Detection and Classification of Concrete Patches by Integrating GPR and Surface Imaging

**Peng Cheng, James V. Krogmeier, Mark R. Bell,
Kelvin Wang, Joshua Li, Guangwei Yang**

AUTHORS

Peng Cheng
Graduate Teaching Assistant
School of Electrical and Computer Engineering
Purdue University

James V. Krogmeier, PhD
Professor of Electrical and Computer Engineering
School of Electrical and Computer Engineering
(765) 494-3530
jvk@purdue.edu
Corresponding Author
Principle Investigator

Mark R. Bell, PhD
Professor of Electrical and Computer Engineering
School of Electrical and Computer Engineering
Purdue University
Principle Investigator

Kelvin Wang, PhD, PE
Regents Professor
School of Civil and Environmental Engineering
Oklahoma State University

Joshua Li, PhD, PE
Associate Professor of Transportation Engineering
School of Civil and Environmental Engineering
Oklahoma State University

Guangwei Yang
Post Doctoral Researcher
School of Civil and Environmental Engineering
Oklahoma State University

JOINT TRANSPORTATION RESEARCH PROGRAM

NOTICE

TECHNICAL REPORT DOCUMENTATION PAGE

1. Report No. FHWA/IN/JTRP-2021/18	2. Government Accession No.	3. Recipient's Catalog No.	
4. Title and Subtitle Detection and Classification of Concrete Patches by Integrating GPR and Surface Imaging		**5. Report Date** May 2021	
		6. Performing Organization Code	
7. Author(s) Peng Cheng, James V. Krogmeier, Mark R. Bell, Kelvin Wang, Joshua Li, and Guangwei Yang		**8. Performing Organization Report No.** FHWA/IN/JTRP-2021/18	
9. Performing Organization Name and Address Joint Transportation Research Program Hall for Discovery and Learning Research (DLR), Suite 204 207 S. Martin Jischke Drive West Lafayette, IN 47907		**10. Work Unit No.**	
		11. Contract or Grant No. SPR-4213	
12. Sponsoring Agency Name and Address Indiana Department of Transportation (SPR) State Office Building 100 North Senate Avenue Indianapolis, IN 46204		**13. Type of Report and Period Covered** Final Report	
		14. Sponsoring Agency Code	

15. Supplementary Notes
Conducted in cooperation with the U.S. Department of Transportation, Federal Highway Administration.

16. Abstract
This research considers the detection, location, and classification of patches in concrete and asphalt-on-concrete pavements using data taken from ground penetrating radar (GPR) and the WayLink 3D Imaging System. In particular, the project seeks to develop a patching table for "inverted-T" patches. A number of deep neural net methods were investigated for patch detection from 3D elevation and image observation, but the success was inconclusive, partly because of a dearth of training data. Later, a method based on thresholding IRI values computed on a 12-foot window was used to localize pavement distress, particularly as seen by patch settling. This method was far more promising. In addition, algorithms were developed for segmentation of the GPR data and for classification of the ambient pavement and the locations and types of patches found in it. The results so far are promising but far from perfect, with a relatively high rate of false alarms. The two project parts were combined to produce a fused patching table. Several hundred miles of data was captured with the Waylink System to compare with a much more limited GPR dataset. The primary dataset was captured on I-74. A software application for Matlab has been written to aid in automation of patch table creation.

17. Key Words pavement, pavement patching, ground penetrating radar, three-dimensional imaging, patching table		**18. Distribution Statement** No restrictions. This document is available through the National Technical Information Service, Springfield, VA 22161.		
19. Security Classif. (of this report) Unclassified		**20. Security Classif. (of this page)** Unclassified	**21. No. of Pages** 89 including appendices	**22. Price**

Form DOT F 1700.7 (8-72)   Reproduction of completed page authorized

EXECUTIVE SUMMARY

Introduction

In this research, the problem considered is to develop practical methods to detect, locate, and classify patches in concrete and asphalt-on-concrete pavements using data taken from ground penetrating radar (GPR) and the WayLink 3D Imaging System—effectively fusing the information from the below pavement and above pavement sensing systems. In particular, the project seeks to develop a patching table for "inverted-T" patches, which were not constructed to current best practices, since they did not use dowel bars to transfer load from pavement to patch to pavement. Inverted-T patches typically use "ears" undercut below the existing good pavement as an attempt to transfer load. They were originally recommended in situations where dowels could not be used and still maintain a relatively small patch, e.g., if the condition of pavement on either side of the patch location could not support dowels.

Findings

The Oklahoma state team considered visual methods for pavement patch detection. Several deep learning architectures were applied, including object detection methods (SSD300 and Mark R-CNN) and image segmentation methods (U-Net). The results based solely on imaging were inconclusive, as expected, and some reasons, including a very limited training dataset, were hypothesized for this. Later, a method based on threshold international roughness index (IRI) values computing on a 12 foot window was used to localize pavement distress, particularly as seen by patch settling. This method was far more promising.

The Purdue team developed algorithms for segmentation of the GPR data and for classification of the ambient pavement and the locations and types of patches found in it. The results so far are promising but far from perfect due to a relatively high rate of false alarms.

An integrated patching table was constructed for a seven mile segment of I-74 data by fusing the laser and GPR patching tables using an "agree-within-5-meters" test. The laser patching table was based on thresholding IRI and the GPR table from pattern matching on GPR images. The laser patching table is used to filter the GPR patching table to those patches with evidence of failure. With current GPR technology it does not appear to be feasible to reliably discriminate between inverted-T patches and other plain concrete and non-reinforced patches. This is because reinforcing steel used deep in an inverted-T patch is not reliably detected due to low signal-to-noise ratio and the fact that the absence of dowels in a patching application (which might indicate inverted-T) is also difficult to detect when using a transverse E-field GPR moving longitudinally down the road. New 3D GPR technologies may be able to solve this problem.

Implementation

Several hundred miles of data was captured with the Waylink System to compare with a much more limited GPR dataset. The primary dataset was captured on I-74. A software application for MATLAB has been written and will be provided to Dwayne Harris to aid in his efforts to automate the GPR patch table creation. In addition, the software will allow importation of the visual patching table from WayLink.

<div align="center">CONTENTS</div>

LIST OF FIGURES

LIST OF TABLES

1. INTRODUCTION

Indiana pavements are generally described as asphalt (flexible), concrete (rigid), or asphalt-over-concrete composite pavements. As part of a larger study of life cycle costs, a survey of Indiana pavement types was completed by Lamptey et al. (2005) where they found the entire state highway network was approximately 8% concrete, 28% asphalt-on-concrete, and 64% asphalt. This project primarily concerns patch locations and patch classifications in concrete and asphalt-on concrete pavements, of which there are many thousands of miles. In many cases it is difficult from visual inspection alone to determine the health of an existing pavement patch, furthermore, concrete pavement patches are frequently overlain with asphalt, and effectively concealing the location until failure is well-underway.

Furthermore, a particular type of concrete patch called an "inverted-T" has been used in the past and has been found to be failing at higher than expected rates. The current recommended practice for full-depth concrete patching is the use of dowel rods on either side of the patch in order to transfer load from the patch to the existing pavement on either side. This is done to prevent "rocking" and it's associated deleterious effects. However, in the past in cases where dowels could not be used, e.g., if the old slab was deteriorated or rubblized, the practice was to use inverted-T patches (INDOT, 2013). In this case, the base or subbase was removed below the patch and also under the existing undamaged pavement on either side of the patch for a distance or around 6 inches. Then the void created was filled with concrete. These are difficult repairs and it is very hard to properly compact the subbase under the existing pavement (McDaniel, 2020). For this reason and that they are prone to premature failure (Hall & Darter, 1994), inverted-T patches will not be included in the next revision of the *INDOT Design Manual* and are being removed from existing pavements during rehabilitation.

1.1 Problem Statement

The problem considered in this research is to find practical methods to locate and classify the different types of concrete patches and to deliver a corresponding patching table. According to McDaniel (2020), there are three types of patches used in composite pavements (1) full-depth doweled concrete patches, (2) inverted-T patches, and (3) full-depth asphalt patches. The first two may or may not be overlain with asphalt.

In particular, it is desired to find and classify inverted-T patches, which are believed to be failing at a higher rate than are dowel stabilized patches. INDOT needs to be able to locate them for either proactive repair or for more careful monitoring of their performance. Monitoring and early repair is known to be cost effective.

1.2 Literature Review and Technical Background

The known methods for classifying composite pavement patches are: visual inspection from the surface of undisturbed pavement via either automatic or non-automatic means (Kang et al., 2015; Wang et al., 2018), studies of pavement resilience using falling weight deflectometer (FWD) (Hall & Darter, 1994; Noureldin et al., 2003), survey by ground penetrating radar (GPR) (Maser, 2002), coring samples in the vicinity of patches, and visual inspection after removal of a wearing surface (Blight, 2009; MoDOT, 2018). A comprehensive literature survey has recently been published by McDaniel (2020). In the current project two of the patch classification methods discussed above were compared: automatic visual inspection based on the WayLink 3D Imaging System used by INDOT and ground penetrating radar based upon INDOT's available equipment from GSSI, Inc.

1.2.1 3D Surface Imaging Technology

INDOT uses an imaging technology supplied by the WayLink Systems Corporation encompassing automated pavement condition survey (including cracking, rutting, texture, roadway geometry) at 1 mm resolution up to 60 mph. The working principle used in the system is based on line-laser triangulation to determine the height information on a surface. The INDOT 3D system has been calibrated to provide a true transverse profile at 1-mm resolution across the entire lane, with the height resolution at 0.5 mm. Each transverse profile is a single line with 4,000 points of height information. Wang et al. (2017, 2018) and others have been exploring the use of deep-learning in hope of automating road surface cracking surveys. Good results with region-based convolutional neural networks have been reported (Wang et al., 2018) along with discouraging results from a Vincennes area study that showed no correlation between asphalt and concrete distress using neural nets (Kang et al., 2015).

Left and right wheel tracks can be extracted from the transverse profiles and used to longitudinal profiles for each wheel track and these can be used to compute the international roughness index (IRI). IRI is used to quantify roughness and which can then be thresholded to identify areas of potential subsurface distress, which can be compared with GPR. Additional work is reported in the appendix to this report.

1.2.2 Ground Penetrating Radar Technology

Figure 1.1 shows a basic ground penetrating radar (GPR) block diagram with pulse generation, transmit antenna, receive antenna, correlation processing, and subsequent blocks for detection, analysis, and visualization. In the pavement survey application, the scanned volume would typically include layers of air, asphalt, concrete, and the base and soil below. All radars, including GPRs, detect targets by launching
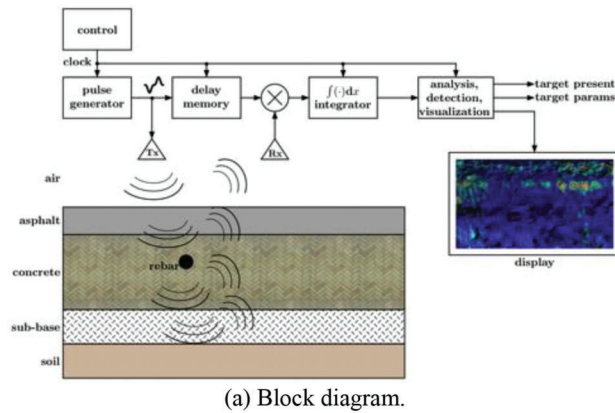
(a) Block diagram. (b) INDOT GPRs behind survey van.

Figure 1.1 Ground penetrating radar system.

TABLE 1.1
Parameters for EM wave propagation (Buyukozturk, 1997; Drnevich et al., 2001; Maser, 2003; Porubiaková & Komačka, 2015; Smith & Scott, 1989)

Material	Relative Permittivity (real part)	Speed of EM Propagation (cm/ns)	Wavelength at 500 MHz (cm)	Excess Round-Trip Power Loss Relative to Free Space at 500 MHz (dB/cm of depth)
Air	1	29.9	59.8	0
Concrete	7.4–9 (midpt = 8.2)	10.0–11.0 (10.4 at midpt)	20.0–22.0	0.05 (dry)–0.22 (wet)
Asphalt	3.8–7.4 (midpt = 5.6)	11.0–15.3 (12.6 at midpt)	22.0–30.6	Less than concrete
Aggregate	6–18 (midpt = 12.0)	7.0–12.0 (8.6 at midpt)	14.0–24.0	0.045 (dry)
Soil	4.5–30 (midpt = 17.25)	5.5–14.1 (7.2 at midpt)	10.9–28.2	0.4
Water	81	3.3	6.6	Very high

electromagnetic waves into the scanned volume and looking for reflections from the targets, which are received back at the radar. The radar indicated in the figure has separate transmit and receive antennas, which is called bistatic operation. It is the most common operating mode for GPRs. In the GPR application envisioned here, targets of interest are rebar, rebar chairs/baskets, wire mesh, and the various interfaces between the layers (asphalt, concrete, base, etc.) comprising a road. The purpose of a radar is to estimate properties of a target, e.g., its presence or non-presence, etc.

Interpretation of GPR data requires an understanding of the elementary parameters governing electromagnetic wave propagation in the media of interest: air, concrete, asphalt, aggregate, and soil. These are listed in Table 1.1 along with sources for the different numbers. It is important to note that the range of values is rather large and that the effect of moisture is also large. Of most interest are (1) the speed of propagation, (2) the power losses incurred, and (3) the magnitude of reflection and transmission at boundaries.

Roughly speaking the ordering of propagation speed from fastest to slowest is air >> asphalt > concrete > soil > aggregate >> water. The ordering of power losses in excess of free space loss is, from smallest to largest is air << aggregate < asphalt < concrete << soils << water. It should also be carefully noted that

aggregate, asphalt, and concrete look very similar in a GPR image.

A typical road is constructed of layers of these materials of different thicknesses. With a concrete road of 11-inch thickness on top of a 21-inch layer of aggregate, we would expect a worst-case roundtrip loss through both layers of about 10 dB to the compacted soil layer. Note that there are other sources of apparent loss to consider as well. But the bottom line would be that a reasonably detectable signal should return from the reflection off of the bottom soil layer. Losses increase rapidly with frequency, however, and this limits GPR to operate in frequencies below 2 GHz if imaging to reasonable depth is needed.

To understand some of the timing considerations in pulses used to image under the road consider the approximate time it would take an EM wave to propagate down through a 1-meter deep concrete, reflect off something near the bottom of the layer, and return. For simplicity, assume a typical propagation speed of 10 cm/ns. This would yield a roundtrip time of about 20 ns. The duration of the pulse used to image needs to be short enough to avoid excess overlapping of reflections in the material when received at the receiving antenna. Since the window for receiving all reflection returns is only on the order of 30 ns, if we assume that about 5 reflections return in that interval, then each must be only a few ns wide. Therefore, pulse bandwidth must be on the order of 1 GHz. Because losses increase
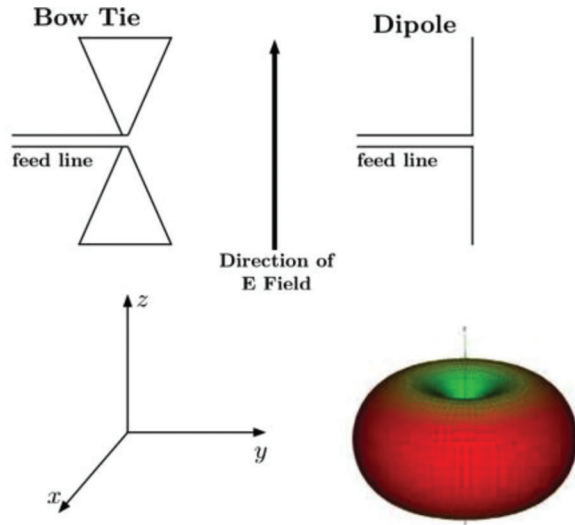
Figure 1.2 Illustration of antenna concepts important for understanding GPR.
Note: Top left: Bowtie antenna as seen from the pavement looking up into the GPR. The z-axis is oriented along the axis of the antenna and in the direction of the E-field polarization (bottom left). The typical orientation of the y-axis is in the longitudinal direction along the lane. The z-axis is then transverse to the lane and the x-axis is pointing downward into the pavement. Top right: Dipole antenna with the same orientation as the bowtie antenna. Bottom right: Radiation pattern of the ideal dipole. Note that the bow tie antenna has a radiation pattern like that of the dipole.

rapidly with frequency these two facts combine to suggest a 1 GHz bandwidth signal in a total bandwidth of about 1 GHz. This sort of "back of the envelope" sanity check suggests the use of a classical ultra-wideband (UWB) signal.

Finally, many GPR systems, including several models of GSSI radars, use bowtie antennas in bistatic mode. Figure 1.2 shows a bowtie antenna including its polarization direction and the antenna pattern of a dipole. The bowtie approximates a dipole pattern, but it passes a much wider frequency band than does the dipole (Ramo et al., 1984). As used in the GSSI Model 5103 a pair of bowtie antennas, one for transmit and one for receive, are pulled along the road surface in the direction of the y-axis in the figure. The electric field vector is transverse to the road and the antenna pattern is directed down into the road surface. From the figure and the fact that the bowtie approximates the dipole pattern it is apparent that there is very little directional sensitivity in the ideal case. However, neither a dipole nor a bowtie can be built without a feedline, which disrupts the isotropic pattern of the ideal case. GSSI indicates that their bowtie antennas radiate in a cone of approximately 60 degree width (GSSI, 2017).

When a UWB GPR launches a short-pulse electromagnetic wave into a road surface from a transmit antenna, a complex waveform is received a very short time later at the receive antenna. The waveform is the result of multiple reflections of the incident wave from the various layers that make up the road itself. In addition, there is a direct wave that travels without reflection from the transmit antenna to the receive antenna, which is typically the first return seen by the radar receiver.

In the case of most interest to this research, the road layers from top to bottom are asphalt, concrete, aggregate, and soil. If we assume an antenna positioned above the road, as with the GSSI RoadScan 30, then the layer thicknesses might be 100 cm of air, 10 cm of asphalt, 20 cm of concrete, and 50 cm of aggregate. Using the "average" permittivities for each material from Table 1.1, the round-trip travel times through each material layer would be approximately: $2T_{air}= 7$ ns, $2T_{asphalt}=2$ ns, $2T_{concrete}=4$ ns, $2T_{aggregate}=12$ ns. For purposes of illustration, we consider the following two cases. These are merely meant to inform about delay times and relative strengths of reflections. In realistic construction, rebar would not be found below the aggregate in the bottom layer. It would be found near the center of the concrete layer.

1. In the first case the incident waveform travels from the transmitter antenna down through all the layers undergoing partial reflection and transmission at each interface. A small fraction of the incident wave is reflected from the soil layer at the bottom where it begins a return trip to the receiver antenna. The majority of the energy is transmitted into the soil layer, where it is lost.
2. In the second case, the incident waveform eventually encounters a good conductor, such as rebar, and the vast majority of the incident energy is reflected back towards the receiver antenna.

The determination of the amount of an incident wave, which is reflected or transmitted at a material boundary is regulated by the natural impedances of the materials on either side of a boundary:

$$\rho_{1\to2} = \frac{\eta_2 - \eta_1}{\eta_2 + \eta_1} \qquad \text{(Eq. 1.1)}$$

$$\tau_{1\to2} = \frac{2\eta_2}{\eta_2 + \eta_1} \qquad \text{(Eq. 1.2)}$$

where the impedance is given by the square root of the ratios of the magnetic permeability and the dielectric permittivity, which simplifies to $\eta = 377/\sqrt{\epsilon_r}$ in Ohms. See also Figure 1.3

The formulas above work when Medium 2 is a perfect conductor by taking the limit as the impedance of material 2 approaches zero. The equations given in Figure 1.3 are written for the case of short pulses rather than sinusoidal steady state. Table 1.2 also gives the impedance parameters needed to predict reflection and transmission at the various material boundaries found in a typical road. These were used to calculate the reflection and transmission parameters in all the cases that could arise with these materials and the result is documented in Table 1.3.

The left side of Figure 1.4 gives a reflection/transmission diagram for a wave proceeding downward through a road without a rebar reflection at the
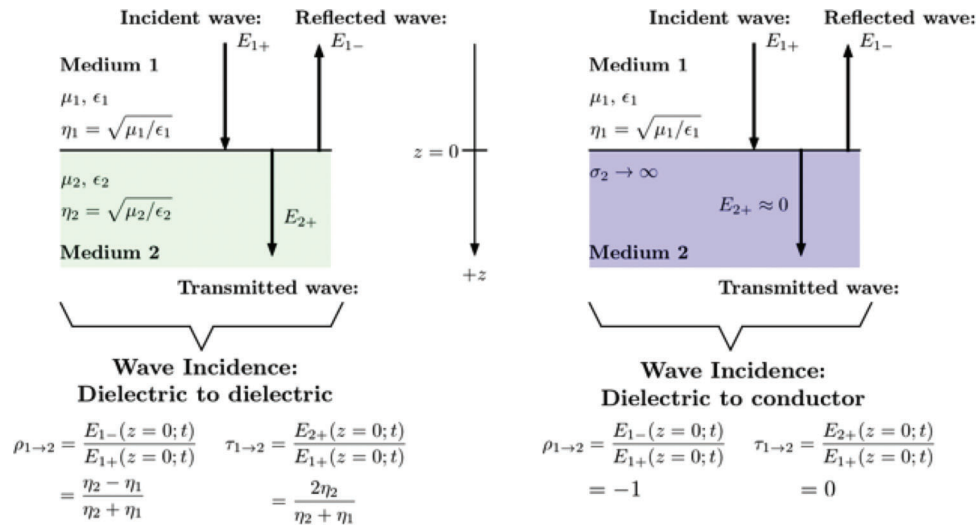
$$\rho_{1\to2} = \frac{E_{1-}(z=0;t)}{E_{1+}(z=0;t)} \qquad \tau_{1\to2} = \frac{E_{2+}(z=0;t)}{E_{1+}(z=0;t)}$$
$$= \frac{\eta_2 - \eta_1}{\eta_2 + \eta_1} \qquad\qquad = \frac{2\eta_2}{\eta_2 + \eta_1}$$

$$\rho_{1\to2} = \frac{E_{1-}(z=0;t)}{E_{1+}(z=0;t)} \qquad \tau_{1\to2} = \frac{E_{2+}(z=0;t)}{E_{1+}(z=0;t)}$$
$$= -1 \qquad\qquad\qquad = 0$$

Figure 1.3 Illustration of reflection and transmission coefficient calculation.
Note: An electro-magnetic wave is traveling from Medium 1 past a boundary into Medium 2. Medium 1 is a dielectric. On the left side Medium 2 is a dielectric. On the right side Medium 2 is a perfect conductor.

TABLE 1.2
Parameters for EM wave propagation in various media

Material	Relative Permittivity (real part)	Speed of EM Propagation (cm/ns)	Impedance (Ohms)
Air	1	29.9	376.7
Asphalt	5.6	12.6	159.2
Concrete	8.2	10.4	131.6
Aggregate	12.0	8.6	108.8
Soil	17.3	7.2	90.7

Note: For simplicity the permittivity ranges from Table 1.1 have been replaced by the midpoint of each range.

TABLE 1.3
A generic example of a layered road

Reflection Coefficient: Medium 1 → Medium 2 / Transmission Coefficient: Medium 1 → Medium 2		Medium 2				
		Air	Asphalt	Concrete	Aggregate	Soil
Medium 1	Air	0 / 1	-.41 / .59	-.48 / .52	-.55 / .45	-.61 / .39
	Asphalt	.41 / 1.41	0 / 1	-.10 / .90	-.19 / .81	-.27 / .73
	Concrete	.48 / 1.48	.10 / 1.10	0 / 1	-.09 / .91	-.18 / .82
	Aggregate	.55 / 1.55	.19 / 1.19	.09 / 1.09	0 / 1	-.09 / .91
	Soil	.61 / 1.61	.27 / 1.27	.18 / 1.18	.09 / 1.09	0 / 1

Note: Reflection and transmission coefficients for the possible dielectric to dielectric material boundaries found in a road. In each case the top number is the reflection coefficient and the bottom number is the transmission coefficient. In the table the rows correspond to Medium 1, which is that through which the incident wave approaches the boundary, and the columns correspond to Medium 2, through which the transmitted wave passes.
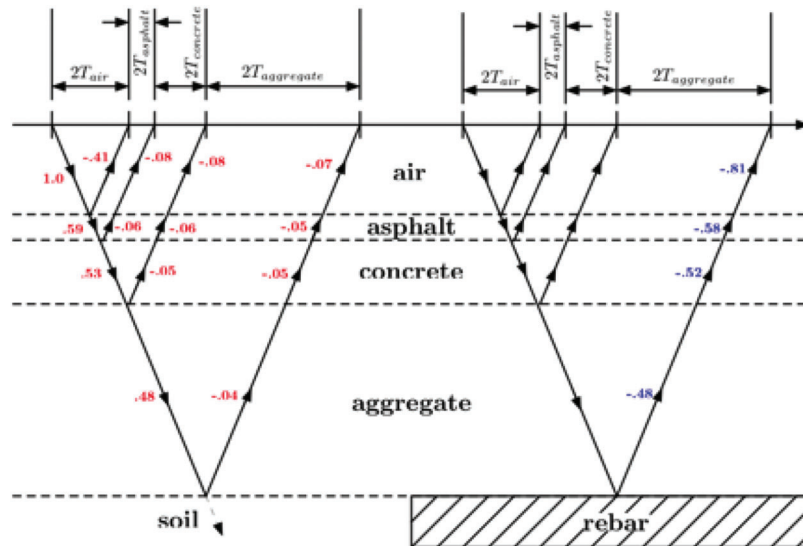
Figure 1.4 Reflection/transmission diagrams.
Note: The left side shows soil at the bottom. The right side shows rebar at the bottom. In each figure the amplitude parameter for the electric field is listed next to the arrow. The cases on left and right only differ in the strengths of the amplitude parameters for the wave returning from the bottom-most material boundary.

bottom. The numbers next to the arrows indicate the amplitudes of the corresponding waves. For example, if a wave of normalized amplitude 1.0 impinges on the asphalt surface, four major returns are seen at the receive antenna. The first, direct wave, results from the reflection from the air-asphalt interface and has relative amplitude -0.41, which indicates a change in polarity in the electric field relative to the incident wave. Next come waves resulting from the asphalt-concrete and concrete-aggregate interfaces. Finally, a reflection from the soil at the bottom results in a wave with amplitude -0.07 arriving at about 25 ns after the transmitted pulse using the round trip times above. The right side of the same figure shows the change when the bottom reflection is from rebar rather than soil. In that case the final reflection at 25 ns has an amplitude of -0.81, which is much stronger. In the figure, we have ignored both losses in propagation through the various

media and the existence of secondary reflections. The first secondary reflection we have ignored occurs when the upward directed wave from the asphalt-concrete interface reaches the air-asphalt interface. The figure indicate a transmission wave into the air with amplitude equal to -0.06. There is in addition another reflection back into the asphalt of relative amplitude equal to -0.02. Though this is not shown in the diagram it would then result in another set of signals seen at the receive antenna at times 11 ns, 15 ns, and 27 ns. The amplitudes of these three signals would be only about 3% of the direct reflections.

Figure 1.5 shows the idealized signals at the receiver antenna corresponding to the reflection and transmission amplitudes of Figure 1.4. The general character of this signals agree with that seen in actual GPR traces with the exception that signal power loss in propagation has been ignored in of Figure 1.4 and Figure 1.5.
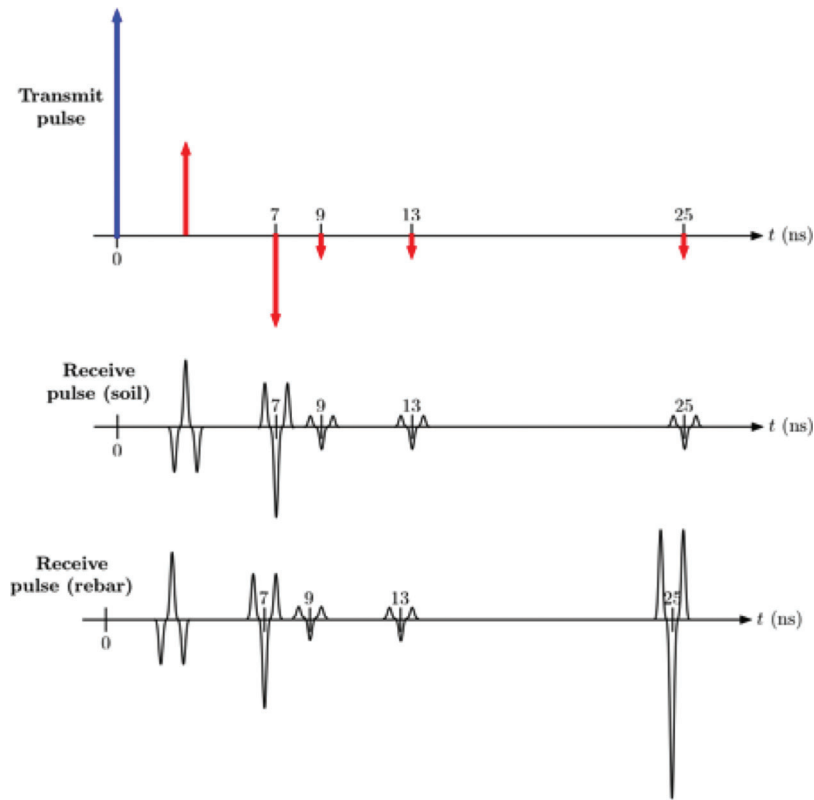
Figure 1.5 Received radar pulses for the situation of Figure 1.4.

2. DATA COLLECTION AND ANALYSIS

2.1 GPR Equipment

Ground penetrating radar (GPR) equipment used in this project was manufactured by Geophysical Survey Systems, Inc. (GSSI). The radar is controlled by a Model SIR-30 controller, which is used in conjunction with antenna packages designed for various center frequencies including 900 MHz, 400 MHz, and 270 MHz. The SIR-30 is capable of transmitting at a maximum pulse repetition frequency (PRF) of 800 kHz while it simultaneously supports up to four radar channels. The unit uses fixed point 32 bit sampling, which gives a dynamic range of about 192 dB all of which data is stored in raw format, e.g., without filtering or gain. Filtering and time-delay-dependent gain can be used for operator display. The SIR-30 also has external connections for survey wheel and/or GPS in order to log radar data with position information and/or to control sampling spatially.

Three antenna center frequencies were used that corresponded to the following antenna package models.

- *Model 3101 900 MHz antenna.* This is designed with a center frequency of 900 MHz for applications requiring high resolution yet relatively shallow penetration depth. The integrated antenna box, of dimensions 33 by 20 by 8 cm, contains one transmit antenna and one receive antenna. The pulse duration of this model is approximately 1.1 nanosecond, which corresponds nominally to a 900 MHz bandwidth. The effective penetration depth is

typically between 0 and 6 feet depending on the permittivity of the material.
- *Model 5040 400 MHz antenna.* The antenna is designed with a center frequency of 400 MHz. It has less resolution and higher penetration depth compared with 900 MHz antenna. The integrated antenna box contains one transmit antenna and one receive antenna. Its dimensions are 30 by 30 by 17 cm. The transmit antenna sends a source signal with a pulse duration of 2.5 nanosecond, and the effective penetration depth is typically between 0 and 16 feet depending on the permittivity of the material.
- *Model 5104 270 MHz antenna.* The antenna is designed with a center frequency of 270 MHz. It provides deeper penetration and less resolution compared with the 900 and 400 MHz options. The integrated antenna box contains one transmit antenna and one receive antenna and is of dimensions 44.5 by 44.5 by 19 cm. The transmit antenna sends a source signal with a pulse duration of 3.7 nanosecond, and the effective penetration depth is typically between 0 and 25 feet depending on the permittivity of the material.

2.2 GPR Data Collection

Table 2.1 shows some detail of the GPR datasets that were used in this study. The following three types of parent pavements were identified: (1) jointed reinforced concrete pavement (JRCP), (2) continuously reinforced concrete pavement (CRCP), and (3) jointed plain concrete pavement (JPCP). Various combinations of GPR antenna center frequencies and polarizations

were also used. In addition, some calibration data was taken with the 900 MHz antenna package in the Division of Research shop, which is reported further in the appendix. See also Figure 2.1 showing the data collection areas on an Indiana map.

Most of the data collection runs shown in Table 2.1 were used for algorithm development and tuning. The final run, used to build a sample patching table and for comparison to the results of the WayLink 3D Imaging System, is shown last in the table. This run, on I-74 RP

TABLE 2.1
GPR dataset details

Date	Hwy	RPs	Lane	Ambient Pavement	Wheel Path	Radar Configuration
09-15-2015	I-74	143–163 EB & WB	Driving	JRCP	Right	400 MHz, trans-E
					Left	900 MHz, trans-E
12-15-2016	I-65	141–165 NB & SB	Driving and passing	CRCP	Right	900 MHz, trans-E
					Left	900 MHz, trans-E
07-24-2018	I-465	38–42 NB & SB	1, 2, 4 (Lane 1 is adjacent to median)	JPCP	Right	900 MHz, trans-E
					Left	900 MHz, trans-E
06-03-2020	I-74	157–163 EB & WB	Driving	JRCP	Left	900 MHz, long-E
					Right	900 MHz, trans-E
					Right	400 MHz, trans-E
					Right	270 MHz, trans-E

(a) I-65, I-465, I-74
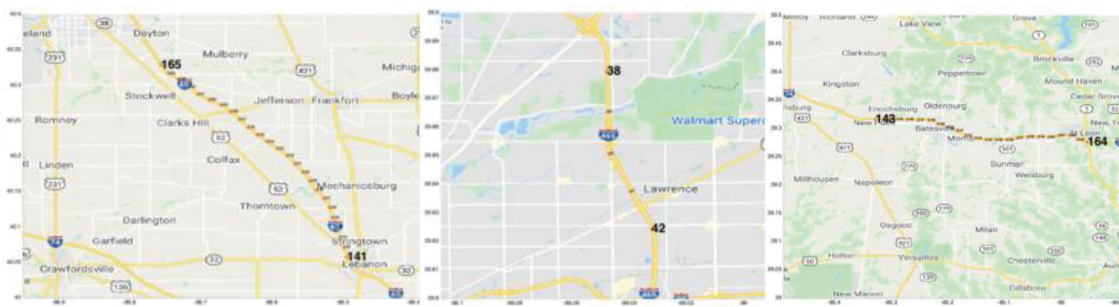
(b) I-65   (c) I-465   (d) I-74

Figure 2.1 Map of data collection areas.

156 to 164 EB and WB, was conducted in June 2020. In this run all three GSSI antennas were used: 270 MHz, 400 MHz, and 900 MHz. The latter was used in two orientation relative to the direction of travel during the survey. The vehicle towing the antennas and the control unit are shown in Figure 2.2(a). A close-up showing the antenna arrangement is given in Figure 2.2(b) and (c). On the left wheel path, the vehicle pulls a 900 MHz GPR antenna by its long side. On the right wheel path, it pulls the other 900 MHz GPR antenna by its short side followed by a 400 MHz and a 270 MHz antenna.

Channel 2 collects 900 MHz data in the regular transverse-E mode (right wheel path in Figure 2.2) where in comparison Channel 1 (left wheel path in Figure 2.2) is turned 90 degrees. Having one antenna's electric field aligned with direction of travel (longitudinal) and the other transverse is beneficial to inspection of underlying pavement condition and will be discussed in detail in the next section. Channels 3 and 4 are behind Channel 2 and have lower frequencies in order to penetrate deeper underground and compare with the Channel 2 data.

2.3 GPR Data Analysis

This section, which concerns the construction and GPR features evident in ambient pavements and patches is summarized in Table 2.2.

2.3.1 Features Appearing in GPR Images

In the standard data collection setup used by INDOT GPR antenna packages are pulled along a road in the direction of travel while recording simultaneously in the left and right wheel paths of the lane. The situation is shown in Figure 2.2. In some cases, only a single antenna is towed, typically in the right wheel path. Surveys usually focus on the driving lane of a multiple lane facility. The GPR antenna is typically, though not always, oriented with electric field polarization in the transverse direction (i.e., orthogonal to the direction of motion).

The features that appear in a GPR image are the interfaces between regions of differing dielectric constant (e.g., antenna-to-air, air-to-asphalt, asphalt-to-concrete, concrete-to-base, and base-to-soil) or conducting surfaces such as buried rebar or wire mesh. When the electric field is oriented in the transverse direction, then rebar or wire also oriented in the transverse direction will produce a stronger reflected signal than rebar or wire oriented longitudinally (Figure 2.3). As the GPR is moved longitudinally down the road over a buried transverse conducting bar, the image produced is an inverted segment of a hyperbolic curve with the vertex at the location of the bar's transverse axis (Travassos et al., 2018). See Figure 2.3(c).

The two possible orientations of the electric field in a road survey are illustrated in Figure 2.3(a). In a conventional GPR survey, antennas are oriented with transverse electric field, which puts it parallel to any transverse conductors. This maximizes the reflected electromagnetic waves and makes the detection easier. On the other hand, a longitudinal electric field orientation is able to see below the transverse steel rendering a clearer image below (ASTM International, 2019). Consequently, this choice makes measuring pavement thickness and detecting deterioration possible. Frequently, there are features of interest associated with steel reinforcement aligned in either the transverse or the longitudinal direction, and therefore it makes sense to include both transverse and longitudinal electric field when possible.

(a) Test vehicle with GPR antennas attached.
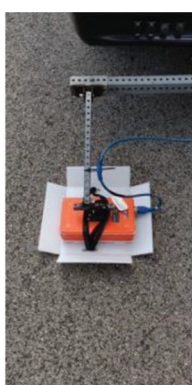
(b) Antenna arrangement in left wheel path: Channel 1–900 MHz longitudinal E-field polarization.
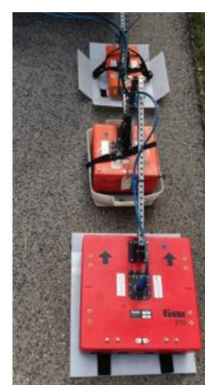
(c) Antenna arrangement in right wheel path: Channel 2–900 MHz transverse E-field polarization (top), Channel 3–400 MHz transverse E-field polarization (middle), and Channel 4–270 MHz transverse E-field polarization (bottom).

Figure 2.2 INDOT GPR test from June 2020 on I-74.

TABLE 2.2
Ambient pavements and patch types seen in the main data set used in this study (2020 I-74 data)

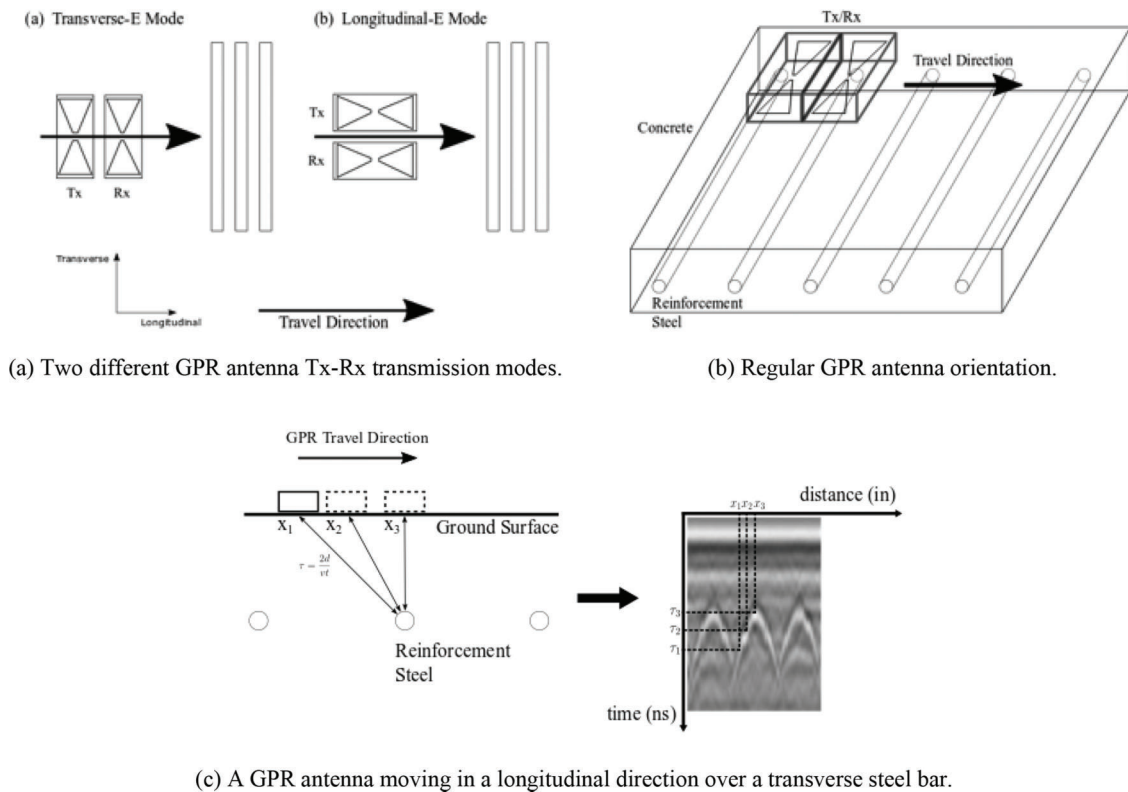|	Class	Construction	GPR features
Ambient Pavements	Jointed Plain Concrete Pavement (JPCP)	No reinforcement. Transverse dowels at joints. Dowels held up by wire baskets with some transverse steel before construction and left inside the curing concrete. Longitudinal joint spacing ranges from 12 to 25 feet.	Characteristic inverted hyperbolic returns at the joint spacings.
	Jointed Reinforced Concrete Pavement (JRCP)	Welded wire mesh reinforcement with transverse wires spaced about 1 foot in longitudinal direction. Dowels held up by wire baskets as in JPCP but with longitudinal spacing typically larger than in JPCP.	Characteristic inverted hyperbolic returns at the joint spacings. Characteristic inverted hyperbolic returns at the wire mesh spacings also. Joint and mesh returns are clearly distinct from each other.
	Continuously Reinforced Concrete Pavement (CRCP)	Longitudinal rebar held up before concrete curing by transverse steel with longitudinal spacings around 2 to 3 feet. No joints and no dowels or dowel carriers.	No joint returns. Characteristic inverted hyperbolic returns at the transverse steel spacing of 2 to 3 feet.
Patch Types	Type 1 Plain Concrete Patch	No reinforcing steel in the top- or mid-depths of the patch. No apparent layers—all one type of material.	No transverse steel returns. No layer discontinuities.
	Type 2 Plain Concrete Patch	No reinforcing steel in the top- or mid-depths of the patch. Evidence of layers—more than one type of material.	No transverse steel returns. A dielectric discontinuity.
	Type 3 Reinforced Concrete Patch	Welded wire mesh with closely spaced transverse wires. Located in the mid-depths of the patch. Longitudinal spacing between transverse wires typically closer than 1 foot.	Characteristic inverted hyperbolic returns at the wire mesh spacings, typically very close together.

(a) Two different GPR antenna Tx-Rx transmission modes.

(b) Regular GPR antenna orientation.

(c) A GPR antenna moving in a longitudinal direction over a transverse steel bar.

Figure 2.3 GPR over transverse steel bars.

2.3.2 Dowel Bars and Welded Wire Baskets Feature

Dowel bars and welded wire baskets are located at the joint between two adjacent concrete slabs. Their purpose is to transfer loads from one slab to the next across the joint, and at the same time allow joint movement due to contraction and expansion to a certain degree. Because of this their placement is different from that of deformed steel reinforcement. The welded wire basket is used in new construction to hold the dowel bars in place while concrete is poured and cured. They, of course, remain in the concrete and can be detected by GPR. The basket is placed transverse to the direction of travel and provides slots in which to insert longitudinal dowel bars. Figure 2.4 shows a comparison of dowel and welded wire basket in practice and under GPR inspection. In the image the basket assembly is clearly visible even though the much larger dowel is not clear. Note that the welded wire basket is only used in new construction. In a typical patch dowels are chemically anchored into pre-drilled holes.

2.3.3 Pavement Features

GPR is widely used in pavement inspection due to its non-destructive nature and ability to penetrate asphalt and concrete. It provides images of the subsurface structures and helps evaluate pavement thickness which is essential for management and rehabilitation (Harris, 2006). In this project subsurface structures are especially useful in determining the pavement types. In the following subsections, a few common pavement types are shown in plan views and under GPR inspection.
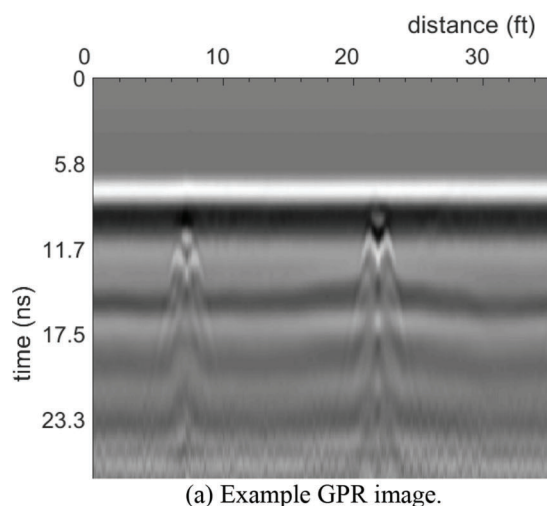
2.3.3.1 Jointed Plain Concrete Pavement. Jointed Plain Concrete Pavement (JPCP) contains no reinforcement inside the concrete. However, the concrete slabs are joined by dowel bars controlling the locations of expected cracks (Whiting et al., 2016). The spacing between transverse joints ranges from 12.5 feet to 25 feet and is typically about 15 feet, as shown in Figure 2.5.

Dowel bars and baskets are the majority of the metal contained in JPCP and therefore become the most noticeable features in identifying the pavement. Figure 2.5(b) and (c) shows examples of a JPCP section under GPR inspection. The pattern of joints (dowel/basket) is clear with 15-foot spacing.

2.3.3.2 Jointed Reinforced Concrete Pavement. Jointed Reinforced Concrete Pavement (JRCP) contains steel mesh inside concrete for reinforcement. Compared with JPCP, JRCP has a wider joint spacing in order to fit the steel mesh that holds together mid-panel cracks. Although JRCP has become a less popular pavement practice for being susceptible to cracks and resultant faulting, it still appears regularly in old sections of interstate highways.

Figure 2.6 shows a glimpse of what JRCP looks like in GPR data. It is noticeable that the joint pattern resembles JPCP. However, in-between the joints we can see the different appearances of steel mesh in the two transmission modes. In longitudinal electric field mode, the electric field is parallel to the longitudinal wire in the mesh while moving in the same direction, thus receiving consistent reflection from them. In transverse electric field mode, as explained previously, the electric field is parallel to the transverse wire while moving perpendicular to them, thus generating hyperbolic shapes.
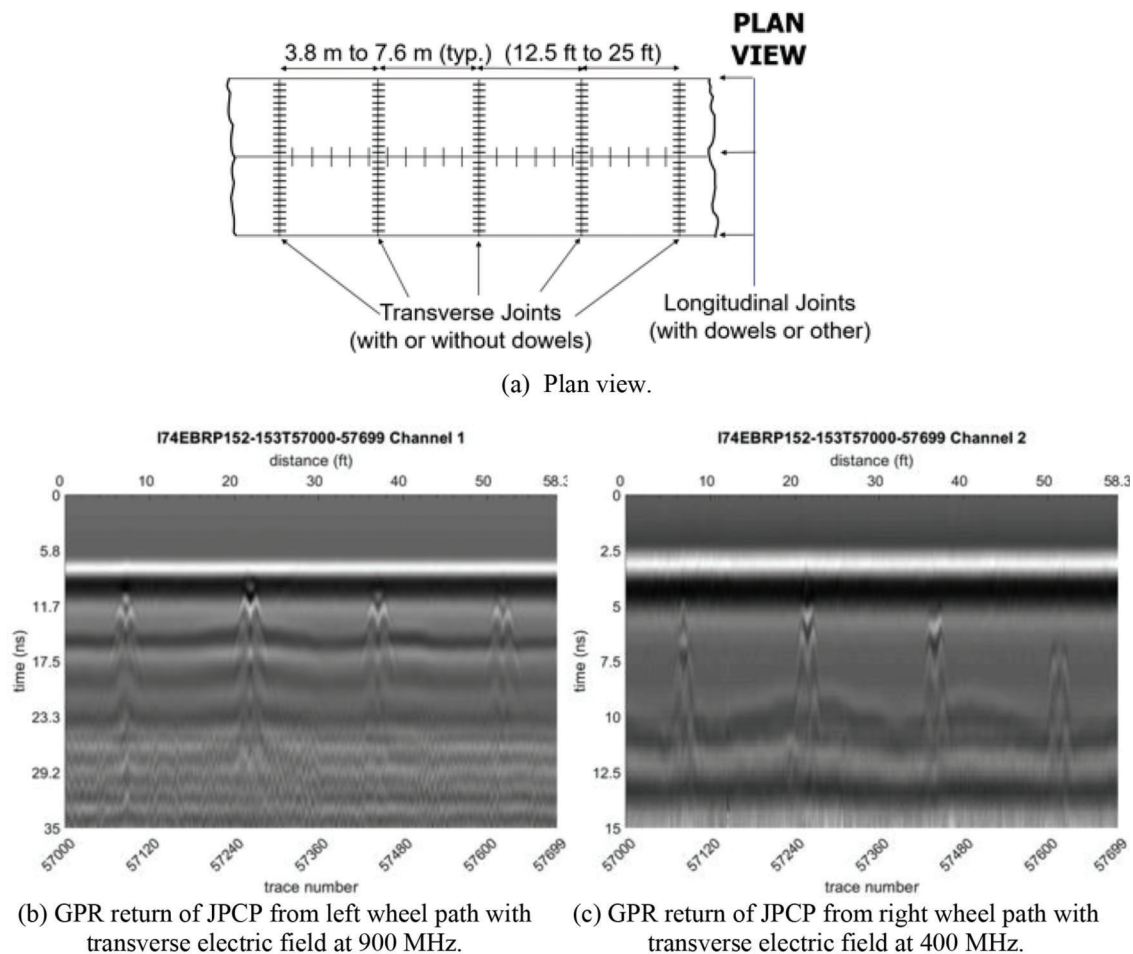

(a) Example GPR image.

(b) Close up of dowel bars and basket.

(c) Placement in construction.

Figure 2.4 Dowel bars and baskets.

PLAN VIEW

3.8 m to 7.6 m (typ.) (12.5 ft to 25 ft)

Transverse Joints
(with or without dowels)

Longitudinal Joints
(with dowels or other)

(a) Plan view.

I74EBRP152-153T57000-57699 Channel 1

(b) GPR return of JPCP from left wheel path with
transverse electric field at 900 MHz.

I74EBRP152-153T57000-57699 Channel 2

(c) GPR return of JPCP from right wheel path with
transverse electric field at 400 MHz.

Figure 2.5 Jointed plain concrete pavement (JPCP) (from 2015 I-74 data).

2.3.3.3 Continuously Reinforced Concrete Pavement. Continuously Reinforced Concrete Pavement (CRCP) uses longitudinal reinforcement steel to hold together the cracks. Controlling the spacing of typical cracks to 3–8 feet is one of the most crucial part of the design process, as shown in Figure 2.7. Although majority of the reinforcement is in longitudinal direction, it requires transverse deformed steel rebar as the support structure (it serves as a chair to support the longitudinal reinforcement). The transverse deformed steel is typically continuous through the adjacent lane, thereby tying the lanes together. The figure also shows a pair of GPR returns of CRCP in transverse-E mode. It is worth noting that the supporting transverse steel in CRCP is not as dense as the mesh structure in JRCP. Note that the tie bars indicated in Figure 2.7(a) are not used in new construction. Instead, transverse deformed steel bars are used to hold up the longitudinal steel. The transverse deformed steel bars typically extend across the lanes thereby tying them together.

2.3.4 Patch Features

As the focus of the project, pavement patches are the most important underground features to look for in data analysis. Three common patch types are discussed in the following subsections.

2.3.4.1 Type 1 (plain concrete patch). Type 1 patch is mostly plain concrete. It is easily identified by looking for the discontinuity of reinforcement structure in pavement. Figure 2.8 shows a typical scenario for a Type 1 patch. The surrounding pavement is identified as JRCP similar to what is shown above. In the center we see the mesh structure breaks up thus indicating the existence of a patch. Also due to the fact that there is no outstanding fluctuation in the received traces inside the patch, we can deduce that the patching material has a similar dielectric property as the surrounding material.

2.3.4.2 Type 2. Type 2 patch is similar to Type 1 patch as they are usually found at the discontinuity of reinforcement. However, unlike the former patch type, Type 2 patch has significant fluctuations inside the patch, as shown in Figure 2.9. This suggests different dielectric property from the surrounding, thus different patching material.

2.3.4.3 Type 3 (reinforced concrete patch). Different from both Type 1 and 2 patches, Type 3 patch contains

(a) Plan view.

(b) GPR return of JRCP from left wheel path with longitudinal electric field.

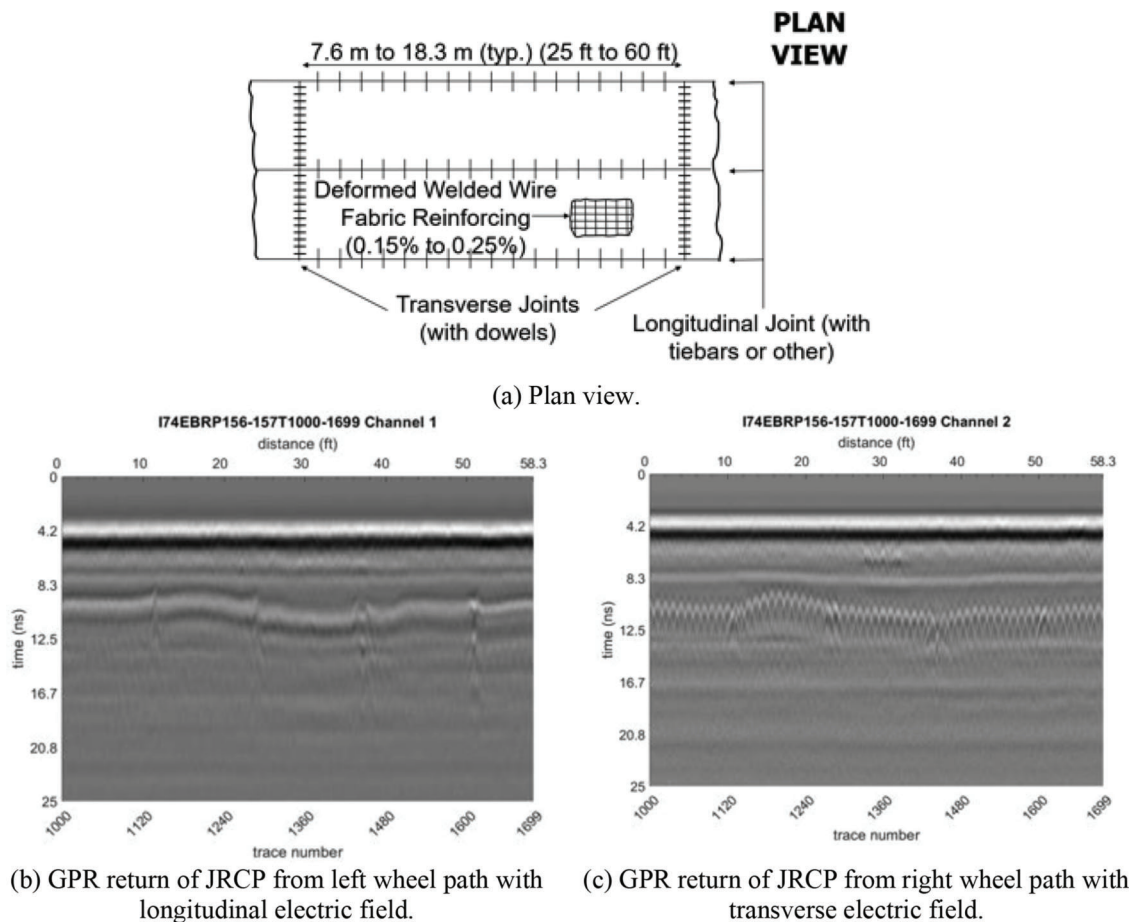(c) GPR return of JRCP from right wheel path with transverse electric field.

Figure 2.6 Jointed reinforced concrete pavement (JRCP).

reinforcement. Usually, the reinforcement in a Type 3 is denser than surrounding mesh structure. Figure 2.10 shows a Type 3 patch in JRCP with the transverse steel twice as dense as the surrounding mesh.

Note that all of the pavements and patches may or may not be overlaid with asphalt. We typically don't distinguish between a pavement or patch, which is 100% concrete and one which is overlaid with asphalt. Because the dielectric constant of the two materials is very close, they are hard to distinguish. For example, note that in Figure 1.4 (for idealized values) that the amplitude of the signal reflection from an asphalt over concrete interface is only about 10% of the incident amplitude, or equivalently, about 1% of the power. One possible exception is found in the distinction between Type 1 and Type 2 patches that only differ because of an apparent dielectric discontinuity at patch mid-depth. These are probably partial depth patches with asphalt over concrete.

The classical inverted-T patch (see Figure A.2 in Appendix A) is a full depth patch of Type 1 or Type 2 in that there is no reinforcing steel at mid-depth and no dowels. Sometimes reinforcing steel is used in an inverted-T to strengthen the "ears" that extend under the existing ambient pavement on either side of the patch. It is sometimes possible to see the reinforcing

steel at full depth, but not reliably, given the low signal-to-noise ratio. The other feature that could be used to find inverted-T patches in the general Type 1 and Type 2 class would be the *absence* of dowel bars. However, dowel bars oriented longitudinally and without the transverse steel in a basket are not reliably detected with transverse electric field GPR.

2.4 Results of Manual Inspection of the 2015 I-74 GPR Data Set

GPR data was captured on I-74 from reference posts 143 to 163 on September 15, 2015. The dataset included the driving lanes in both eastbound and westbound directions with a transverse electric field GPR in both left and right wheel paths. A 400 MHz antenna was used in the right wheel path and a 900 MHz antenna in the left wheel path.

Figure 2.11 shows the patch count data per 1-mile interval over the 21-mile test area. This section of roadway averages about 40 patches per mile or on the order of 100 feet between patches. The road was in relatively poor shape and the reference posts from 143 to 154 were reconstructed in June of 2020. Nevertheless, many of these manually identified patches were very short (on the order of a few feet in length) and were unlikely to be true patches

(a) Plan view.

(b) GPR return of CRCP from left wheel path with transverse electric field at 900 MHz.

(c) GPR return of CRCP from right wheel path with transverse electric field at 900 MHz.
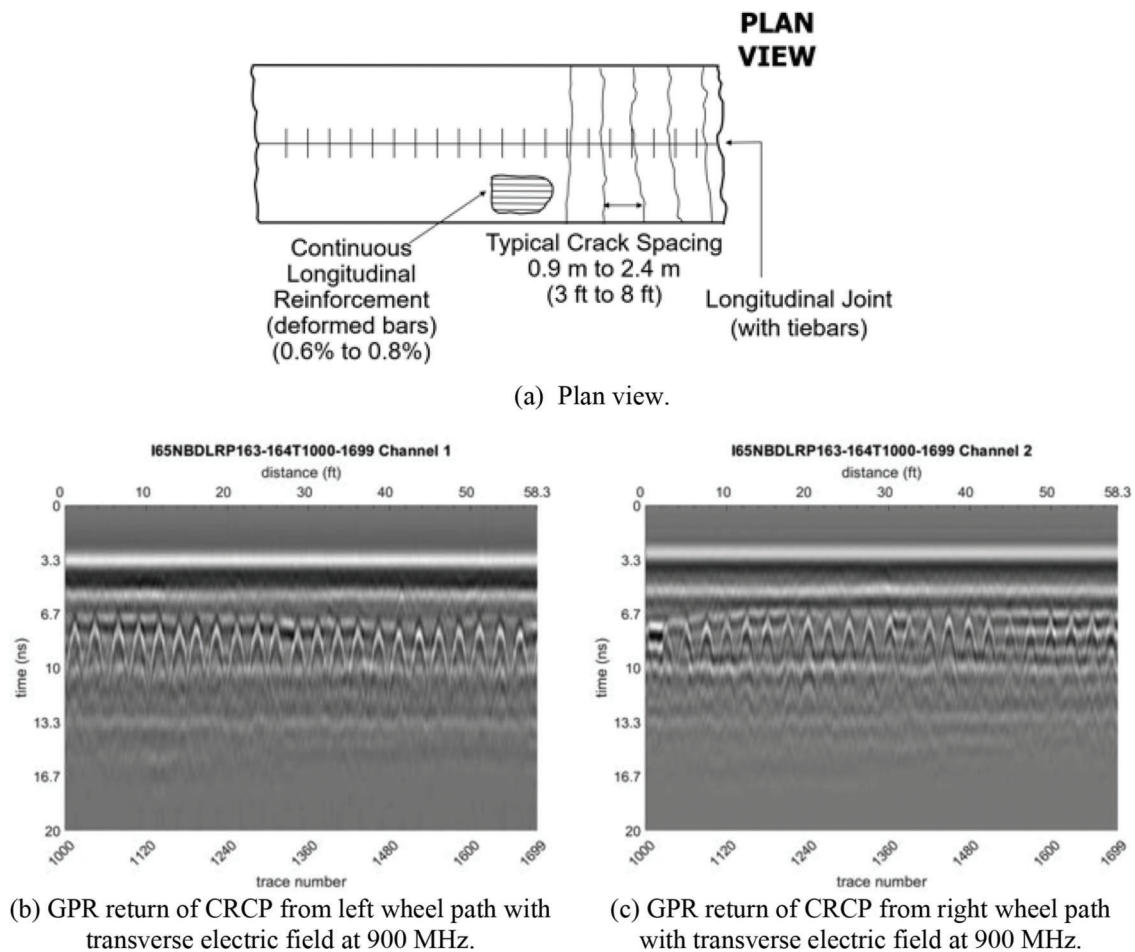
Figure 2.7 Continuously reinforced concrete pavement (CRCP).
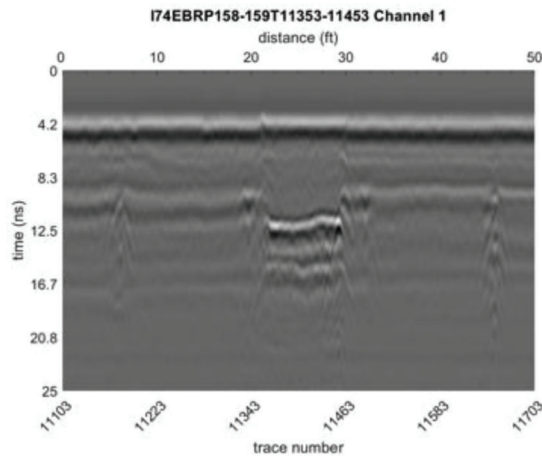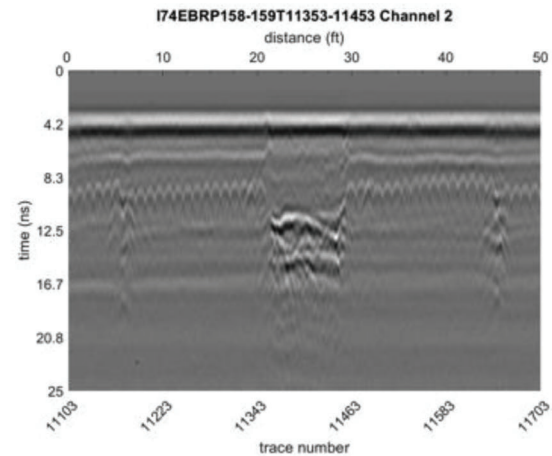

(a) Left wheel path, longitudinal-E.

(b) Right wheel path, transverse-E.
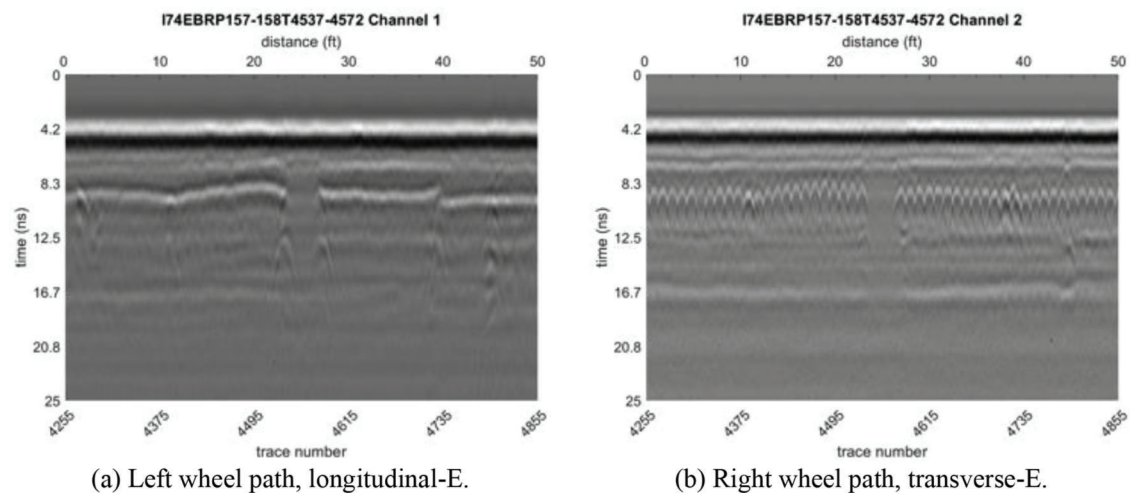
Figure 2.8 GPR return of a Type 1 (plain concrete) patch.

given that it is mechanically impossible to create patches of width equal to 2 feet. These are likely to be some other anomaly of the original construction. See Figure 2.12.

Finally, patches were manually classified as shown in Figure 2.13 and the overwhelming majority of patches were of Type 1.

(a) Left wheel path, longitudinal-E.　　　(b) Right wheel path, transverse-E.

Figure 2.9　GPR return of a Type 2 patch.
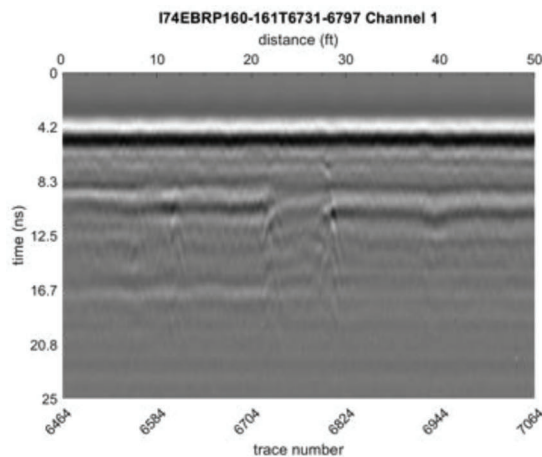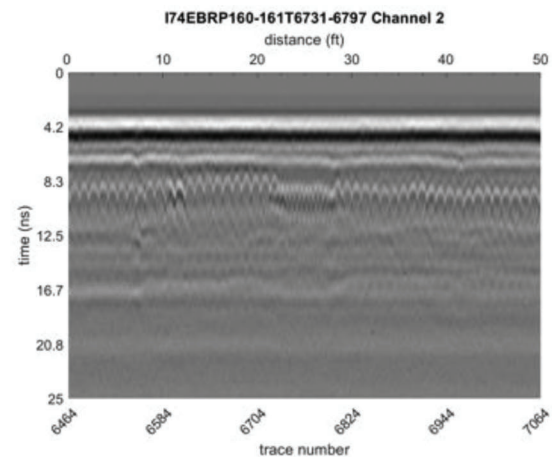
(a) Left wheel path, longitudinal-E.　　　(b) Right wheel path, transverse-E.

Figure 2.10　GPR return of a Type 3 patch.
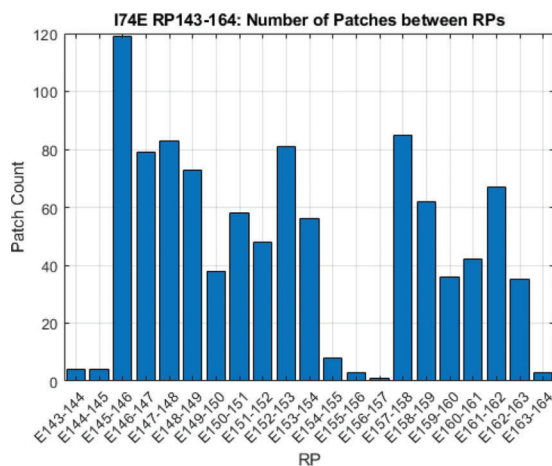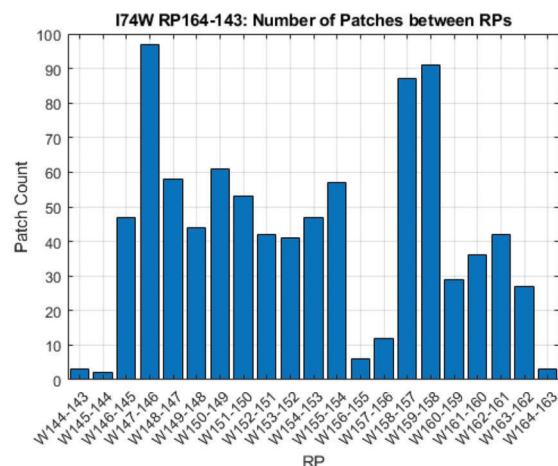
(a) East bound driving lane.　　　(b) West bound driving lane.

Figure 2.11　Number of patches manually observed from I-74 data by 1-mile intervals.
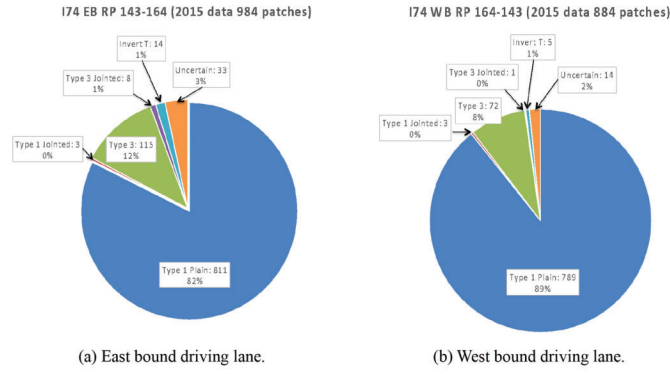
Figure 2.12 Patch classification statistics from manual inspection of 2015 I-74 GPR data.
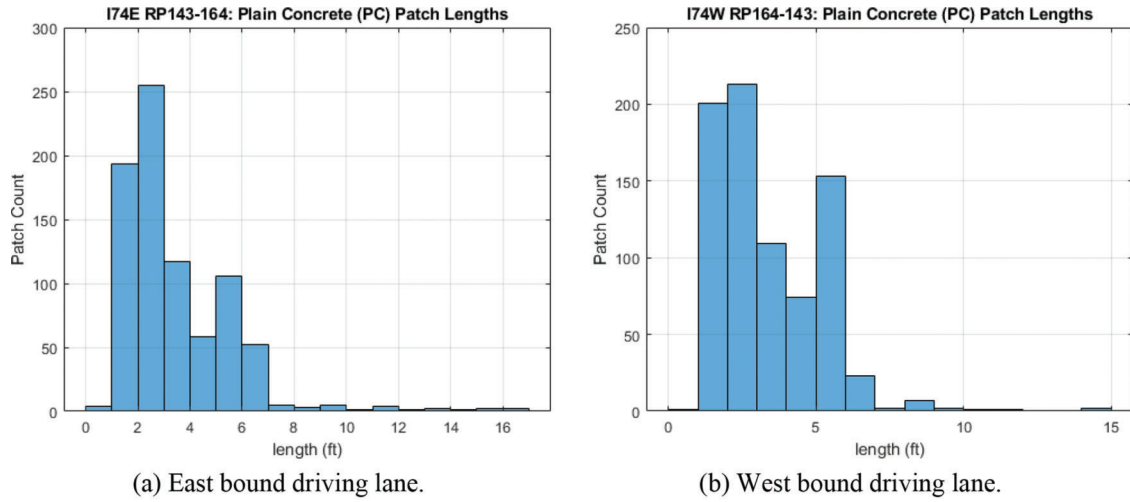
Figure 2.13 Empirical distribution of patch lengths found in manual survey for the Type 1 patches.

3. DETECTION ALGORITHM

The GPR patch detection algorithm is described in the sections below and summarized in Figures 3.1, 3.2, and 3.3.

3.1 Pavement Segmentation

Segmentation algorithm dissects a GPR image into segments based the variations in trace energy. The radar receives different levels of energy depending on the underlying pavement structure, especially the amount of metal because of its high reflectance. For instance, the average trace energy on a JRCP will be much greater than that on a JPCP simply because of the more complicated reinforcement mesh structure in JRCP.

It does not only give the operator an overview of the pavement under test, but also help the detection algorithm avoid wasting computational power on bridges or unlikely patch cases (e.g., reinforced patch in plain concrete pavement).

3.2 Pavement Feature Detection

The problem in hand can be treated as a detection problem and formulated in a hypothesis test as follows:

Let R be a GPR image of window size $n \times m$, $r \in \mathbb{R}$ is realization of R

$$\text{Hypothesis } H_1 : r_1 + w \ \text{(reinforced concrete)}$$

$$\text{Hypothesis } H_0 : r_0 + w \ \text{(plain concrete)}$$

The detector decides:

$$p(x|H_0)p(H_0) \underset{\underset{H_0}{>}}{\overset{\overset{H_1}{<}}{}} p(x|H_1)p(H_1)$$

The distance measure is defined as:

$$D_i^2 = \max_{u \in U, v \in V} c_{u,v}, \ c_{u,v} \text{ denotes an element in } C = RR_i^T$$

Algorithm 1: GPR image segmentation by trace energy

input : $r(n,l)$, a GPR image of size $N \times L$
output: $\{c_p\}$, locations of abrupt changes in trace energy

1 Compute e_l, the energy of each trace
2 Choose c_1, a random index in $\{1,...,L\}$ that divides e_l into two sections
$e_{s_1} = \{e_1,...,e_{c_1-1}\}$ and $e_{s_2} = \{e_{c_1},...,e_L\}$
3 Compute $\bar{e}$, the empirical mean for each section

$$\bar{e}_{s_1} = \mathbf{E}[e_1, e_2,...,e_{c_1-1}], \quad \bar{e}_{s_2} = \mathbf{E}[e_{c_1}, e_2,...,e_L]$$

4 Compute $Var(e)$, the variance for each section

$$Var(e_{s_1}) = \mathbf{E}[(e_{s_1} - \bar{e}_{s_1})^2], \quad Var(e_{s_2}) = \mathbf{E}[(e_{s_2} - \bar{e}_{s_2})^2]$$

5 Find $\hat{c}_1$ that minimizes $Var(e_{s_1}) + Var(e_{s_2})$,

$$\min_{c1 \in \{1,...,L\}} Var(e_{s_1}) + Var(e_{s_2})$$

Figure 3.1 Algorithm 1: GPR image segmentation by trace energy.

RR_i^T is the cross-correlation matrix of R and R_i,

where R and R_i are the **row** FFTs of r and r_i

$$R(n,k) = F_m\{r(n,m)\}$$

3.2.1 Feature Vector Extraction

Feature extraction algorithm focuses on the common characteristics of pavement, the periodic reinforcement structure. It applies FFT on the rows of a GPR image and reduces the periodicity to corresponding spectral components for further processing.

3.2.2 Spectral Template Matching

The matching algorithm essentially computes the similarity between the image under test and each of the template resulted from feature extraction. The image under test is then categorized to the closest match.

3.3 Test on I74RP147-148

A test run on I74 RP147-148 is presented as follows. This section of road is selected because it not only has a number of patches but also a variety of pavement types.

3.3.1 Pavement Segmentation

The segmentation in Figure 3.4(a) roughly matches the results from manual inspection in (b). This result reduces the search area by about 20% since the focuses are on the first and last segment only.

3.3.2 Sample Selection

For demonstration purposes, we will be running the algorithm on the first segment. Ten 32-trace (32-inch) long samples are randomly selected from each of JRCP and PC GPR image sets according to the patch table from manual inspection (see Figure 3.5).

3.3.3 Feature Extraction and Template Construction

The spectral features are extracted from the samples to form the matching templates (see Figures 3.6 and 3.7).

3.3.4 Detection Results

As shown in Figure 3.8(a), around 80% of the PC patches are detected in the first JRCP segment, thus 20% of them are missed. From in Figure 3.8(b), out of all positive results, 83% are correct detection and 17% false alarms.

The first 2,800 feet of I-74 east bound reference post 147–148 was used to test the automated detection algorithm by comparing its results to manually classified ground truth. See Figure 3.4 where it shows the ambient pavement detection and the test area, which is approximately 2,800 feet of JRCP in the east bound driving lane before the bridge.

There are imperfection in the spatial accuracy of both ground truth and automated patch detection. Therefore, if the estimated interval of a patch from both methods overlaps at all, we call that event a "hit." Let P_{alg} be the set of patches estimated by the algorithm and P_{gt} be the set of ground truth patches. A patch is actually the interval of trace numbers that are contained in the patch. Then P_{hit} is the set of patches where

Algorithm 2: Spectral template construction

input : $\{r_i(n,m)\}$, a set of GPR images of size $N \times M$ from class H

output: $R_H(n,k)$, a spectral template for class H

1   initialization

2   **foreach** $r \in \{r_i(n,m)\}$ **do**

3   Normalize the range to $[0,1]$

4   Remove horizontal mean

5   Normalize image energy to 1

6   Compute $R_i(n,k)$, an M-point FFT on **rows**

$$R_i(n,k) = \mathcal{F}_m\{r_i(n,m)\}$$

7   Find $c^i_{u,v}$, the largest entry in the cross-correlation matrix $R_1(s,t)[R_i(n,k)]^T$

$$\max_{u \in U, v \in V} c^i_{u,v}, \quad c^i_{u,v} = C_i[u,v] \text{ where } C_i = R_1(s,t)[R_i(n,k)]^T$$

8   Define $\delta_i(-u,-v)$, the shift vector corresponding to the position of $c^i_{u,v}$

9   Compute $R'_i(n,k)$, the shifted spectrum

$$R'_i(n,k) = R_i(n,k) * \delta_i(x,y)$$

10   **end**

11   Compute $R_H(n,k)$, the template by averaging all the spectra

$$R_H(n,k) = \frac{1}{I}\sum_{i=1}^{I} R'_i$$

Figure 3.2   Algorithm 2: Spectral template construction.

Algorithm 3: Shifted spectral template matching

input : $\{R_{H_1}, R_{H_0}\}$, a set of two spectral templates from class H_1 and H_2; $r(n,m)$, a GPR image under test

output: $label \in \{H_1, H_0\}$, a label indicating the classification of the test image

1   initialization

2   Normalize the range of $r(n,m)$ to $[0,1]$

3   Remove horizontal mean

4   Normalize image energy to 1

5   Compute $R(n,k)$ for $r(n,m)$, an M-point FFT on **rows**

$$R(n,k) = \mathcal{F}_m\{r(n,m)\}$$

6   Compute $\{c_1, c_0\}$, the maximum cross correlations for classes $\{H_1, H_0\}$,

$$c_1 = \max_{u \in U, v \in V} c^1_{u,v}, \quad c^1_{u,v} = C_1[u,v] \text{ where } C_1 = R_{H_1}(s,t)[R(n,k)]^T$$

$$c_0 = \max_{u \in U, v \in V} c^0_{u,v}, \quad c^0_{u,v} = C_1[u,v] \text{ where } C_0 = R_{H_0}(s,t)[R(n,k)]^T$$

7   Decide

$$label : c_1 \underset{H_1}{\overset{H_2}{\lessgtr}} c_0$$

Figure 3.3   Algorithm 3: Shifted spectral template matching.

there is overlap between P_{alg} and P_{gt}. We use the notation $\#\{\cdot\}$ to denote the number of members in a set and a backslash to denote relative set complement. Then the following performance measures are defined:

$$Precision \equiv \#\{P_{hit}\}/\#\{P_{alg}\}$$

$$False\,Alarm\,Rate \equiv \#\{P_{alg}\backslash P_{hit}\}/\#\{P_{alg}\}$$
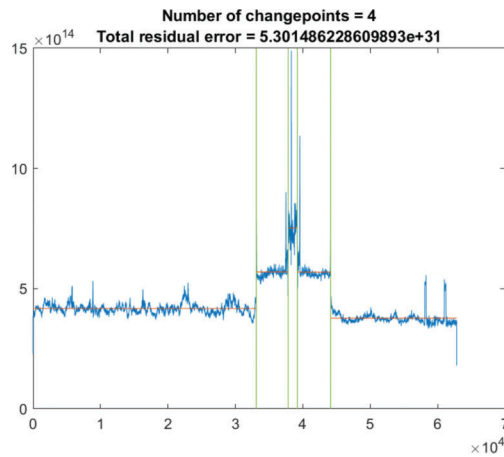
Figure 3.4 Pavement segmentation.
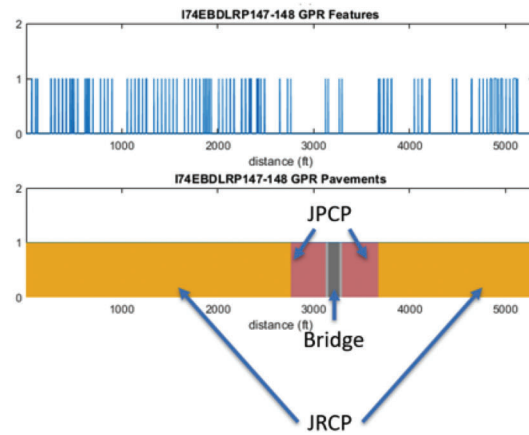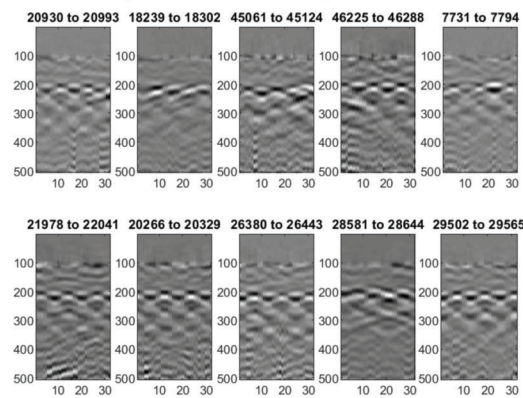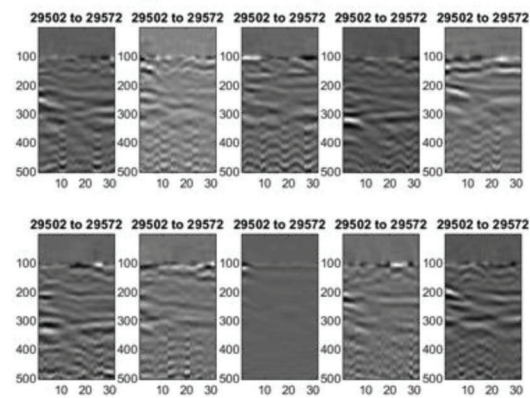
(a) JRCP samples.

(b) PC samples.

Figure 3.5 Samples selected.
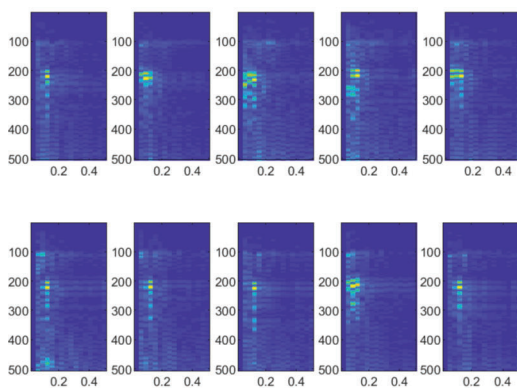
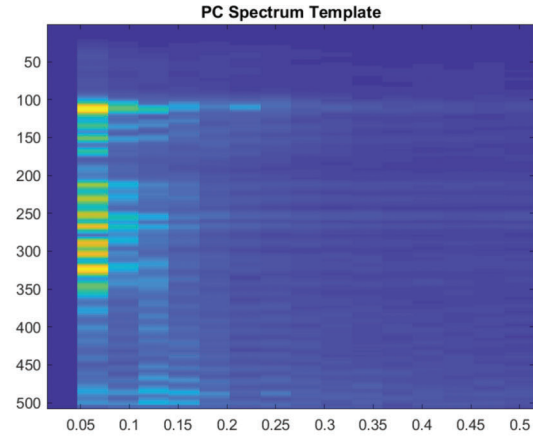(a) Corresponding spectra of JRCP samples.
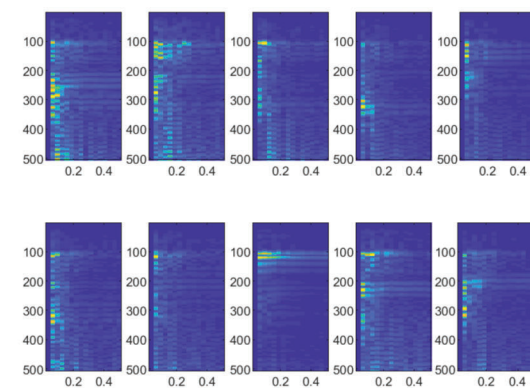
(b) Corresponding spectra of PC samples.

Figure 3.6 Spectra of selected samples.
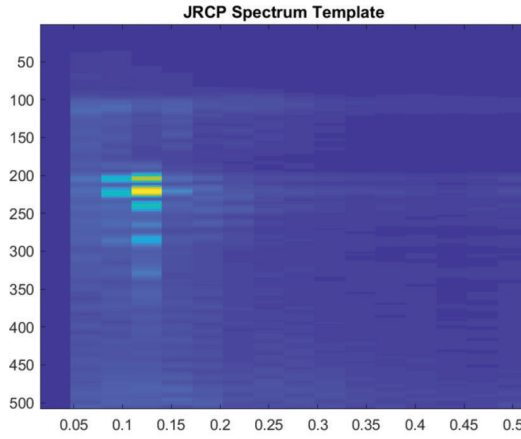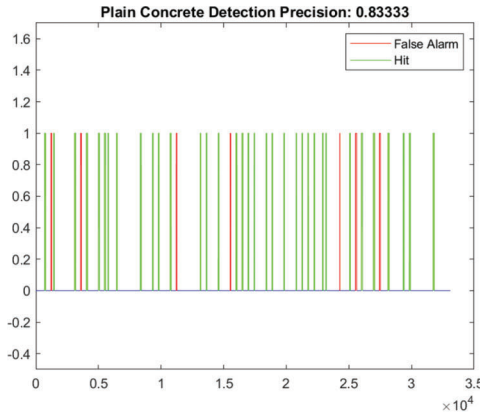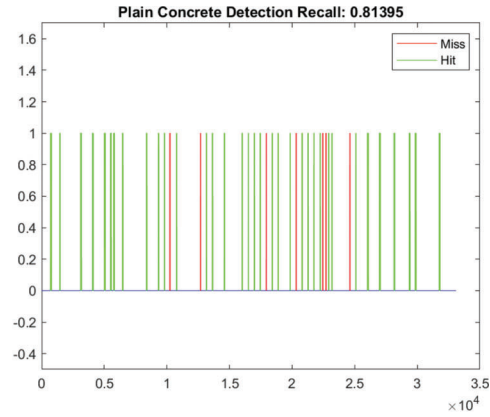
(a) JRCP spectral template.

(b) PC spectral template.

Figure 3.7 Spectral templates.

(a) Plain concrete precision rate.

(b) Plain concrete recall rate.

Figure 3.8 Detection results.

$$Recall \equiv {}^{\#\{P_{hit}\}}\!/\!_{\#\{P_{gt}\}}$$
$$Miss\ Rate \equiv {}^{\#\{P_{gt}\backslash P_{alg}\}}\!/\!_{\#\{P_{gt}\}}$$

Results are given in Figure 3.8 where we see a precision rate of approximately 83% and a recall rate of 81%.

4. GPR INSPECTION VIEWER AND DATA FUSION

During this project two software tools are developed in MATLAB to facilitate the patch locating process, GPR Inspection Viewer and Pavement Stats Viewer. The following subsections focus on how an operator can take advantage of the tools.

4.1 GPR Inspection Viewer

GPR Inspection Viewer is designed specifically for visualizing GPR profiles. It enables the operator to analyze pavement data with accurate GPS shown alongside. The software uses the algorithm described in the previous section and identifies potential plain concrete patches embedded in reinforced concrete pavement. It marks the detected targets and generates a corresponding patch table which the operator can further validate by comparing with other statistics.

4.1.1 Load GPR Files

Figure 4.1 shows the software interface. Clicking on the "Select File" button on top left will bring up a file selection window where the operator finds the "dzt" file under test. Then click "Run" on bottom left to load and display the data.

4.1.2 Display GPR Data

After selecting the pavement section under test, click "Run" to display data in the axes. Figure 4.2 shows an example of running two-channel dataset. Dragging the slider at the bottom allows the operator to go through the data from the start to end.
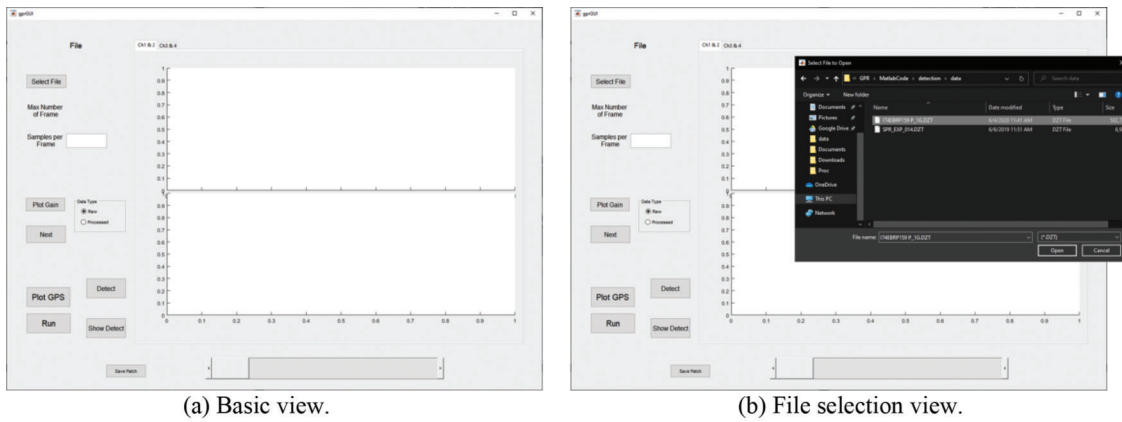
(a) Basic view.

(b) File selection view.

Figure 4.1 GPR Inspection Viewer.
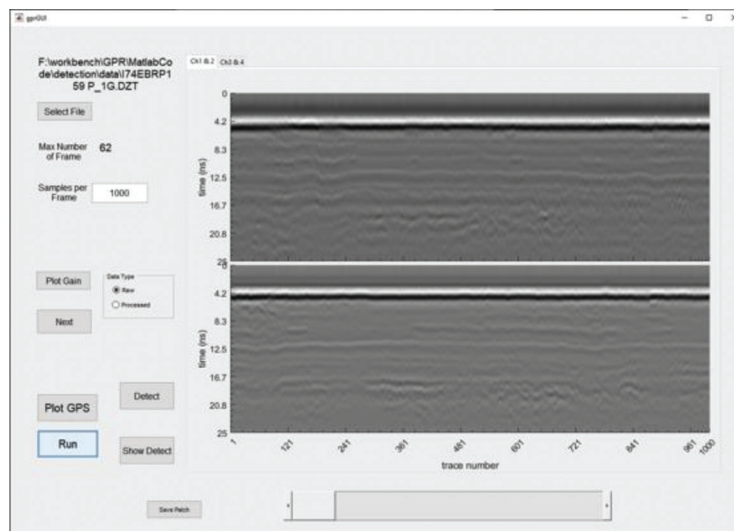
Figure 4.2 GPR profile.

4.1.3 Display GPS Data

With the GPR data shown in the axes, the operator will also be able to see the corresponding GPS tracking data alongside simply by clicking the "Plot GPS" button (see Figure 4.3).

4.2 Pavement Stats Viewer and Data Fusion

4.2.1 Pavement Stats Viewer

Pavement Stats Viewer is designed to present an overview of the pavement under test. The interface is shown in Figure 4.4. Select the desired pavement data from the drop-down menu on the top right, then click "Show Road Section" button. The map is plotted in the center axes with reference posts highlighted.

Now the operator will be able to select a mile of road (between two adjacent reference posts) and analyze its

detailed statistics closely. Figure 4.5 showcases the data from I74 Eastbound RP 147-148 driving lane.

4.3 Patch Table and Data Fusion

A patch table comparison was made between one made by inspecting GPR data and another made by thresholding a function of left and right wheel path IRI computed from the Waylink laser data. The road covered is the driving lanes of I-74 east and west bound between reference posts 157 and 164 (seven miles).

The patch tables are graphically compared in Figure 4.6 through Figure 4.12 on the following pages. Each figure covers a one mile segment of the east bound lanes. We note immediately that there are an order of magnitude more patches in the GPR data than in the IRI thresholded laser data. The 5-meter fusion rule pulls out patches in both, which appear to be failing according to roughness.
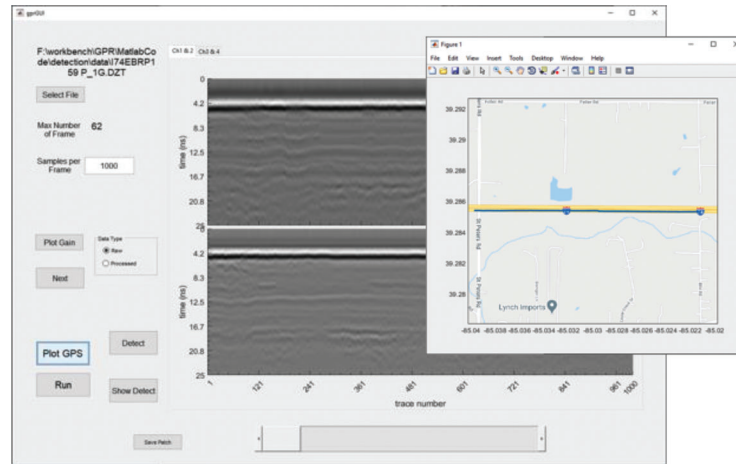
Figure 4.3 Plot GPS tracking data in GPR Inspection Viewer.
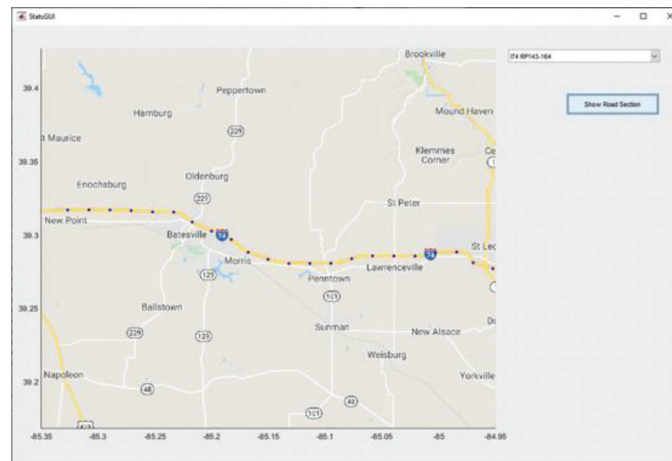
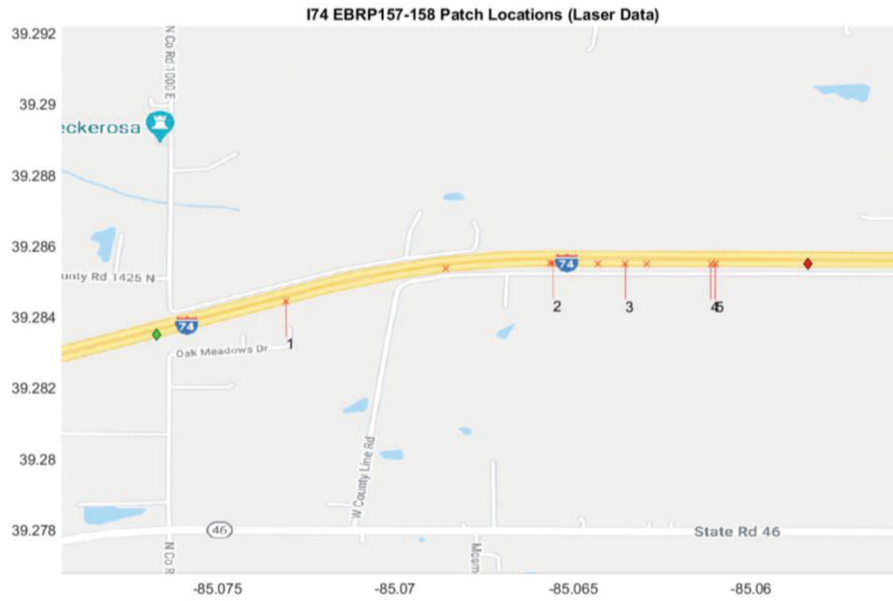**Figure 4.4** Pavement Stats Viewer.
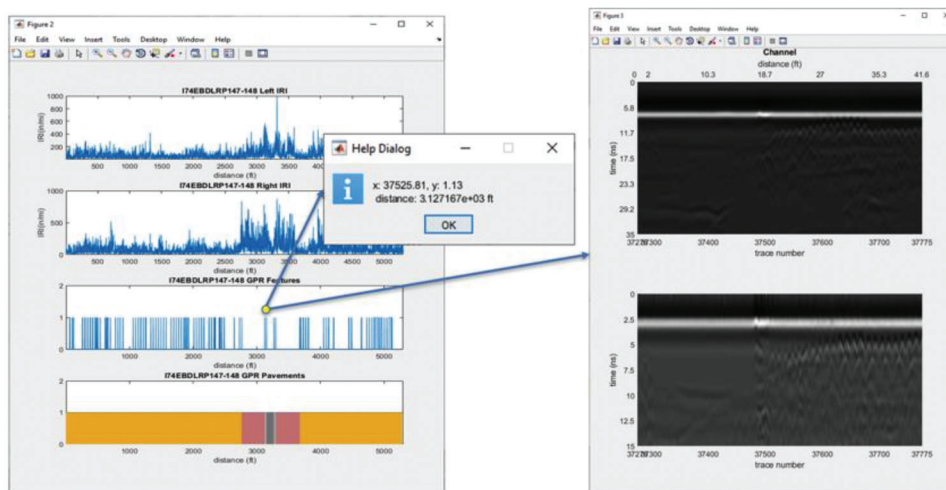
Figure 4.5 Detailed pavement statistics.

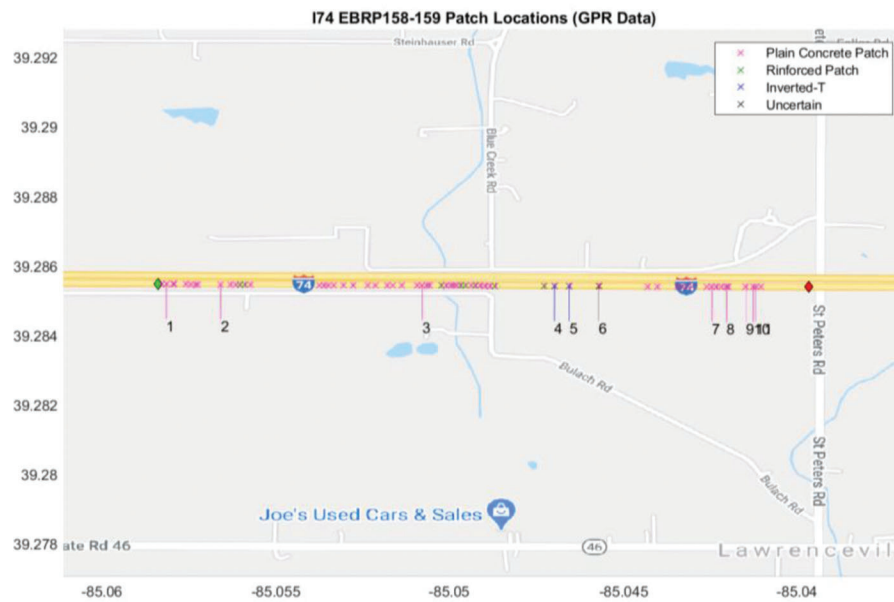(a) Laser patch table IRI threshold = 300.

(b) GPR patch table.

Figure 4.6 I74 Eastbound RP 157–158 (numbered patches indicate where (a) and (b) agree to within 5 m).
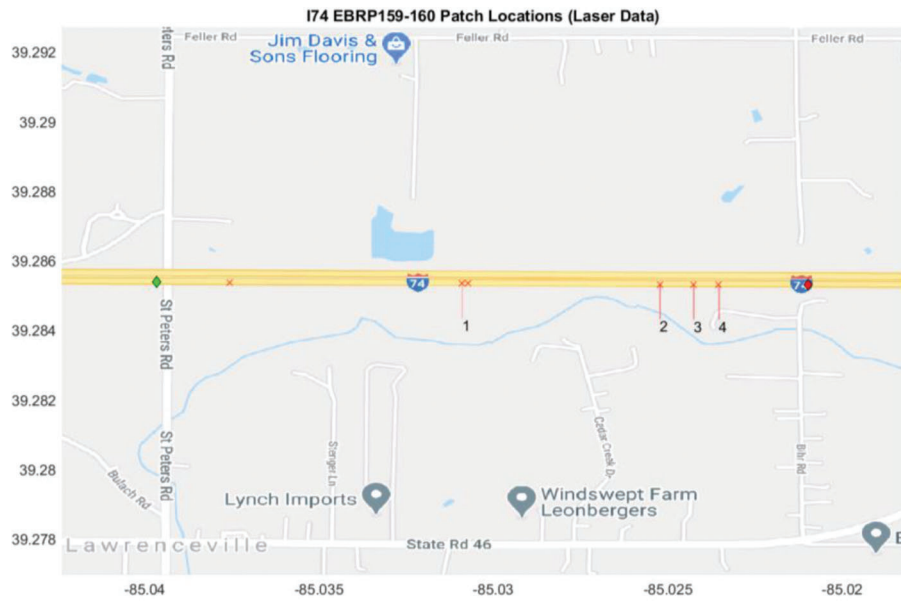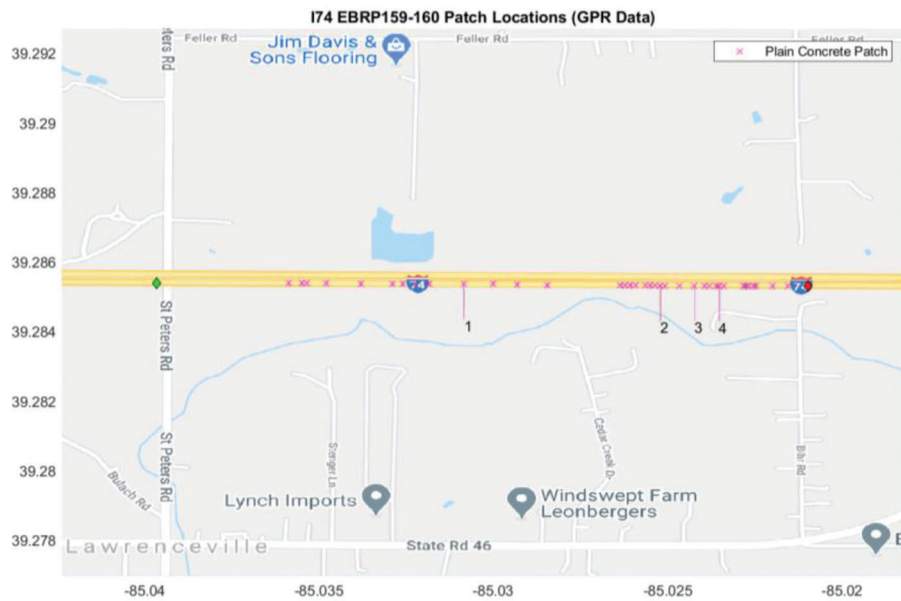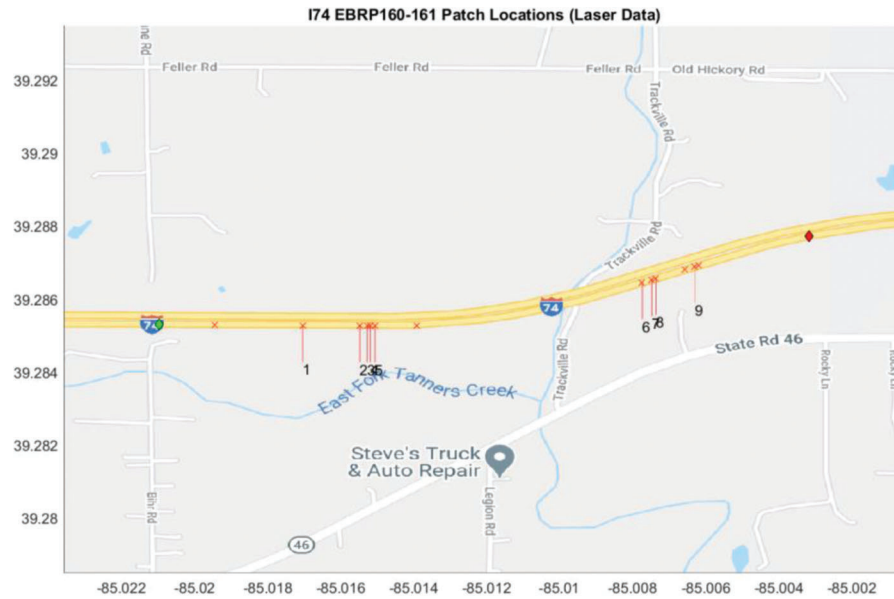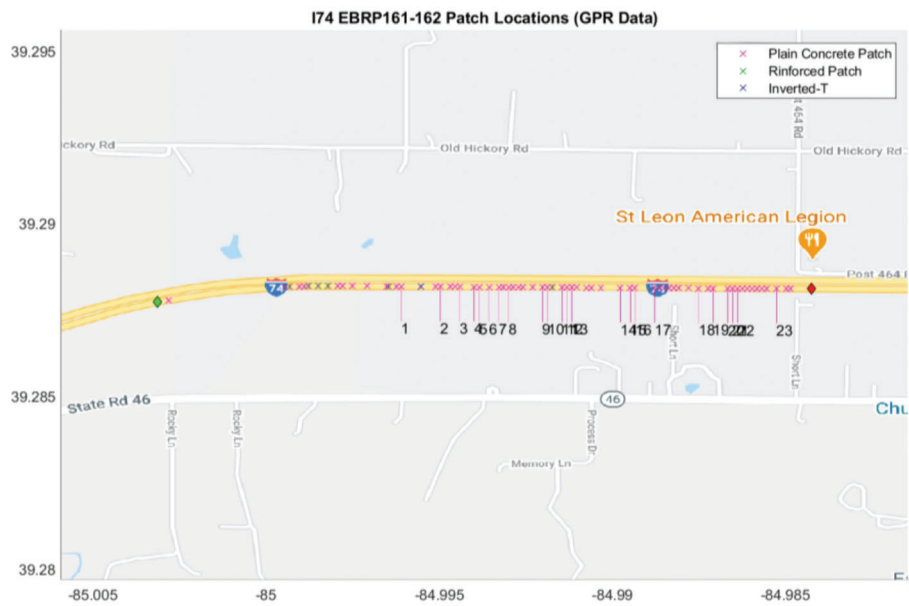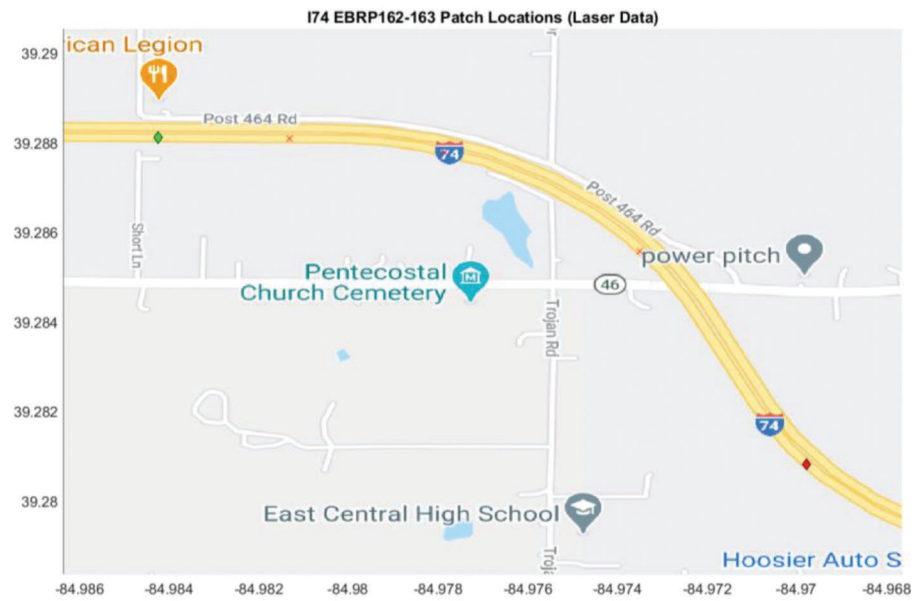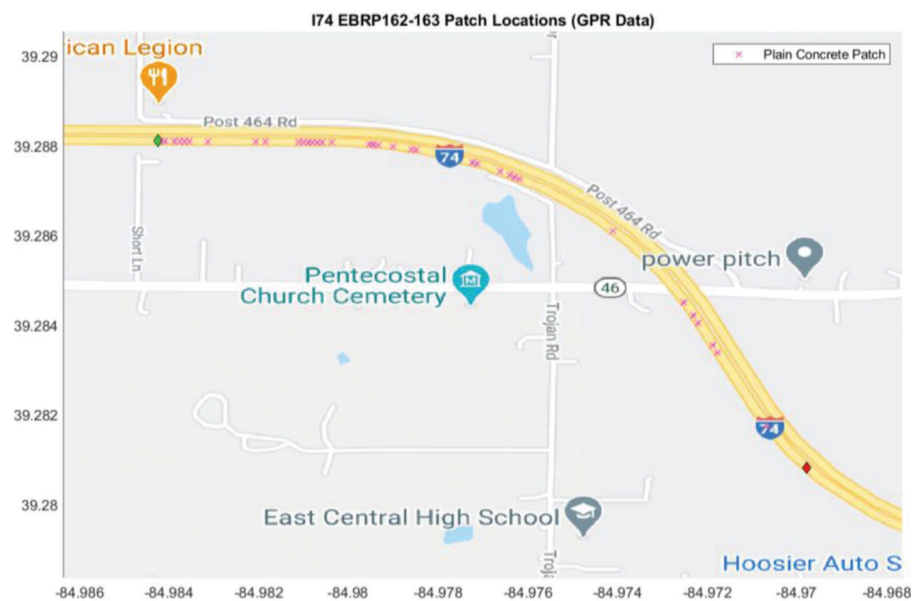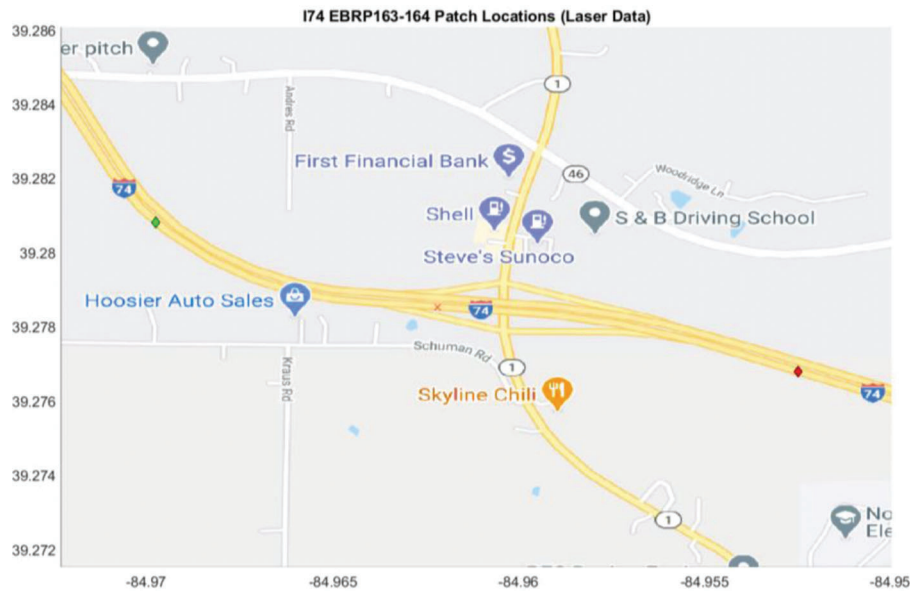
(a) Laser patch table IRI threshold = 300.

(b) GPR patch table.

Figure 4.7 I74 Eastbound RP 158–159 (numbered patches indicate where (a) and (b) agree to within 5 m).

(a) Laser patch table IRI threshold = 300.

(b) GPR patch table.

Figure 4.8 I74 Eastbound RP 159–160 (numbered patches indicate where (a) and (b) agree to within 5 m).

(a) Laser patch table IRI threshold = 300.

(b) GPR patch table.

Figure 4.9 I74 Eastbound RP 160–161 (numbered patches indicate where (a) and (b) agree to within 5 m).

(a) Laser patch table IRI threshold = 300.

(b) GPR patch table.

Figure 4.10 I74 Eastbound RP 161–162 (numbered patches indicate where (a) and (b) agree to within 5 m).
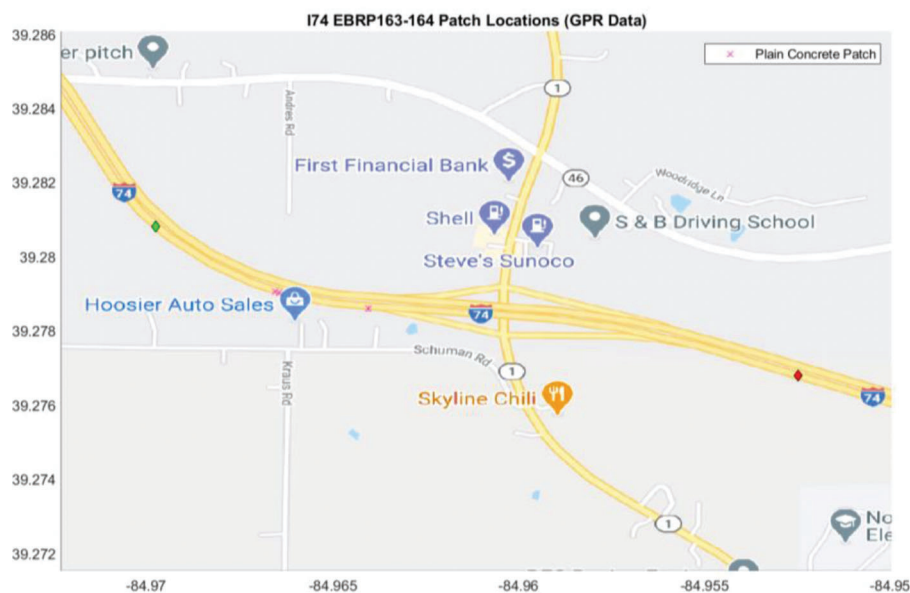
(a) Laser patch table IRI threshold = 300.

(b) GPR patch table.

Figure 4.11 I74 Eastbound RP 162–163 (numbered patches indicate where (a) and (b) agree to within 5 m).

(a) Laser patch table IRI threshold = 300.

(b) GPR patch table.

Figure 4.12 I74 Eastbound RP 163–164 (numbered patches indicate where (a) and (b) agree to within 5 m).

5. CONCLUSIONS

In this research the problem considered was to develop practical methods to detect, locate, and classify patches in concrete and asphalt-on-concrete pavements using data taken from ground penetrating radar (GPR) and the WayLink 3D Imaging System effectively fusing the information from the below pavement and above pavement sensing systems. In particular, the project sought to develop a patching table for "inverted-T" patches, which were not constructed to current best practices in that they did not use dowel bars to transfer load from pavement to patch to pavement. Inverted-T patches typically used "ears" undercut below the existing good pavement as an attempt to transfer load. They were originally recommended in situations where dowels could not be used and still maintain a relatively small patch, e.g., if the condition of pavement on either side of the patch location could not support dowels.

The Oklahoma State team considered visual methods for pavement patch detection. Several deep learning architectures were applied including object detection methods (SSD300 and Mark R-CNN) and image segmentation methods (U-Net). The results based solely on imaging were inconclusive as expected and some reasons, including a very limited training dataset, were hypothesized for this. Later, a method based on threshold international roughness index (IRI) values computing on a 12-foot window was used to localize pavement distress, particularly as seen by patch settling. This method was far more promising.

The Purdue team developed algorithms for segmentation of the GPR data and for classification of the ambient pavement and the locations and types of patches found in it. The results so far are promising, but far from perfect with relatively high rate of false alarms.

An integrated patching table was constructed for a seven mile segment of I-74 data by fusing the laser and GPR patching tables using an "agree-within-5-meters" test. The laser patching table was based on thresholding IRI and the GPR table from pattern matching on GPR images. The GPR table has an order of magnitude more entries in it and the laser table is used to reduce that number to those with evidence of failure (via observed roughness). With current GPR technology it does not appear to be feasible to reliably discriminate between inverted-T patches and other plain concrete and non-reinforced patches. This is because reinforcing steel used deep in an inverted-T patch is not reliably detected due to low signal-to-noise ratio and the fact that the absence of dowels in a patching application (which might indicate inverted-T) is also difficult to detect when using a transverse E-field GPR moving longitudinally down the road. New 3D GPR technologies may be able to solve this problem.

REFERENCES

ASTM International. (2019). *ASTM D6432-19 standard guide for using the surface ground penetrating radar method for subsurface investigation.* https://doi.org/10.1520/D6432-19

Augustaukas, R., & Lipnickas, A. (2019). Pixel-wise road pavement defects detection using U-net deep neural network. *2019 10th IEEE international conference on intelligent data acquisition and advanced computing systems: Technology and applications (IDAACS* (pp. 468–471). https://doi.org/10.1109/IDAACS.2019.8924337

Blight, R. J. (2009). *Composite pavement rehabilitation techniques* [PowerPoint slides]. New Jersey Department of Transportation. http://www.state.nj.us/transportation/eng/pavement/pdf/Composite0709.pdf

Brown, A. (2017, November 2). *Introduction to object detection & image segmentation* [PowerPoint slides]. NVIDIA. Accessed October 29, 2020, from https://on-demand.gputechconf.com/gtcdc/2017/presentation/dc7217-abel-brown-deep-learning-object-detection-and-segmentation.pdf

Buyukozturk, O. (1997). Electromagnetic properties of concrete and their significance in nondestructive testing. *Transportation Research Record: Journal of the Transportation Research Board*, *1574*(1), 10–17. https://doi.org/10.3141/1574-02

Cao, X., Wang, P., Meng, C., Bai, X., Gong, G., Liu, M., & Qi, J. (2018). Region based CNN for foreign object debris detection on airfield pavement. *Sensors*, *18*(3), 737. https://doi.org/10.3390/s18030737

Chen, V., & Chou, E. (2018). *Practical object detection and segmentation* [PowerPoint slides]. Accessed July 29, 2020, from http://cs231n.stanford.edu/slides/2018/cs231n_2018_ds06.pdf

Daniels, D. J. (2004). Modulation techniques. In D. J. Daniels (Ed.), *Ground Penetrating Radar–2nd Edition* (pp. 185–246). The Institution of Engineering and Technology.

Drnevich, V. P., Lovell, J., Tishmack, J., & Yu, X. (2001, September). Temperature effects on dielectric constant determined by time domain reflectometry. In *TDR 2001: Innovative Applications of TDR Technology* [Symposium]. Infrastructure Technology Institute, Northwestern University, Evanston, IL.

Girshick, R., Donahue, J., Darrell, T., & Malik, J. (2014). *Rich feature hierarchies for accurate object detection and semantic segmentation* [PDF file]. https://arxiv.org/pdf/1311.2524.pdf

GSSI. (2017). *Concrete handbook* (MN72-367 Rev H) [PDF file]. Geophysical Survey Systems, Inc. https://www.geophysical.com/wp-content/uploads/2017/10/GSSI-Concrete-Handbook.pdf

Hall, K. T., & Darter, M. I. (1994). Improved methods for asphalt-overlaid concrete pavement back calculation and evaluation. In A. Bush, H. Q. Von Quintus, & G. Baladi (Eds.), *Nondestructive testing of pavements and back calculation of moduli: Second volume* (pp. 83–102). American Society for Testing and Materials. https://doi.org/10.1520/STP18143S

Han, S., Yoo, J., & Kwon, S. (2019). Real-time vehicle-detection method in bird-view unmanned-aerial-vehicle imagery. *Sensors*, *19*(18), 3958. https://doi.org/10.3390/s19183958

Harris, D. A. (2006). *Pavement thickness evaluation using ground penetrating radar* (Order No. 3260019) [Doctoral thesis]. ProQuest Dissertations and Theses Global. https://www.proquest.com/dissertations-theses/pavement-thickness-evaluation-using-ground/docview/305280875/se-2?accountid=13360

He, K., Gkioxari, G., Dollár, P., & Girshick, R. (2018). *Mask R-CNN.* https://arxiv.org/pdf/1703.06870v3

INDOT. (2013). *Indiana Department of Transportation–Design manual, Chapter 601: Pavement design* [PDF file]. Indiana Department of Transportation. https://www.in.gov/dot/div/contracts/design/Part%206/Chapter%20601%20-%20Pavement%20Design.pdf

Kang, K., Yoon, S., Patel, S., Yoon, Y., Ji, Y., & Hastak, M. (2015) *Enhanced treatment selection for reflective joint cracking in composite pavements* (Joint Transportation Research Program Publication No. FHWA/IN/JTRP-2015/21). West Lafayette, IN: Purdue University. http://dx.doi.org/10.5703/1288284316006

Lamptey, G., Ahmad, M. Z., Labi, S., & Sinha, K. C. (2005). *Life cycle cost analysis for INDOT pavement design procedures* (Joint Transportation Research Program Publication No. FHWA/IN/JTRP-2004/28). West Lafayette, IN: Purdue University. https://doi.org/10.5703/1288284313261

Lau, S. L. H., Chong, E. K. P., Yang, X., & Wang, X. (2020). *Automated pavement crack segmentation using U-Net-based convolutional neural network* (arXiv:2001.01912 [cs.CV]). https://doi.org/10.1109/ACCESS.2020.3003638

Li, G., Ma, B., He, S., Ren, X., & Liu, Q. (2020). Automatic tunnel crack detection based on U-Net and a convolutional neural network with alternately updated clique. *Sensors*, *20*(3), 717. https://doi.org/10.3390/s20030717

Liu, W., Anguelov, D., Erhan, D., Szegedy, C., Reed, S., Fu, C.-Y., & Berg, A. C. (2016). SSD: Single shot multibox detector. In B. Leibe, J. Matas, N. Sebe, & M. Welling (Eds.), *Computer Vision–ECCV 2016*, Vol 9905, 21–37. Springer, Cham. https://doi.org/10.1007/978-3-319-46448-0_2

Majidifard, H., Adu-Gyamfi, Y., & Buttlar, W. G. (2020). Deep machine learning approach to develop a new asphalt pavement condition index. *Construction and Building Materials*, Vol 247, 118513. https://doi.org/10.1016/j.conbuildmat.2020.118513

Maser, K. R. (2002). Use of ground-penetrating radar data for rehabilitation of composite pavements on high-volume roads. *Transportation Research Record: Journal of the Transportation Research Board*, *1808*(1), 122–126. https://doi.org/10.3141/1808-14

Maser, K. R. (2003, April 25). *Non-destructive measurement of pavement layer thickness* (Caltrans No. 65A0074). California Department of Transportation.

Matcha, A. C. N. (2020). *A 2020 guide to semantic segmentation*. Accessed July 20, 2020, from https://nanonets.com/blog/semantic-image-segmentation-2020/#:~:text=Frequency%20weighted%20IOU&text=If%20one%20class%20dominates%20most,class%20region%20in%20the%20dataset

McDaniel, R. S. (2020). *Best practices for patching composite pavements* (Joint Transportation Research Program Publication No. FHWA/IN/JTRP-2020/05). West Lafayette, IN: Purdue University. https://doi.org/10.5703/1288284317116

MoDOT. (2018, April). Section 613: Pavement repair. In *Missouri standard specifications for highway construction* (4th ed., pp. 321–330). https://www.modot.org/sites/default/files/documents/2017_MO_Std_Spec_Gen_Supp_%28April%202018%29.pdf

Mongkhonthanaphon, S., & Limpiyakorn, Y. (2018). Classification of titanium microstructure with fully convolutional neural networks. *Journal of physics: Conference series*, *1195*(012022). https://doi.org/10.1088/1742-6596/1195/1/012022

Naghavi, S. H., & Pourreza, H. (2018, October). Real-time object detection and classification for autonomous driving. *2018 8th International Conference on Computer and Knowledge Engineering (ICCKE)* (pp. 274–279). https://doi.org/10.1109/ICCKE.2018.8566491

Noureldin, A. S., Zhu, K., Li, S., & Harris, D. (2003). Network pavement evaluation with falling-weight deflectometer and ground-penetrating radar. *Transportation Research Record: Journal of the Transportation Research Board*, *1860*(1), 90–99. https://doi.org/10.3141/1860-10

Porubiaková, A., & Komačka, J. (2015). A comparison of dielectric constants of various asphalts calculated from time intervals and amplitudes. *Procedia Engineering*, *111*, 660–665.

Ramo, S., Whinnery, J. R., & Van Duzer, T. (1984). *Fields and waves in communication electronics* (2nd ed.). John Wiley and Sons.

Ren, S., He, K., Girshick, R., & Sun, J. (2016). *Faster R-CNN: Towards real-time object detection with region proposal networks* [PDF file]. https://arxiv.org/pdf/1506.01497.pdf

Ronneberger, O., Fischer, P., & Brox, T. (2015). *U-Net: Convolutional networks for biomedical image segmentation*. https://arxiv.org/abs/1505.04597v1

Sachan, A. (2017). *Zero to hero: Guide to object detection using deep learning: Faster R-CNN, YOLO, SSD*. Accessed July 19, 2020, from https://cv-tricks.com/object-detection/faster-r-cnn-yolo-ssd/

Singh, J., & Shekhar, S. (2018). *Road damage detection and classification in smartphone captured images using mask R-CNN*. https://arxiv.org/abs/1811.04535

Smith, G. S., & Scott, W. R., Jr. (1989, July). A scale model for studying ground penetrating radars. *IEEE Transactions on Geoscience and Remote Sensing*, *27*(4), 358–363. https://doi.org/10.1109/36.29554

Travassos, X. L., Avila, S. L., Adriano, R. L. da S., & Ida, N. (2018). A review of ground penetrating radar antenna design and optimization. *Journal of microwaves, optoelectronics and electromagnetic applications*, *17*(3), 385–402. https://doi.org/10.1590/2179-10742018v17i31321

Wang, Y., Wang C., & Zhang, H. (2017). Combining single shot multibox detector with transfer learning for ship detection using Sentinel-1 images. *2018 IEEE International Geoscience and Remote Sensing Symposium* (pp. 8444–8447). IEEE International.

Wang, W., Wu, B., Yang, S., & Wang, Z. (2018). Road damage detection and classification with faster R-CNN. In *2018 IEEE International Conference on Big Data (Big Data)* (pp. 5220–5223). The Institute of Electrical and Electronics Engineers. https://doi.org/10.1109/BigData.2018.8622354

Whiting, N. M., Panchmatia, P., & Olek, J. (2016). *Concrete pavement joint deterioration* (Joint Transportation Research Program Publication No. FHWA/IN/JTRP-2016/02). West Lafayette, IN: Purdue University. http://dx.doi.org/10.5703/1288284316225

Zhang, Q., Chang, X., & Bian, S. B. (2020). Vehicle-damage-detection segmentation algorithm based on improved mask RCNN. *IEEE Access*, *8*, 6997–7004. https://doi.org/10.1109/ACCESS.2020.2964055

APPENDICES

Appendix A. Oklahoma State Subcontract Report

Appendix B. Metal Plate Experiment at Research Division

# APPENDIX A. OKLAHOMA STATE SUBCONTRACT REPORT

A.1   Introduction

Indiana pavements are generally categorized as asphalt (flexible), concrete (rigid), or asphalt-over-concrete (composite) pavements (Lamptey et al., 2005). In the year 2001 the entire state highway network was approximately 8% concrete, 28% asphalt-on-concrete, and 64% asphalt. This project primarily concerns patch locations in concrete and asphalt-on concrete pavements in the length of many thousands of miles. It is difficult from visual inspection alone to determine the health of an existing pavement patch. Furthermore, concrete pavement patches are frequently overlaid with asphalt, effectively concealing the location until failure is well-underway.

The recommended practice for concrete patching (Figure A.1) is the use of dowel rods on either side of patch in order to transfer load from the patch to the existing pavement. This is designed to prevent "rocking" and it's associated deleterious effects. However, in the past, in cases where dowels could not be used, e.g., if the old slab was deteriorated or rubblized, the practice was to use "Inverted-T" patches (Figure A.2). This particular type of concrete patch has been used in the past before the installation of asphalt overlay and has been found to be problematic in Indiana regarding its performance. Since the "Inverted-T" patches are not connected with the existing concrete pavement with dowel bars, the "Inverted-T" patches could be unstable, such as having more settlement than existing concrete pavement under traffic loading. This uneven settlement leads to failures including dip and reflective transverse cracking in the asphalt overlay around the "Inverted-T" patches (Figure A.3). Therefore, it is desired to identify locations of the "Inverted-T" patches from the highway network to address "Inverted-T" patches related distresses.

However, from Figure A.1 and Figure A.2, it is clear that the distinction cannot be made between these different types of patches from a visual observation of a structurally sound patch. Furthermore, the "Inverted-T" shown in Figure A.2 is covered by a continuous layer of asphalt further masking the patch location. Therefore, it is challenging to determine "Inverted-T" concrete patch locations based on visual observation only.

In this research, the problem considered is to develop practical methods to locate and classify the "Inverted-T" patches on composite pavements (Figure A.2) and to deliver a corresponding patching table for engineers to fix the issues related to "Inverted-T" patches. The Indiana Department of Transportation (INDOT) uses WayLink 3D Laser Imaging System and ground penetrating radar (GPR) system to collect field data from the surface and underneath of pavement with a purpose of creating a patching and classification table. The 3D imaging system will create a 1-mm resolution image of the pavement surface and develop an artificial intelligence based technique to locate the "Inverted-T" patch and narrow the patch search area in order to improve efficiency in using computational and human resources for analyzing the GPR data. The OSU team focuses on the use of the 3D pavement surface data and subsequent analysis while the Purdue team focuses on the application of GPR data and the relevant analysis. Results from the two analyses by the two teams will be combined through a data fusion task to create a patching table database for INDOT. This final report summarizes the completed work by the OSU team.

PLAN

SECTION B-B

SECTION A-A
SUBBASE REMOVAL

SECTION A-A
NO SUBBASE REMOVAL
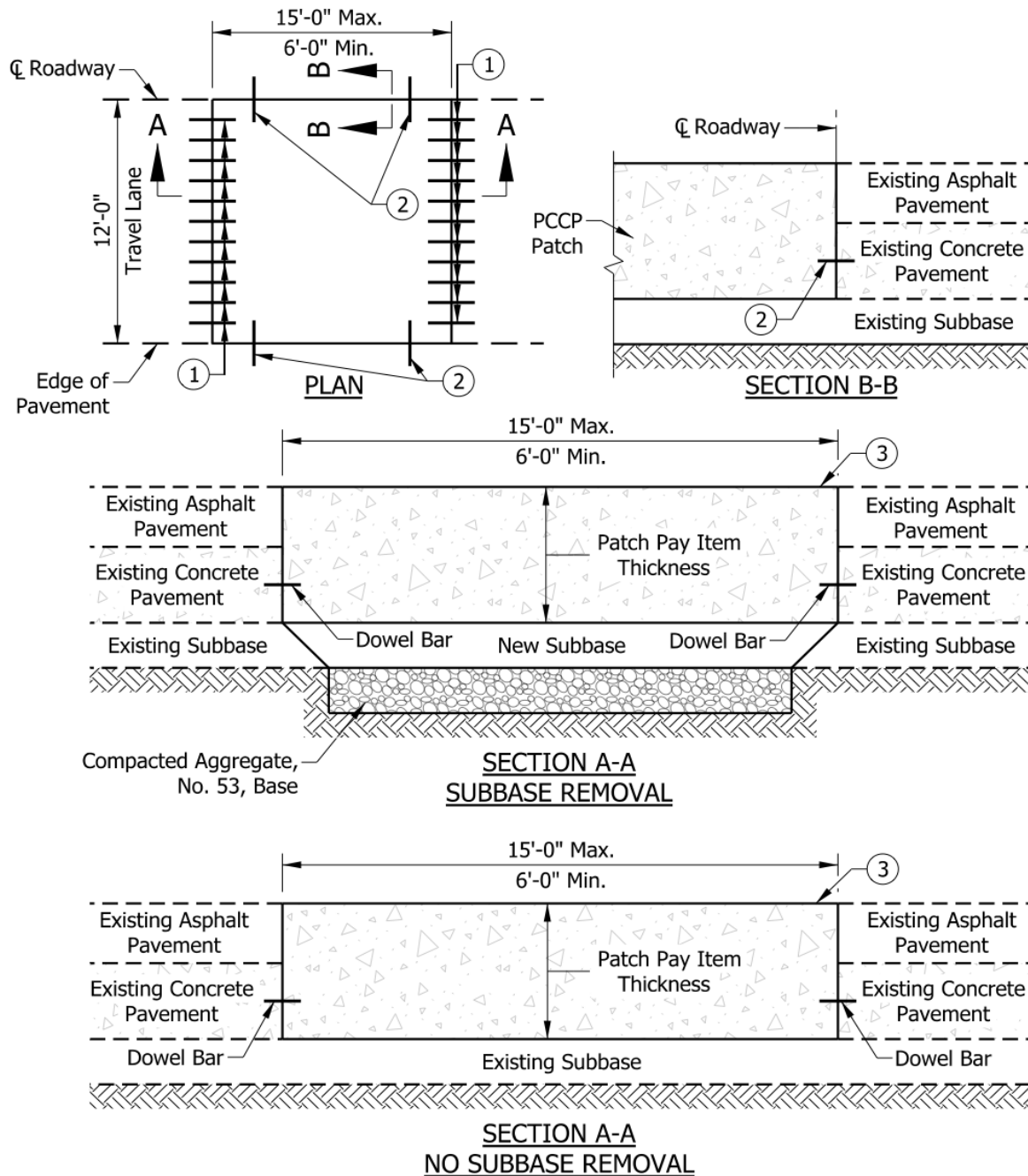
NOTES:

(1) See Standard Drawing E 503-CCPP-01 for Dowel Bar detail.

(2) Tie bar as specified. See Standard Drawing E 503-CCPJ-08 for Retrofit Tie Bar details.

(3) For any subsequent overlay mill, then overlay with HMA Surface course.

Figure A.1 Full-depth concrete patch in composite pavements showing dowel rods (INDOT, 2013).

PLAN

SECTION A-A
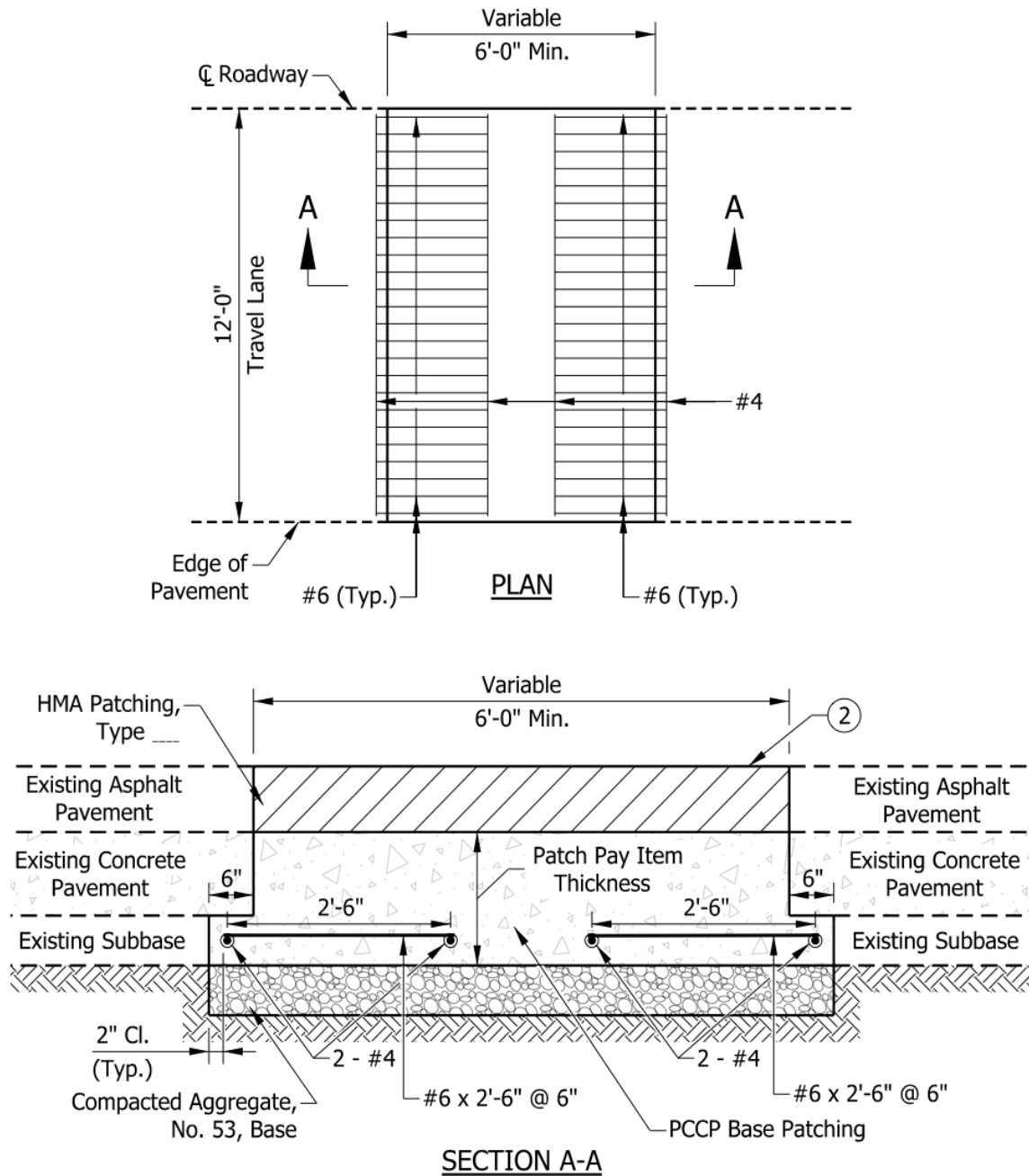
NOTES:

1. The assembly of #4 and #6 bars should be installed at half the depth of the existing subbase.

② For any subsequent overlay mill, then overlay with HMA Surface course.

Figure A.2 Full-depth composite patch, Inverted-T patching (INDOT, 2013).

Figure A.3 Example Inverted-T patching.

A.2   Data Collection

The WayLink 3D laser imaging system with both hardware sensors and software solutions is used for automated pavement condition survey (including cracking, rutting, roughness, texture, patching, pothole, and roadway geometry) at 1-mm resolution at speeds up to 60 mph (Figure A.4). The working principle used in the 3D vehicle platform is based on laser triangulation to determine the height information on a surface.

Figure A.4 WayLink 3D laser imaging system.

In the last week of March 2019, the OSU team sent a technician to INDOT to tune the 3D laser imaging system with 4K resolution to collect pavement images at 1-mm resolution. By the end of May 2019, 36 data collections (as summarized in Table A.1) with a total length of 304.3 miles had been conducted by INDOT on routes with "Inverted-T" patching using the 4K system. In February 2020, the 3D laser imaging system was upgraded to 8K system which collects more than 8,000 pixels in the transverse direction. Figure A.5 illustrates the example images from 4K and 8K systems that were collected from the same location: the images from 8K system shows higher quality with more details and less noises in 2D and 3D images. The INDOT conducted more data collections with the 8K system on I-65 and I-74 with a total length of 142.7 miles, as summarized in Table A.1. All the obtained data from the 3D laser imaging system was used to develop image library for "Inverted-T" patching detection using DL networks.

2D   3D
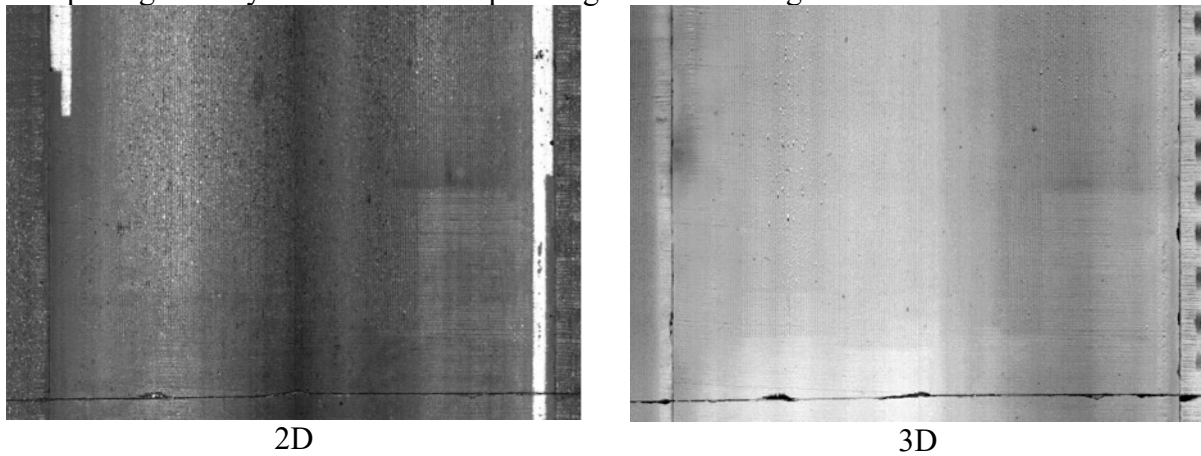
(a) 4K Images (March 2019)

2D   3D
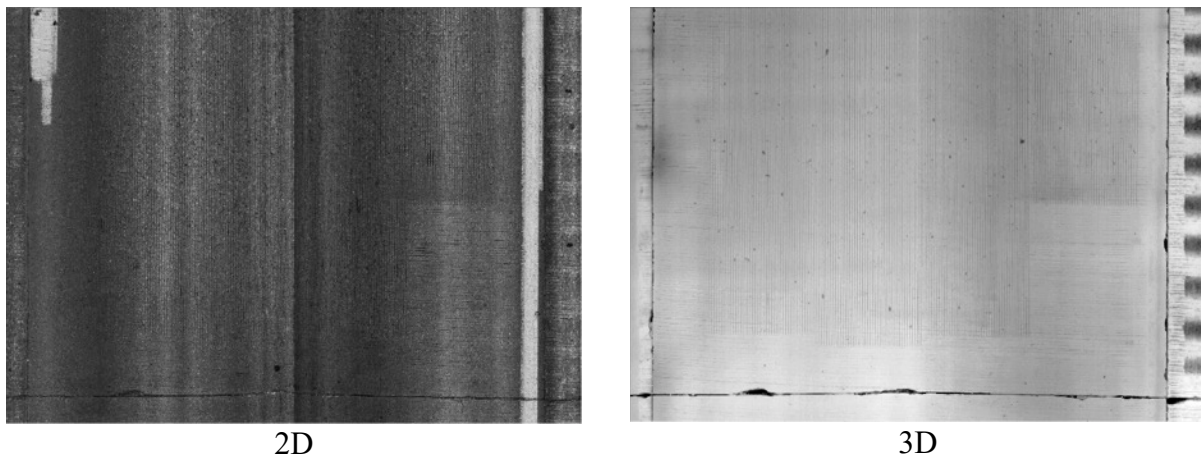
(b) 8K Images (March 2020)

Figure A.5 Example images from 4K and 8K systems.

Table A.1 Summary of Data Collections

ID		Data Collections	Start		End		Length (Mile)
			Latitude	Longitude	Latitude	Longitude	
4K (1 mm resolution)	1	I-65NBDL_NorthEnd-20190327.153235	40.191177	-86.567909	40.334988	-86.759109	14.3
	2	I-65NBDL_NorthEnd-20190327.180718	40.190392	-86.567184	40.339321	-86.76223	14.7
	3	I-65NBDL_SouthEnd-20190327.140107	40.049629	-86.491058	40.208801	-86.588631	12.4
	4	I-65NBPL_NorthEnd-20190327.163434	40.190853	-86.567657	40.335194	-86.759354	14.4
	5	I-65NBPL_SouthEnd-20190327.144403	40.048119	-86.489891	40.208843	-86.588959	12.5
	6	I-65SBDL_NorthEnd-20190327.155632	40.335453	-86.759895	40.195889	-86.572739	14
	7	I-65SBDL_SouthEnd-20190327.142055	40.20826	-86.588516	40.047531	-86.490952	12.5
	8	I-65SBPL_NorthEnd-20190327.173843	40.341629	-86.764198	40.199314	-86.575943	14.1
	9	LL 62 I-74 EBPL-20190531.131121	39.316071	-85.354912	39.27136	-84.939964	23.2
	10	LL 62 I-74 WBDL2-20190531.102905	39.273064	-84.937927	39.275517	-84.947296	0.5
	11	LL 62 I-74 WBDL-20190531.101539	39.273109	-84.938324	39.275185	-84.946342	0.5
	12	LL 62 I-74 WBPL-20190531.123431	39.272907	-84.935349	39.316795	-85.359596	23.7
	13	LL62 I-74 EBDL-20190531.111914	39.316177	-85.356644	39.273064	-84.939796	23.3
	14	LL62 I-74 WBDL 3-20190531.104216	39.27327	-84.931641	39.316765	-85.359123	23.9
	15	I-65SBPL_SouthEnd-20190327.150422	40.207832	-86.587723	40.051804	-86.492462	12.1
	16	I-94EBDL-20190327.102121	41.600525	-87.190575	41.628811	-87.019089	9.4
	17	I-465 RP-38+00 to RP-42+00 NBLN1B-20190428.101204	39.812721	-86.030891	39.893936	-86.052544	5.9
	18	I-465 RP-38+00 to RP-42+00 NBLN2-20190428.084345	39.809498	-86.030807	39.8915123	-86.05426	6.3
	19	I-465 RP-38+00 to RP-42+00 NBLN4-20190428.091602	39.807716	-86.030731	39.887669	-86.047729	5.7
	20	I-465 RP-38+00 to RP-42+00 SBLN1-20190428.092837	39.891232	-86.049911	39.810955	-86.031006	5.7
	21	I-465 RP-38+00 to RP-42+00 SBLN4-20190428.085752	39.89106	-86.049881	39.807308	-86.031158	6
	22	I-465 RP-38+00 to RP-42+00 NBLN1B-20190428.101204	39.812721	-86.030891	39.89396	-86.052544	5.9
	23	I-465 RP-38+00 to RP-42+00 NBLN2-20190428.084345	39.809498	-86.030807	39.895123	-86.05426	6.2
	24	I-465 RP-38+00 to RP-42+00 NBLN4-20190428.091602	39.807716	-86.030731	39.887669	-86.047729	6.2
	25	I-465 RP-38+00 to RP-42+00 SBLN1-20190428.092837	39.891232	-86.049911	39.810955	-86.031006	5.7
	26	I-465 RP-38+00 to RP-42+00 SBLN2-20190428.082454	39.898651	-86.060188	39.805737	-86.031311	6.8
	27	I-465 RP-38+00 to RP-42+00 SBLN4-20190428.085752	39.891052	-86.049881	39.807308	-86.031158	6
	28	I-65SBDL-20190327.131759	40.35479	-86.773071	40.349403	-86.769531	0.4
	29	I-65SBDL-20190327.132223	40.349258	-86.769424	40.299335	-86.718636	4.4
	30	I-65SBDL-20190327.132854	40.291843	-86.709114	40.288239	-86.70446	0.3
	31	I-65SBDL-20190327.133006	40.283154	-86.695045	40.26461	-86.65386	3
	32	I-65SBDL-20190327.133348	40.257751	-86.651176	40.253216	-86.646408	0.4
	33	I-65SBDL-20190327.133508	40.245663	-86.638458	40.241909	-86.63398	0.4
	34	I-65SBDL-20190327.133555	40.23909	-86.630516	40.235981	-86.62701	0.3
	35	I-65SBDL-20190327.133732	40.225563	-86.613342	40.221214	-86.607079	0.4
	36	I-65SBDL-20190327.133852	40.215294	-86.598572	40.185852	-86.563423	2.8
8K (0.5 mm resolution)	37	I65_NBDL-20200304.150707	40.052692	-86.492464	40.379115	-86.785221	28.2
	38	I65_SBDL-20200304.142711	40.444479	-86.843124	40.053915	-86.49321	33.6
	39	I-74 DL EB-20200608.103046	39.315998	-85.347969	39.276323	-84.950953	22.2
	40	I-74 DL WB-20200608.110017	39.276538	-84.950698	39.316272	-85.347877	22.2
	41	I-74 PL EB-20200609.092643	39.316058	-85.347467	39.276402	-84.951082	22.2
	42	I-74 PL WB-20200609.105423	39.280753	-85.092142	39.316255	-85.347316	14.3

A.3 Selection of DL Networks and Image Labeling

A.3.1 Selection of DL Networks

If the transverse cracks around "Inverted-T" patching are fully developed as shown in Figure A.3, the detection of "Inverted-T" patching can be treated as finding objects with two paralleled transverse cracks and a pavement section between them in obtained pavement images. Pavement 3D images collect height information and have demonstrated its advantages in pavement crack detection over 2D images. Therefore, object detection algorithms in imaging processing could be explored to automatically detect the pavement sections containing an "Inverted-T" patching using pavement 3D images.

In recent years, DL based object detection algorithms have achieved excellent performance in various applications, far surpassing more traditional computer vision methods as demonstrated with CrackNet developed by the OSU team. The Region-Convolutional Neural Network (R-CNN) was proposed in 2014 which applied a special type of CNN to locate and detect objects in images: the output is generally a set of bounding boxes that closely match each of the detected objects, as well as a class output for each detected object (Girshick et al., 2014). Figure A.6 shows a typical R-CNN output. Afterwards, the Fast R-CNN and Faster R-CNN were proposed to improve R-CNN in terms of improved training and testing speed while also increased detection accuracy (Girshick, 2014; Ren et al., 2016). However, these networks are not perfect for real-time object detector because they require long training time and multiple training phases.
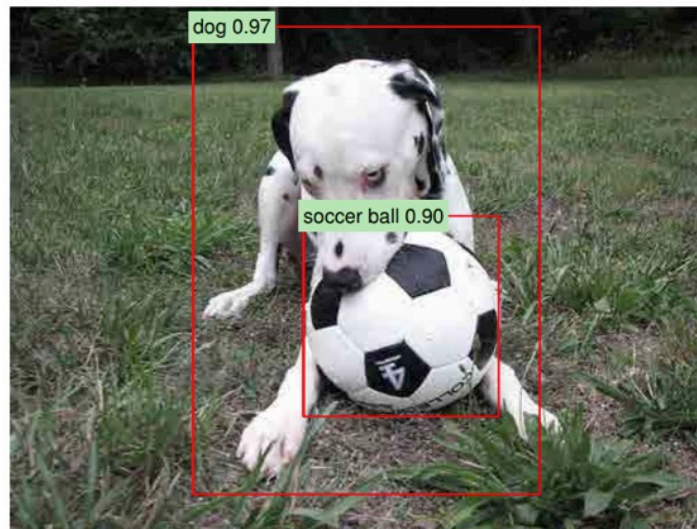
Figure A.6 Example output of R-CNN (Girshick et al., 2014).

Fortunately, in 2016, the Single Shot MultiBox Detector (SSD) was developed as one of the famous real-time object detection algorithms to address the bottlenecks of R-CNN and its successors (Liu et al., 2016). It outperforms Faster R-CNN and is easy to train and straightforward to integrate into systems that require a detection component. The SSD has been used for ship detection, vehicle detection, and autonomous driving (Han et al., 2019; Naghavi &

Pourreza, 2018; Wang et al., 2017). So, the SSD was firstly explored by the research team to detect "Inverted-T" patching from pavement 3D images.

For object detection in image processing, the SSD is faster in speed but lower in accuracy compared against Faster R-CNN (Sachan, 2017). The Mask R-CNN was proposed in 2018 and it extended the Faster R-CNN by adding a branch for predicting an object mask on each Region of Interest (RoI) in parallel with the existing branch for bounding box recognition (He et al., 2018). As shown in (Chen & Chou, 2018) Mask R-CNN shows better performance than SSD and Faster R-CNN for object detection. The Mask R-CNN has been used for vehicle damage detection, road damage detection, and foreign object debris detection on airfield pavement (Cao et al., 2018; Singh & Shekar, 2018; Zhang et al., 2020). Consequently, the Mask R-CNN was also selected to automatically detect "Inverted-T" patching from the pavement 3D images.

Lastly, image segmentation model was also explored to detect the "Inverted-T" patching. Unlike object detection models which only build a bounding box around each object in the image, image segmentation models create a pixel-wise mask for each object in the image. Figure A.7 shows the difference between object detection and image segmentation.
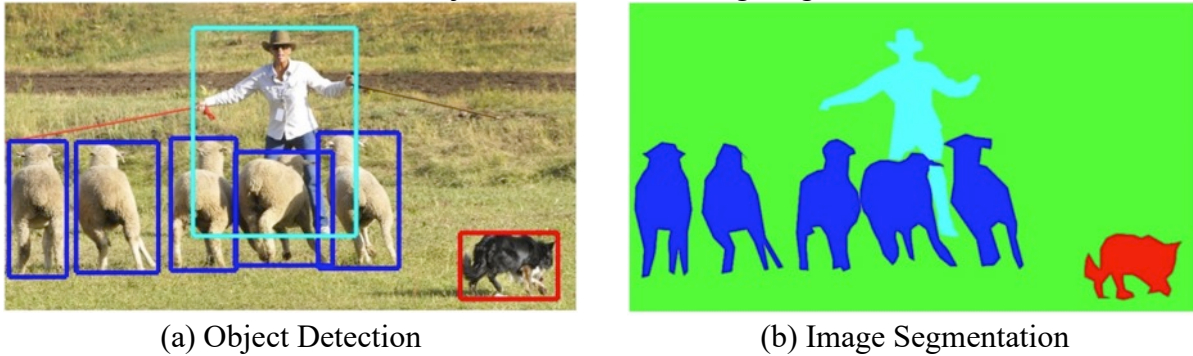
(a) Object Detection   (b) Image Segmentation
Figure A.7 Object detection vs. image segmentation (Brown, 2017).

The U-Net, one powerful image segmentation model, was firstly proposed by Ronneberger et al. in 2015 for biomedical image segmentation. It locates and classifies object or abnormality by doing classification on every pixel. Therefore, the U-Net is getting popular in image-based infrastructure defects detection and classifications, such as crack detection for pavement or tunnel (Augustaukas & Lipnickas, 2019; Lau et al., 2020; Li et al., 2020; Majidifard et al., 2020; Mongkhonthanaphon & Limpiyakorn, 2018; Matcha, 2020). Therefore, in addition to detect "Inverted-T" patching using SSD and Mask R-CNN, the U-Net was also explored for this object by the research team.

A.3.2   Image Labeling

With the collected images, the OSU team built an image library to develop the DL (DL) based "Inverted-T" patching detection model. The default collected pavement images from the 4K system are saved into 2D and 3D formats at 1-mm resolution with a size of 4,096 × 2,048 to represent approximately a 4-meter-wide and 2-meter-long pavement surface. For the images from 8K system, it covers approximately the same area (a 4-meter-wide and 2-meter-long pavement surface) but at 0.5-mm resolution with a size of 8,192 × 2,048 pixels. The presented

research uses the height information contained in 3D data to train the network to detect "Inverted-T" patching.

Due to the length limitation of each default image saved from the system, the patching is not always existed in one single image: it may be saved into two consecutive images. Therefore, the research team merged two continuous 3D images as one training image to prepare the training images and capture an entire "Inverted-T" patching in one image. With this pre-processing, each prepared image contains 4,096 pixels for 4K and 8,192 pixels for 8K in length which covers a roughly 4-meter-long pavement section. Subsequently, the prepared images from data collections in Table A.1 were manually checked and labelled for the DL training if an "Inverted-T" patching was identified in a prepared image by the research team.

(a) Raw 3D Image   (b) Labeled 3D Image
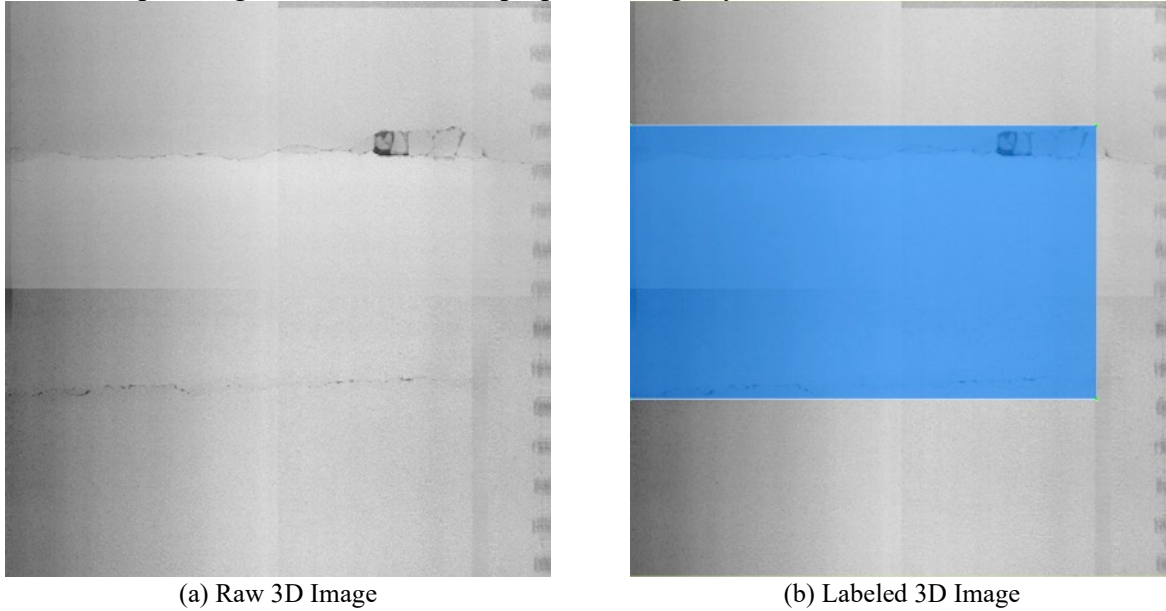
Figure A.8 Examples of image labeling for SSD300 and mask R-CNN.

Figure A.8 shows a pair of raw and labeled 3D images as an example. In Figure A.8(a), the two transverse cracks are developed across the travel lane and parallel to each other. Therefore, the research team treats this prepared 3D image as a good candidate with "Inverted-T" patching. It is labelled in Figure A.8(b) by using the LabelImg software which is a popular graphical image annotation tool in TensorFlow object detection. The blue box in Figure A.8(b) is generated from the labeling software and used as the bounding box of "Inverted-T" patching. In the following training stage, the network will teach the computer to automatically identify image area which has a similar feature like the blue box and mark it as an "Inverted-T" patching.

However, the "Inverted-T" patching was not frequently observed from the prepared images (Figure A.8), even though the data collection covered a total length of 304.3 miles with 4K system. Eventually, a total number of 501 images from 4K system were assembled to develop the SSD300 DL network while 401 and 100 images are randomly picked for training and testing. After another 142.7 miles of images were collected via the 8K system, a total number of 268 images from 4K and 8K systems were prepared to develop the Mask R-CNN DL network.

To train the U-Net for "Inverted-T" patching detection, the image was labelled using GIMP to prepare the required mask file (Figure A.9)—the "Inverted-T" patching was labelled with green colour, while the other part of the image or background was left as transparent. After training, the U-Net is expected to identify the "Inverted-T" patching and output a mask for it.

It is worth mentioning that from INDOT it was learned that the "Inverted-T" patching was constructed with a typical length less than or equal to 6 feet. Therefore, labelled images with a potential patching longer than 6 feet were removed from the prepared image library for training the Mask R-CNN and U-Net networks.

(a) Raw 3D Image   (b) Mask
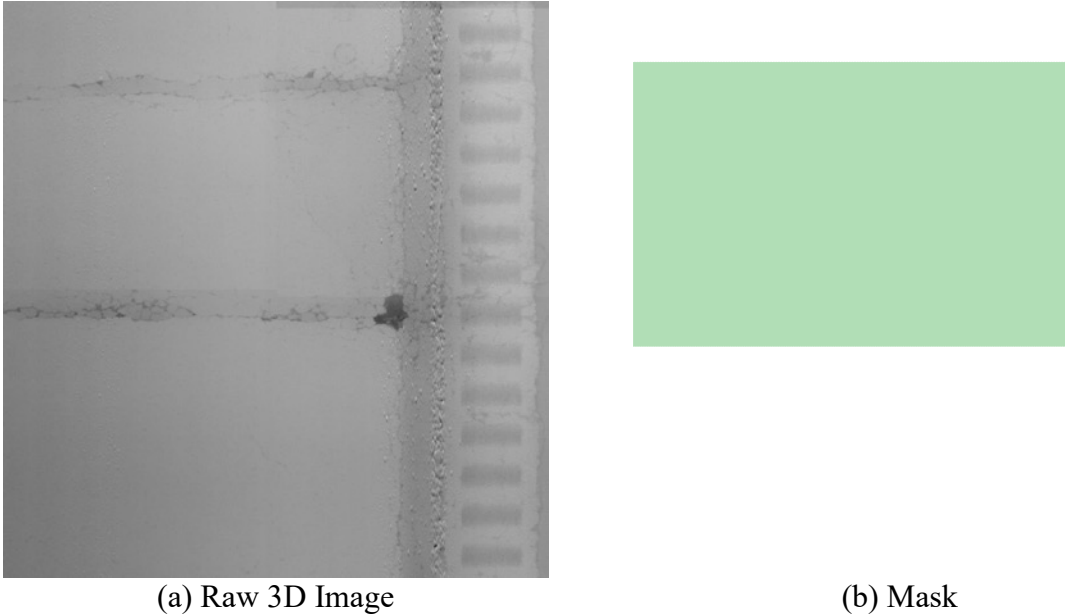
Figure A.9 Examples of image labeling for U-Net.

A.4   Deep Learning Based "Inverted-T" Patching Detection

This chapter summarizes the efforts by the research team to automatically detect "Inverted-T" patching from pavement 3D images using DL networks or models. Three popular and advanced DL models were explored to achieve this object: two object detection models (SSD300 and Mask R-CNN) and one image segmentation model (U-Net). The architecture, training, and performance of each network are summarized as follows.

A.4.1   SSD300

A.4.1.1 Network Architecture

The Single Shot MultiBox Detector (SSD) is applied to detect the potential areas containing an "Inverted-T" patching. The basic structure of SSD (Figure A.10) consists of three critical features (Girshick et al., 2014).

1. Multi-Scale Feature Extractors

The SSD network is set upon pre-trained base network (e.g., VGG 300) with built-in and extra convolutional and pooling layers. Those layers decrease the input image size progressively and generate feature maps in multiple scales to provide both local and global information for object predictions. In other words, the shallow layers with bigger maps are used to predict small objects, while the deep layers with smaller maps are utilized to detect big objects.

2. Convolutional Predictors

SSD network utilizes a set of convolutional filters to infer prediction results from different feature layers. For example, a set of filters in shape of $3\times3\times P$ can be used in a layer with feature maps in shape of $w\times h\times P$ to generate the score for a category or the shape offset relative to the default box coordinates.

3. Default Boxes and Aspect Ratios

Similar to the anchor boxes used in Faster R-CNN (Ren et al., 2016), a series of default boxes are adopted in SSD network to ease the difficulty of training process. As Figure A.11 shows, each cell in different feature map (Figure A.11(b) and Figure A.11(c)) has four anchor boxes in different sizes. Each box can predict the score for all object categories and the shape offsets. During the training process, the default boxes are matched to the ground truth boxes (e.g., the two boxes in blue dashed lines are utilized as positives to learn the object "cat"; the box in red dashed lines is applied as positive to learn the object "dog"; and others are treated as negatives).
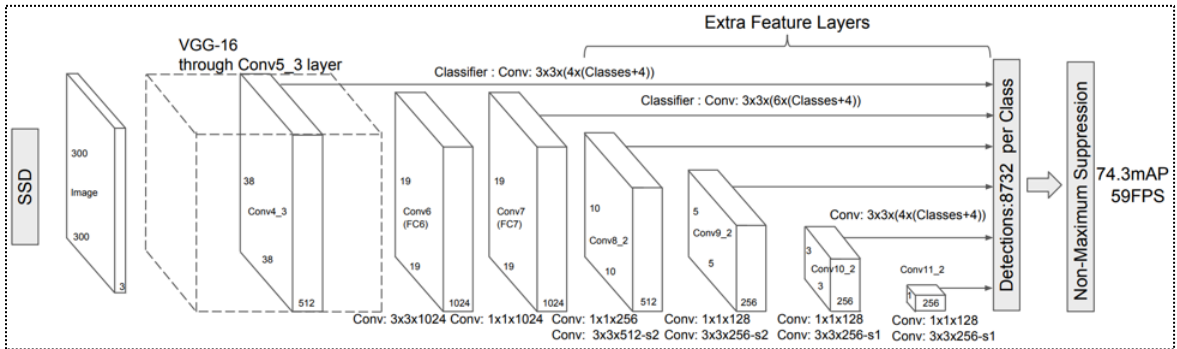
Figure A.10 SSD300 structure for object detection (Girshick et al., 2014).

| (a) Images with GT boxes | (b) 8 x 8 feature map | (c) 4 x 4 feature map |

$$\text{loc} : \Delta(cx, cy, w, h)$$
$$\text{conf} : (c_1, c_2, \cdots, c_p)$$
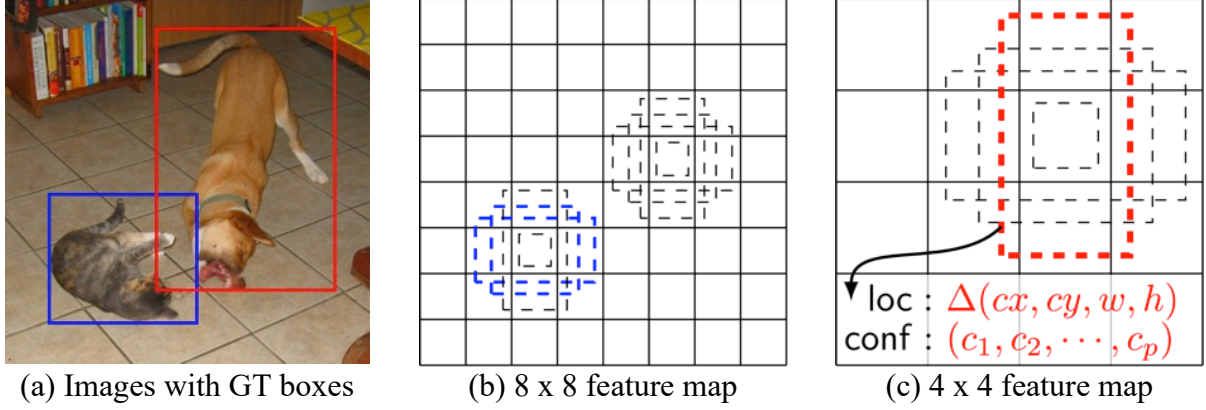
Figure A.11 Default boxes in SSD network.

A.4.1.2 Network Training and Performance

A total of 501 4K images with "Inverted-T" features were manually annotated for network training and testing using the TensorFlow (401 images for training and 100 images for testing). The initial learning rate is set to 0.001, the mini-batch size is set to 8, and the maximum iteration steps are set to 10,000. The loss change during training process is illustrated in Figure A.12. As training goes on, both the classification loss and the localization loss are gradually reduced, resulting in the decrease in the total loss (the weighted sum of classification and localization loss). The weights at the 9,470th iteration are picked for the subsequent evaluation on the network performance.
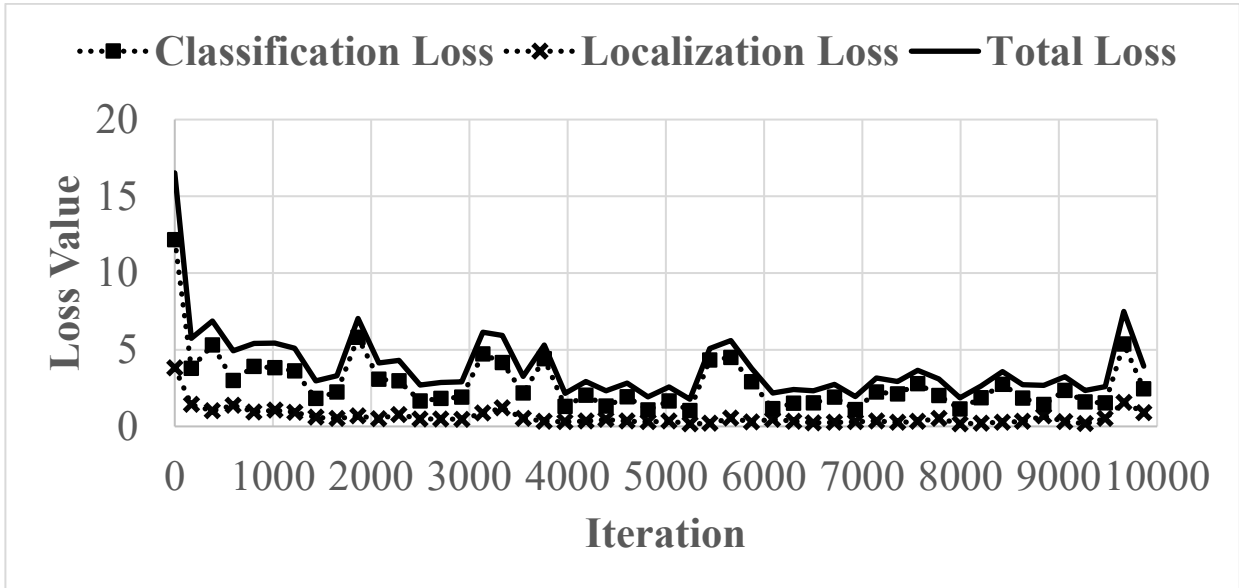
Figure A.12 Loss change during training process for SSD300.

The Precision (***Pr***), Recall (***Re***), and F1-Score (***F1***) are adopted as the evaluation indicators. The precision and recall can be computed on true positive (***TP***), false negative (***FN***) and false positive (***FP***) as the following equations:

$$Pr = TP/(TP + FP) \qquad \text{Eq. 1}$$

$$Re = TP/(TP + FN) \qquad \text{Eq. 2}$$

$$F1 = 2 \times P \times R/(P + R) \qquad \text{Eq. 3}$$

Where,
TP is an "Inverted-T" recognized correctly on an image cell (IoU > 0.5).
FP is a "Non-Inverted-T" recognized incorrectly on an image cell (IoU < 0.5).
FN is an "Inverted-T" recognized incorrectly on an image cell.

The performance of SSD network for "Inverted-T" patching detection is summarized in the Table A.2. According to Table A.2, the performance on the testing datasets (F1: 74.29%) is a little bit higher than that on the training datasets (F1: 70.56%), which may be caused by inadequate "Inverted-T" samples for both training and testing datasets. Based on Figure A.5, most "Inverted-T" distresses can be recognized accurately. Figure A.13 provides some good examples of Inverted-T detection. However, the SSD network sometimes over-estimate the "Inverted-T" as Figure A.14 shows, because the features of "Inverted-T" are hard to be perceived even by our human eyes. In addition, current datasets with "Inverted-T" patching are still not enough yet. The performance of the SSD network should be improved further once more training samples are involved in the future.

Table A.2 Statistics on Inverted-T Detection Results for SSD300

	Precision (%)	Recall (%)	F1-Score (%)
Training Datasets	67.58	73.82	70.56
Testing Datasets	70.91	78.00	74.29
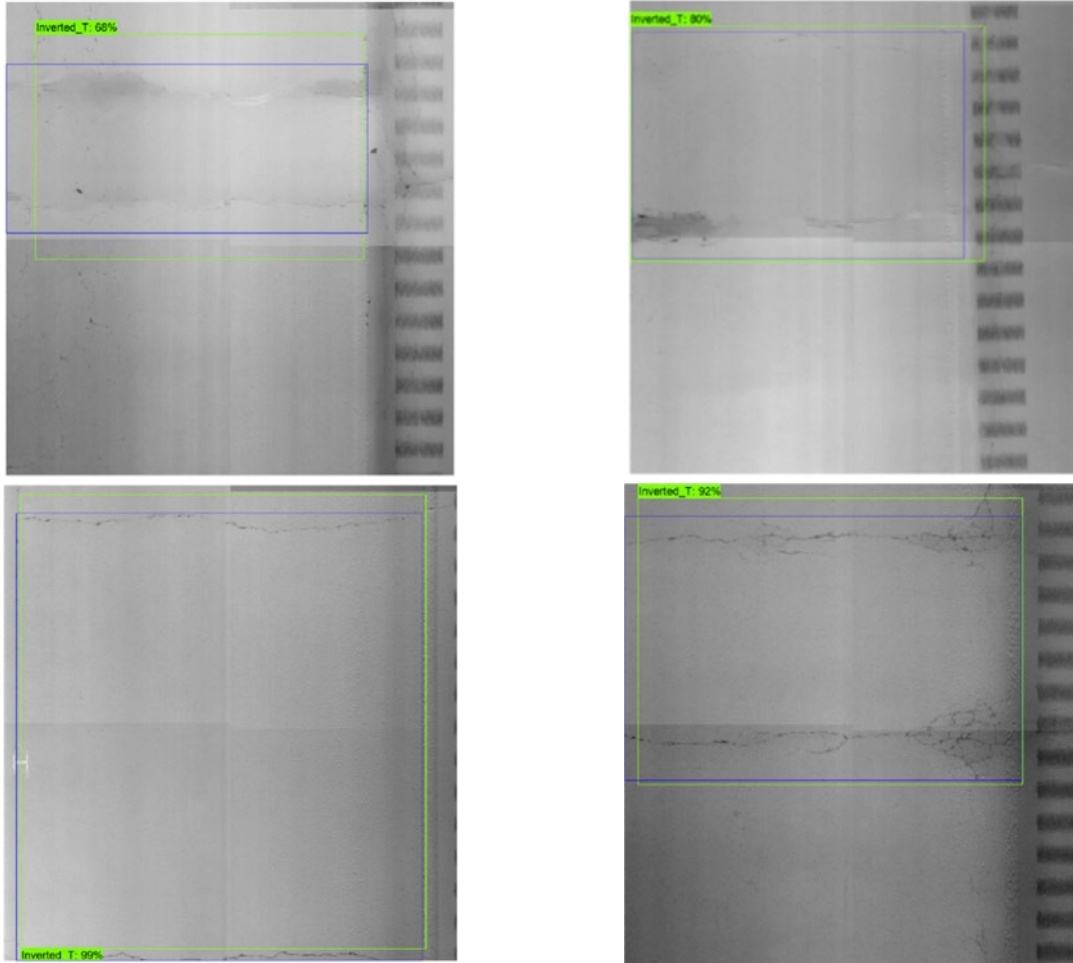
Figure A.13 Good examples of Inverted-T detection using SSD network (green: prediction box; blue: ground-truth box).
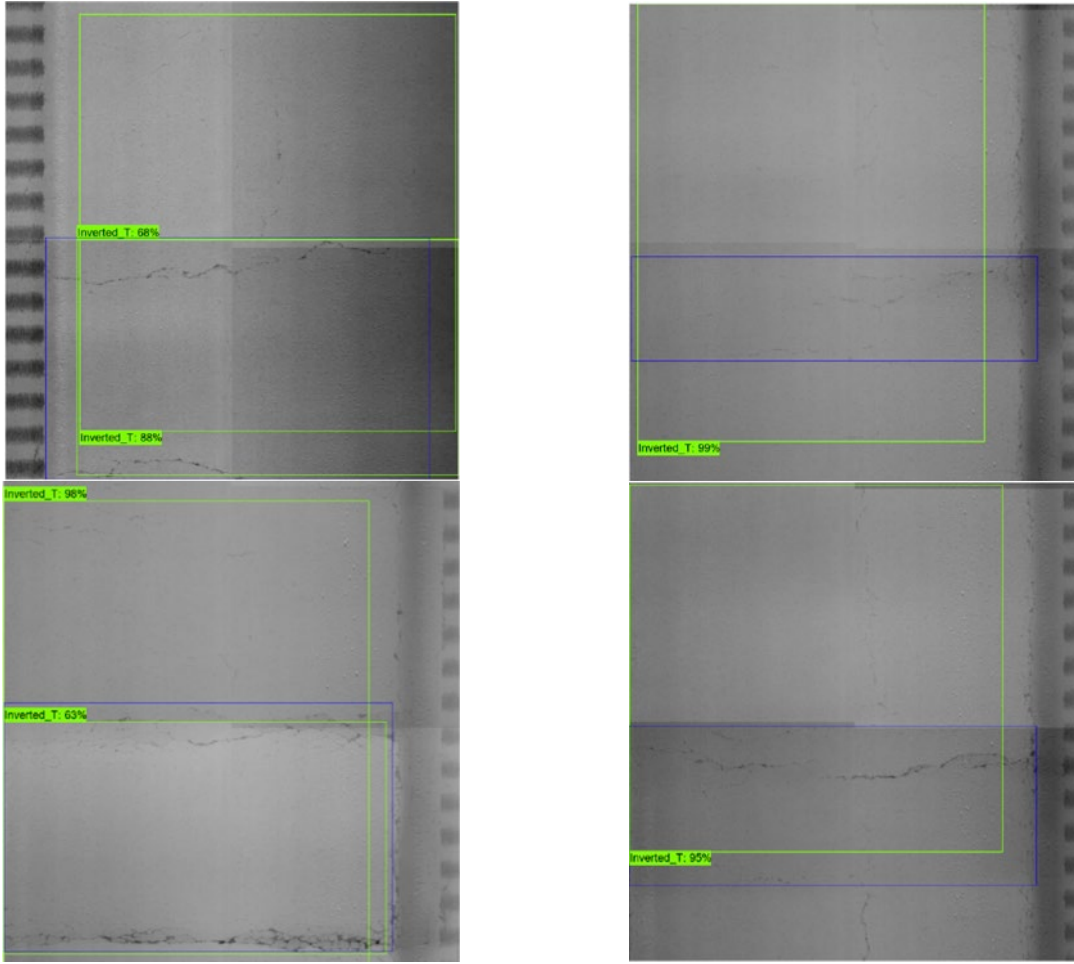
Figure A.14 Bad examples of Inverted-T detection using SSD network (green: prediction box; blue: ground-truth box).

A.4.2   Mask R-CNN

A.4.2.1 Training without Image Augmentation

Network Architecture

The architecture of Mask R-CNN is illustrated in Figure A.15. It includes backbone network and Network Head: (1) The backbone network is a standard Convolutional Neural Network (CNN) for feature extraction from the images. The Mask R-CNN in this study is based on Feature Pyramid Network (FPN) and a ResNet 101 network as backbone. (2) The network head performs three parallel tasks for object detection: bounding box regression, classification, and mask prediction.
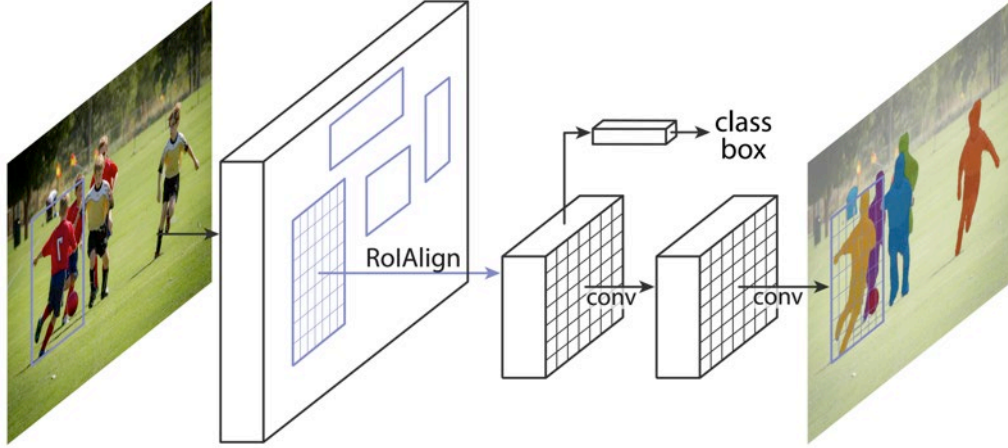
Figure A.15 Mask R-CNN framework (Sachan, 2017).

The feature map from FPN and backbone network includes many candidate frames, or RoI. Many of these RoI are filtered out by Non-Maximum Suppression (NMS) to reduce redundancy. The Intersection over Union (IoU) is a ratio of the area of overlap and the area of union for the predicted bounding box and the labeled bounding box of a RoI: the closer the two boxes, the higher the IoU score. The IoU is used to determine whether a bounding box prediction for RoI is good or not. The IoU threshold for NMS was set to 0.8 in this study during the training of Mask R-CNN. It means RoIs with IoU more than 0.8 will be left as the candidates of corrected prediction of "Inverted-T" patching. Then, the feature map and the remaining RoI are further processed in the RoIAlign layer to predict pixel masks accurately by avoiding quantization. Lastly, the analysis is finished in the network head including two branches: one for object classification and frame regression; the other for pixel segmentation.

Network Training and Performance

A total of 268 4K and 8K images were used to train Mask R-CNN to automatically detect "Inverted-T" patching less than 6 feet long from the 3D images using TensorFlow (80% images for training and 20% images for testing). The initial learning rate is set to 0.001, the mini-batch size is set to 2, and the maximum epochs are set to 400. All of the implementations have been done with Tensorflow and Keras on a single GPU Nvidia GTX 1070 (8 gb). Training time is about 5 hours from scratch. The loss change during training process is illustrated in Figure A.16. As training goes on, both the training loss and the validation loss are gradually reduced. The weights at the 394th epoch are picked for the subsequent evaluation on the network performance.

(a) Training Loss   (b) Validation Loss
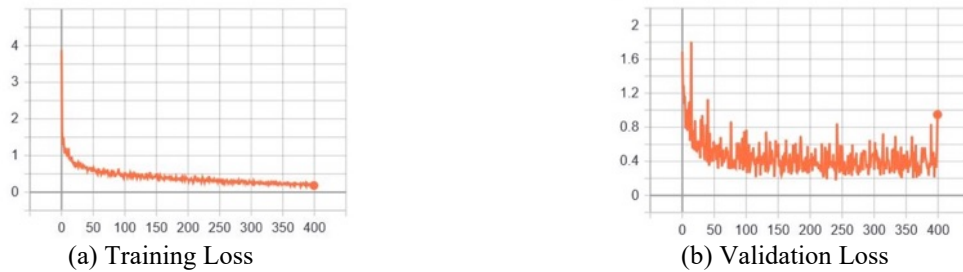
Figure A.16 Loss change during training process for mask R-CNN.

The mean average precision (mAP), mean average recall (mAR), and F1-Score on training and testing data are summarized in Table A.3. By comparing the results in Table A.2 and Table A.3, the Mask R-CNN shows better performance than the SSD300 on the prepared image library. Figure A.17 and Figure A.18 shows examples of good and bad predictions from Mask R-CNN on the testing data. The trained Mask R-CNN model still misclassify or missed the "Inverted-T" patching from the 3D images in some cases, as shown in Figure A.18.

Table A.2 Summary of Training Results for Mask R-CNN

	mAP (%)	mAR (%)	F1-Score (%)
Training Datasets	96.51	96.74	96.63
Testing Datasets	94.44	94.44	94.44
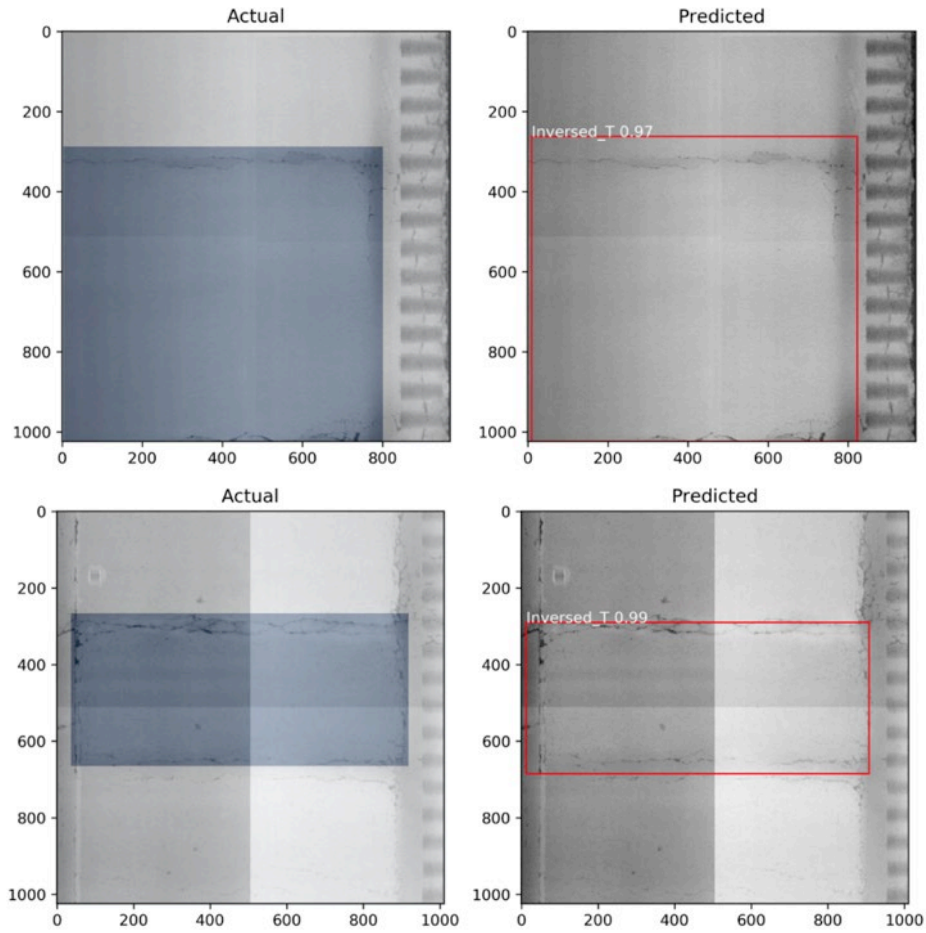
Figure A.17 Good examples of Inverted-t detection using mask R-CNN.
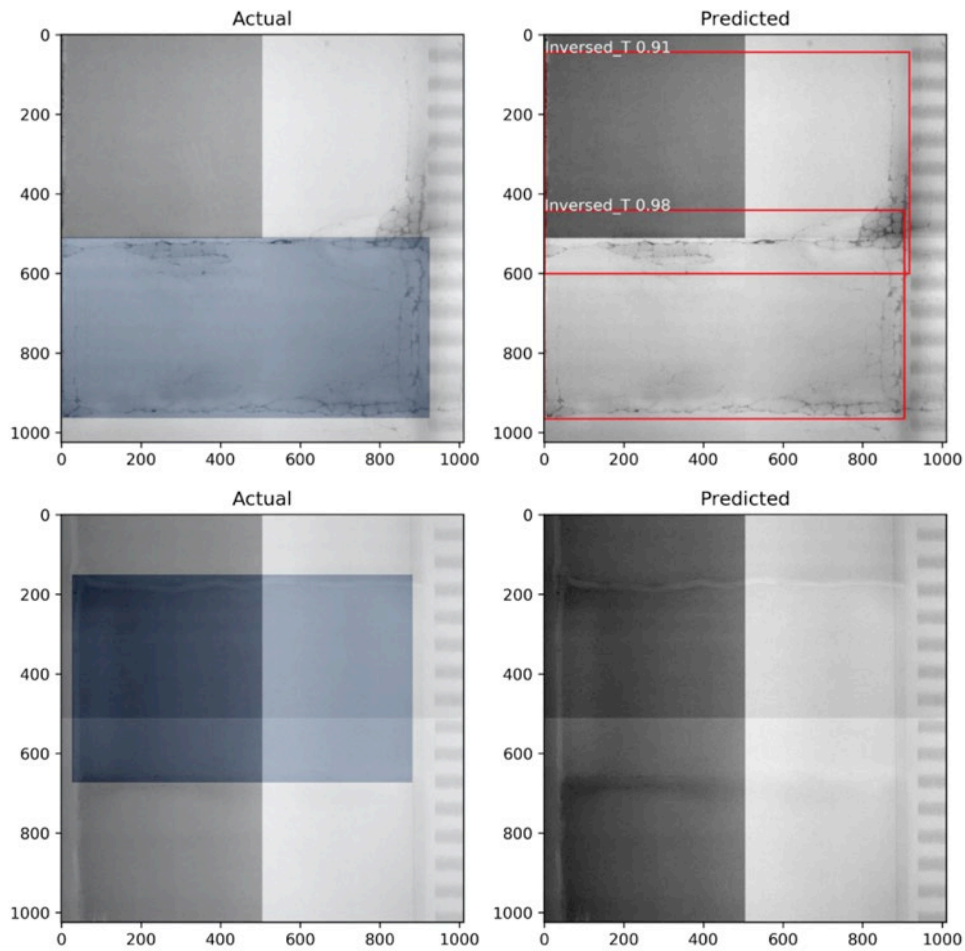
Figure A.18 Bad examples of Inverted-t detection using mask R-CNN.

Subsequently, the obtained Mask R-CNN model was used to detect "Inverted-T" patching from the 8K 3D images in the 37th data collection in Table 2.2 "I65_NBDL-20200304.150707" to verify: (1) if the model can be used to identify the "Inverted-T" patching from a real data collection; (2) the level of its accuracy in "Inverted-T" patching detection. Unfortunately, many false positive happened from the Mask R-CNN prediction, as displayed in Figure A.19. In other words, the Mask R-CNN predicted an "Inverted-T" patching from images that were collected on pavement with good condition but no possible "Inverted-T" patching existed. As a matter of fact, the existence of "Inverted-T" patching is relatively small compared with the size of a highway network. Therefore, it is not acceptable for the Mask R-CNN model to make these false predictions on pavement sections without the "Inverted-T" patching: per this false information, it will increase rather than narrow the patch search area for engineers.
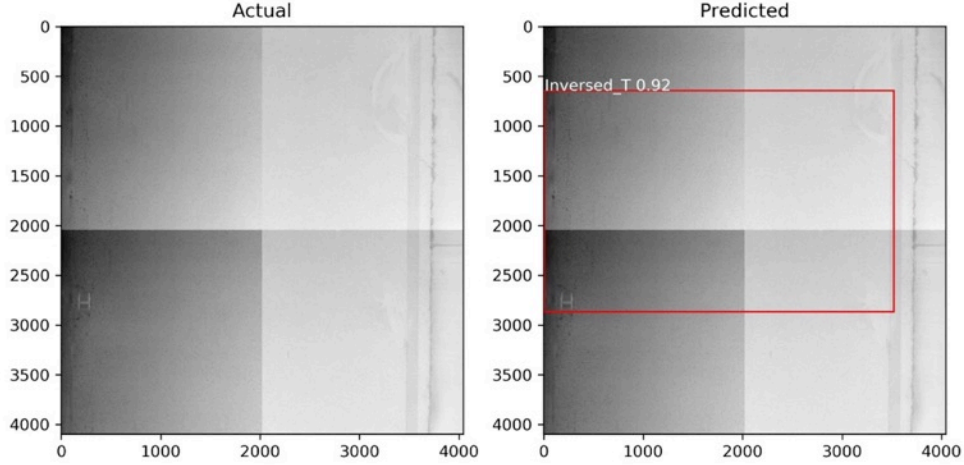
Figure A.19 False positive prediction using mask R-CNN.

A.4.2.2 Training with Image Augmentation

It is well known that DL networks need large amount of training data to achieve good performance. The small number of training images (268) was considered as one possible reason for causing the many false positive predictions from Mask R-CNN (Figure A.19). To increase the network's accuracy and robustness, image augmentation was used to increase the number of images for training and testing Mask R-CNN.

Image augmentation artificially creates training images through different ways of processing or combination of multiple processing, such as random rotation, shifts, shear and flips, etc. The image augmentation includes different combinations of horizontal flipping, transverse flipping, adding salt/pepper noise, adjusting image brightness, and image blurring. Figure A.20 displays the original image and the augmented images as an example. With these image augmentations, the number of training images increased from 268 to 1,608.

With the increased image dataset, the Mask R-CNN was trained again with 80% images for training and 20% images for testing. The loss change during training process is illustrated in Figure A.21. The weights at the 400th epoch are picked for the subsequent evaluation on the network performance.

The mAP, mAR, and F1-Score on training and testing data are summarized in Table A.4. By comparing the results in Table A.3 and Table A.4, the Mask R-CNN with image augmentation (1,608 images) shows slightly better performance than that without image augmentation (268 images). It means the image augmentation is helpful to improve the model's performance. However, when applying the newly obtained Mask R-CNN to detect "Inverted-T" patching from the 8K 3D images in the 37th data collection, many false positive happened again, as displayed in Figure A.19. It means the trained Mask R-CNN with image augmentation is still not good enough to narrow the patch search area for engineers.
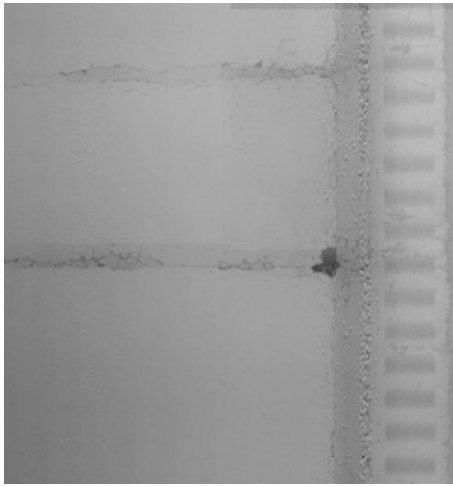
(a) Original
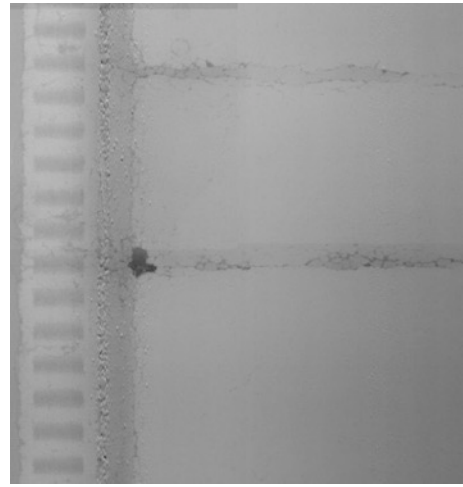
(b) Horizontal Flipped
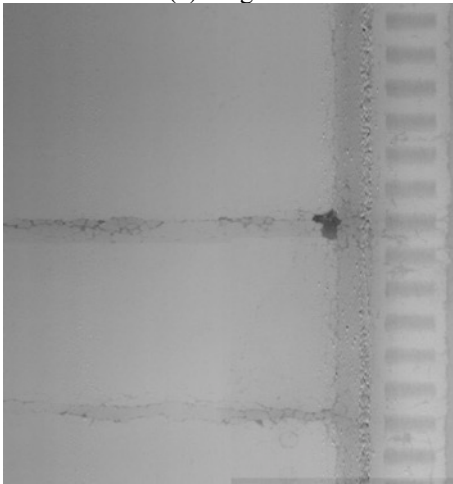
(c) Vertical Flipped
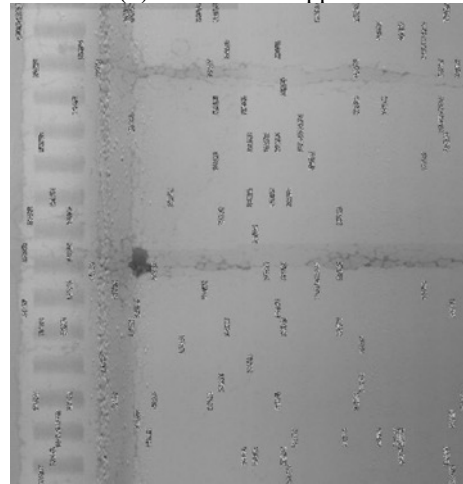
(d) Horizontal Flipped & Salt/Pepper Noise
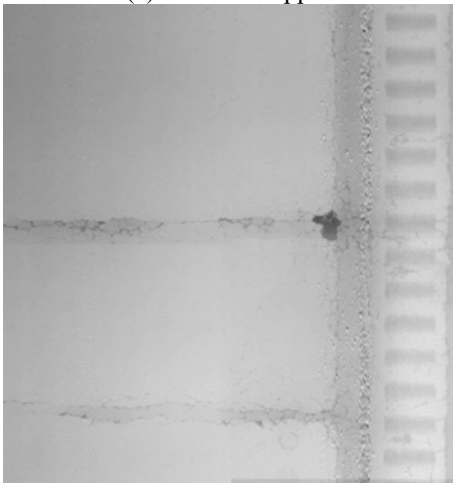
(e) Vertical Flipped & Changed Brightness
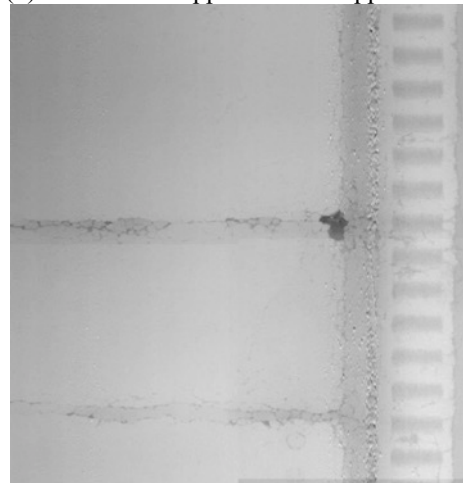
(f) Horizontal Flipped & Image Blurring

Figure A.20 Examples of image augmentation for mask R-CNN training.

| (a) Training Loss | Validation Loss |
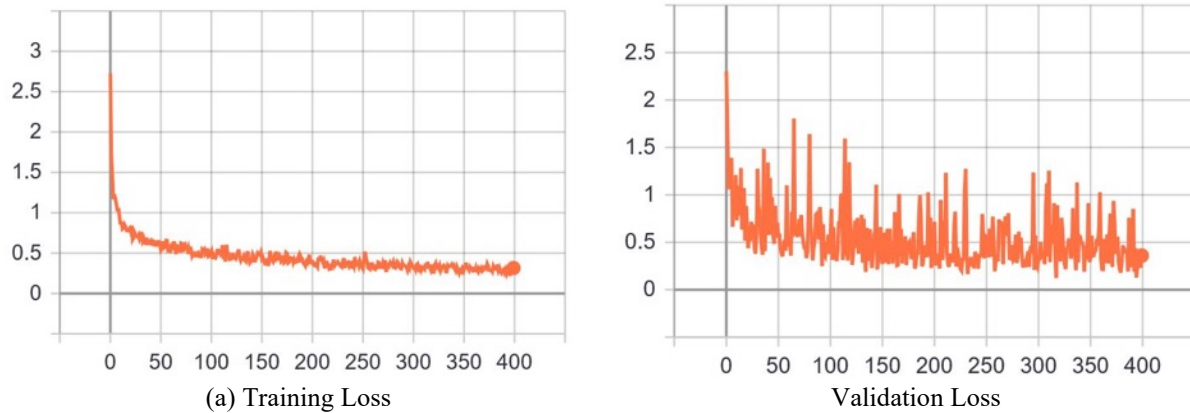
Figure A.21 Loss change during training process for mask R-CNN with image augmentation.

Table A.3 Summary of Training Results for Mask R-CNN with Image Augmentation

	mAP (%)	mAR (%)	F1-Score (%)
Training Datasets	96.47	98.99	97.72
Testing Datasets	97.01	97.17	97.09

At this moment, the OSU team is conducting Mask R-CNN training by adding normal pavement images into the training dataset as "Background" only. These normal pavement images were collected from pavement sections without "Inverted-T" patching (Figure A.22). With this consideration, hopefully the Mask R-CNN can learn the feature of normal pavement images and make less false positive predictions on them to improve its accuracy in the future. In other words, to train the Mask R-CNN to only find the "Inverted-T" patching from the 3D images, it is necessary to train the model so it recognizes other images that do not have the "Inverted-T" patching and will not make false predictions. The final report will include this update in the following weeks if the results are positive.
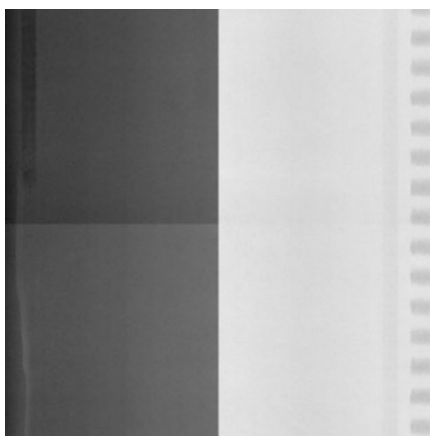
(a) AC
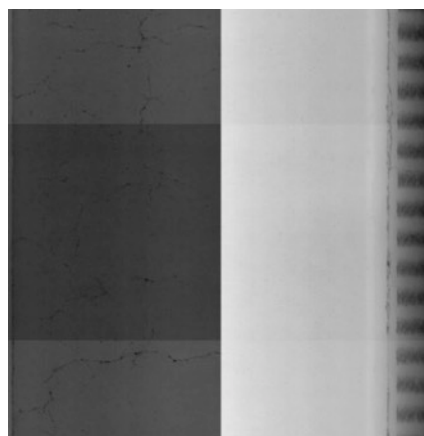
(b) AC with Crack
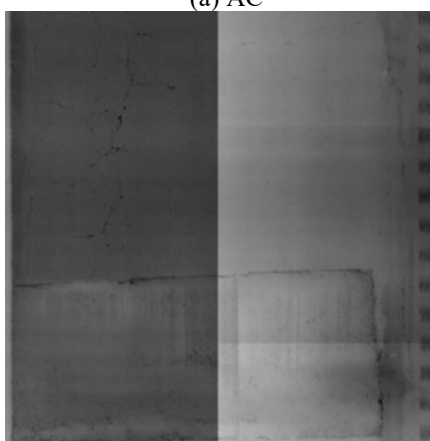
(c) AC with Patching
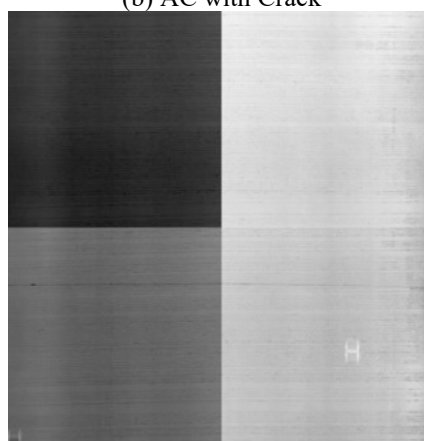
(d) PCC
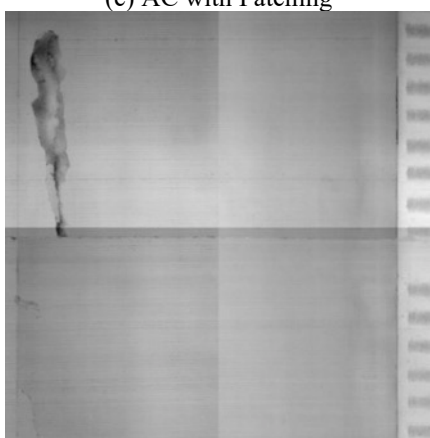
(e) PCC with Crack
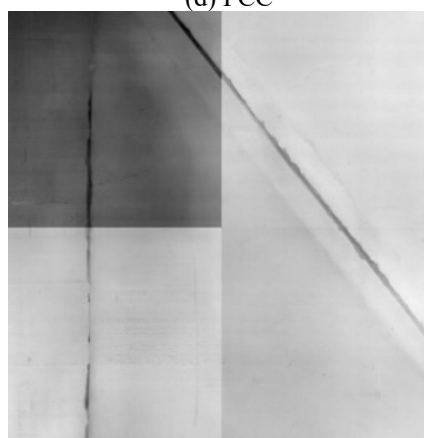
(f) Bridge Joint

Figure A.22 Examples of normal pavement images.

A.4.3   U-Net

A.4.3.1 Network Architecture

The architecture of U-Net (Figure A.23) consists of a contracting path to capture context (the left part) and a symmetric expanding path that enables precise localization (the right part), which gives it the u-shaped architecture. The contracting path is a typical convolutional network that consists of repeated application of convolutions, each followed by a rectified linear unit (ReLU) and a max pooling operation. During the contraction, the spatial information is reduced while feature information is increased. The expanding path combines the feature and spatial information through a sequence of up-convolutions and concatenations with high-resolution features from the contracting path. In this study, the VGG-16 and ResNet-50 were used as the encoder or contracting path of the U-Net (the left part) for improving the model's performance and stability.
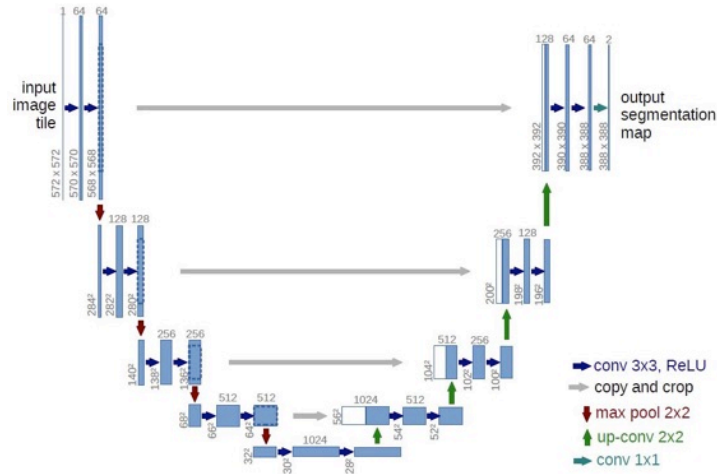
Figure A.23 Example of U-Net architecture (Ronneberger et al., 2015).

A.4.3.2 Network Training and Performance

Because the Mask R-CNN had many false positive predictions, the training of U-Net focus on identifying the distinct "Inverted-T" patching only. Therefore, before training the U-Net, the research team deleted some images that were not 100% sure to be an "Inverted-T" patching from the previously prepared dataset that was used to train Mask R-CNN. For each 3D image in the prepared dataset, the corresponding 2D and ROW images from the original data collection was double-checked to make sure (1) the 3D image contains two parallel transverse cracks, and (2) the distance between the transverse cracks is less than 6 feet Some examples of 3D images with unconfident "Inverted-T" patching are listed in Figure A.24: (a) the image has two sealed transverse cracks; (b) the image has one distinct transverse crack while the other

transverse crack is fuzzy and small; (c) the image has two unparalleled transverse cracks; and (d) the image has two fuzzy and small transverse cracks.

(a) Sealed Crack
(b) One Transverse Crack

(c) Unparalleled Transverse Cracks
(d) Subtle Transverse Cracks
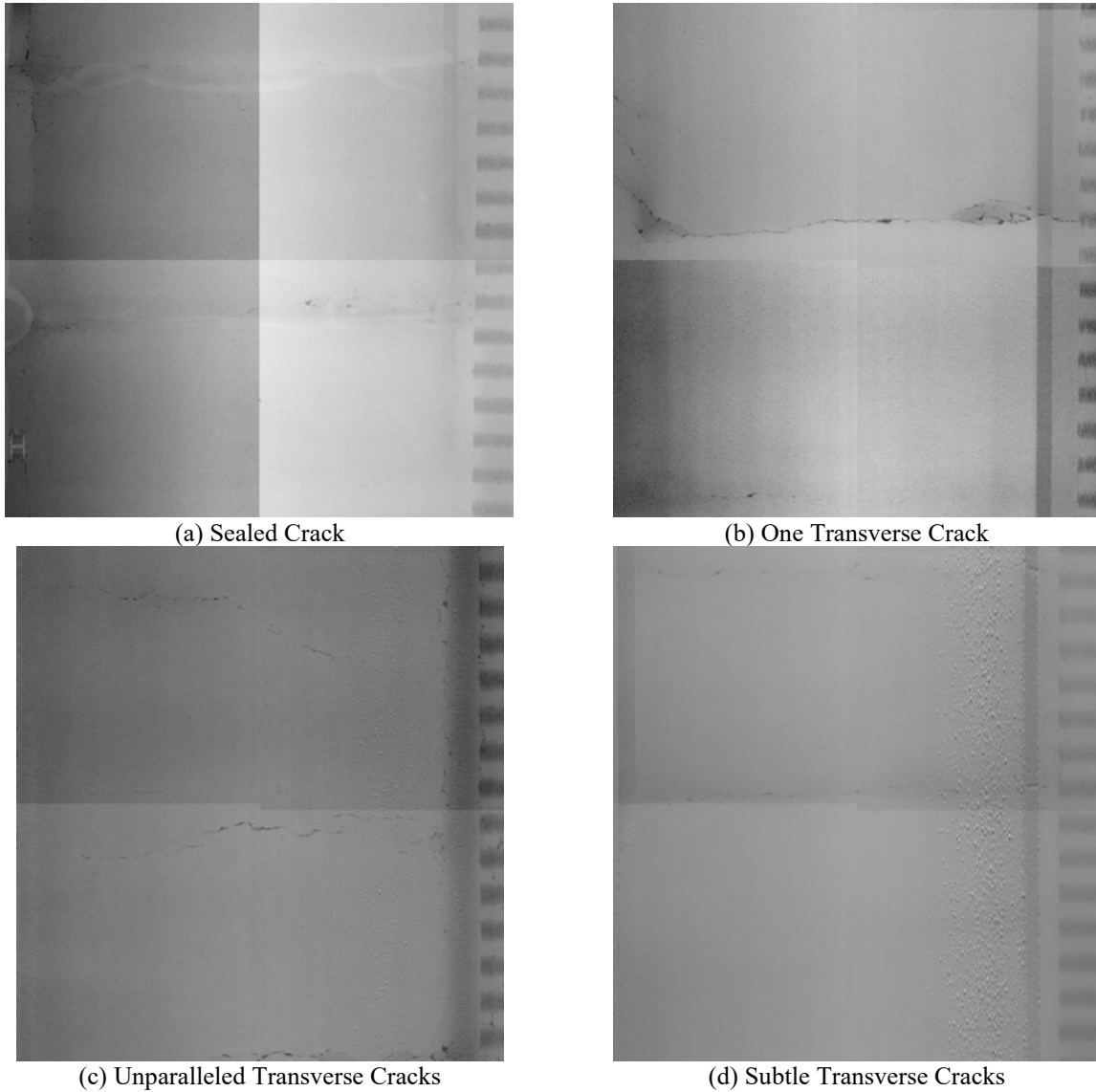
Figure A.24 Example of 3D images with unconfident "Inverted-T" patching.

After adjusting the prepared training dataset, 66 pavement 3D images containing distinct "Inverted-T" patching were left for U-Net training. Then, each 3D image and its mask were augmented 10 times with different combinations of augmentation techniques to increase the number of training images. Figure A.25 lists 10 augmented images and masks of a 3D image as an example. Therefore, a total of 726 images were available for U-Net training (80% for training and 20% for testing). All of the implementations have been done with Tensorflow and Keras on a single GPU Nvidia GTX 1070 (8gb). The network was trained with 60 epochs with training time about 7 hours from scratch.

The evaluation of the performance of U-Net segmentation includes three widely used metrics: (1) class IoU, (2) mean IoU, and (3) frequency weighted of IoU. The IoU is defined as the ratio of intersection of ground truth and predicted segmentation outputs over their union. The class IoU is calculated for each class separately (background and "Inverted-T" patching here). Then, the class IoU is averaged over all classes to provide a global, mean IoU of U-Net segmentation prediction. If one class dominates most part of the images in a dataset, it needs to be weighed down compared to other classes. Thus, instead of taking the mean of all the class results, the frequency weighted IoU is taken based on the frequency of the class region in the dataset (Lau et al., 2020; Li et al., 2020).

The summary of model performance is detailed in Table A.5 reporting all the measures. Figure 4.5 shows some prediction examples on the testing dataset for "Inverted-T" patching from VGG16_U-Net and ResNet50_U-Net. The ResNet50_U-Net exhibited slightly better performance than VGG16_U-Net. However, both models made certain wrong predictions: they classified some pixels of background (or other pavement section) as the "Inverted-T" patching (Figure A.26). It means the models are not learning the features of "Inverted-T" patching very well because of two potential reasons: (1) the small training dataset (726) and (2) the "Inverted-T" patching is so close to the background and the network cannot really tell the difference.

Table A.1 Summary of Training Results for U-Net with Image Augmentation

Models	Class IoU		Mean IoU	Frequency Weighted IoU
	Class 1	Class 2		
VGG16_U-Net	0.6062	0.5208	0.5635	0.5655
ResNet50_U-Net	0.6149	0.6137	0.6143	0.6143

When testing the obtained U-Net via the 8K pavement 3D images in the 37th data collection, many false positive occurred again, as displayed in Figure A.27. It means the trained U-Net was still not good enough to accurately detect the "Inverted-T" patching to narrow the patch search area for engineers.
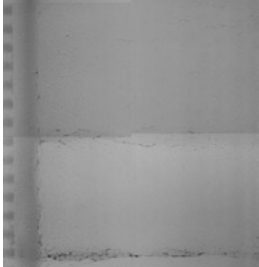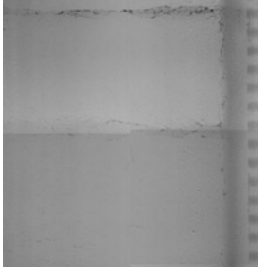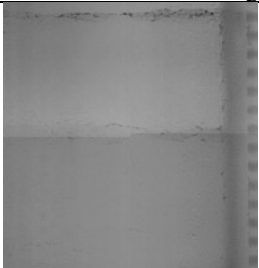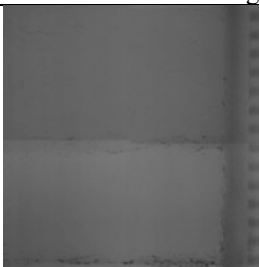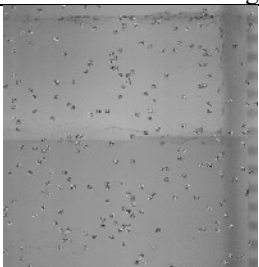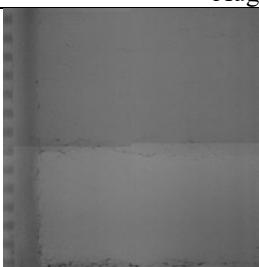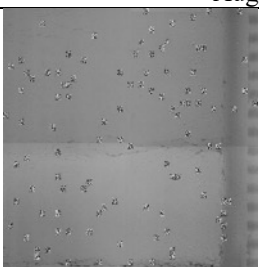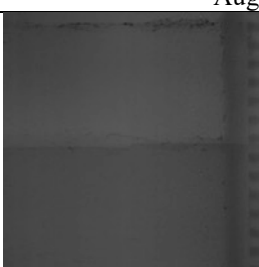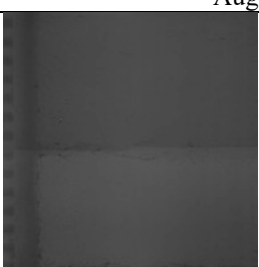
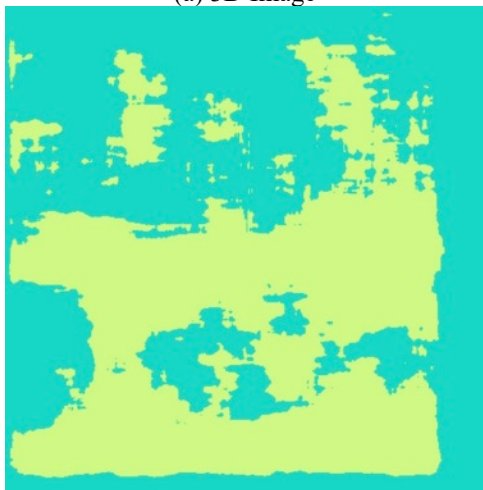| Augmented Images	Augmented Masks	Augmented Images	Augmented Masks
Augment-1		Augment-2	
Augment-3		Augment-4	
Augment-5		Augment-6	
Augment-7		Augment-8	
Augment-9		Augment-10	

Figure A.25 Examples of image augmentation for U-Net training.
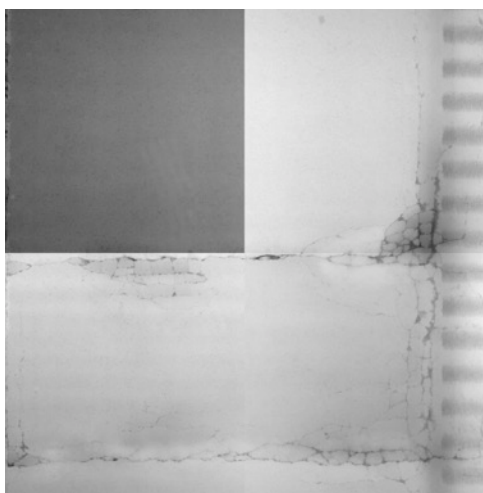
(a) 3D Image

(b) Mask – Ground Truth

(c) Mask – VGG16_U-Net

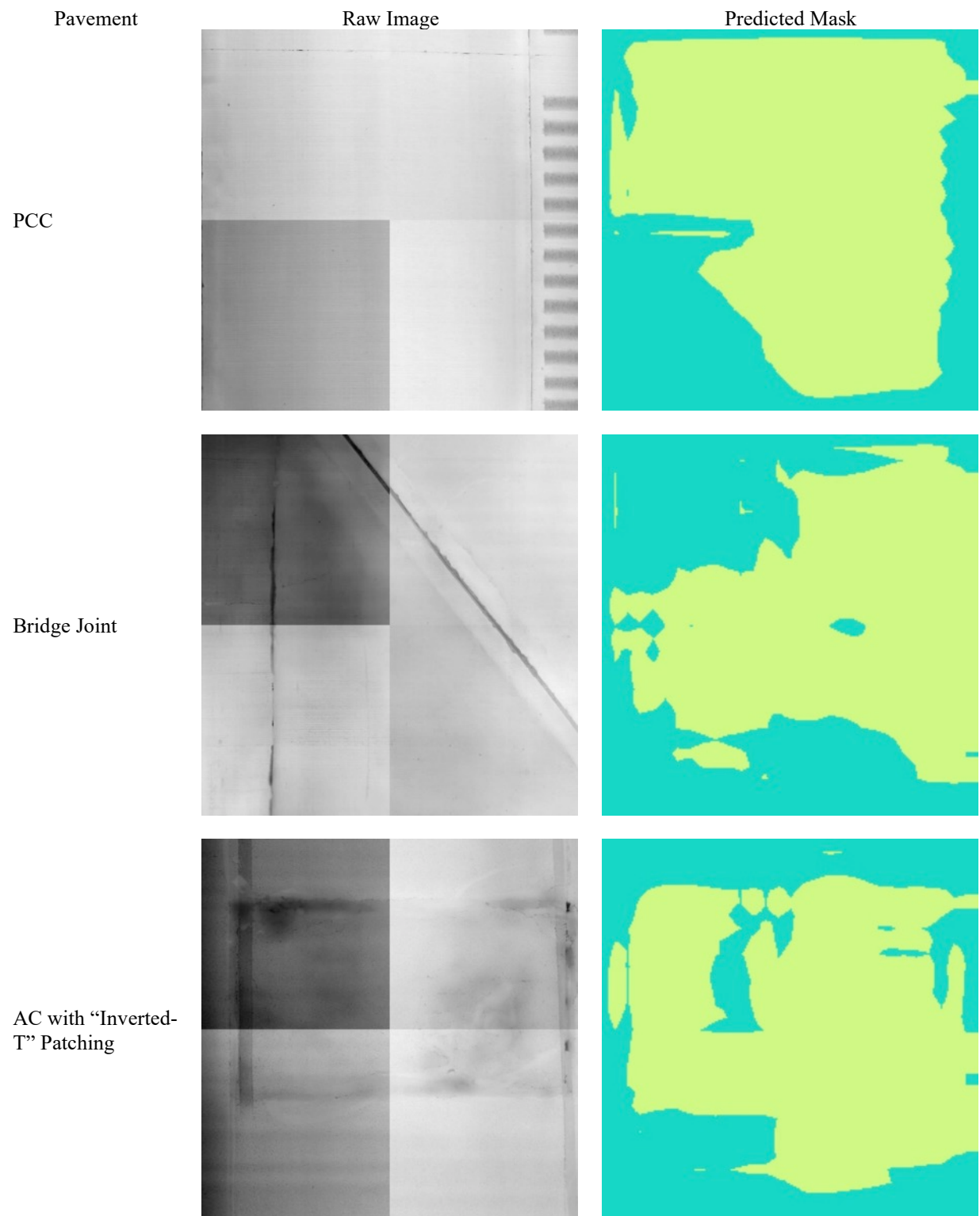(d) Mask – ResNet50_U-Net

Figure A.26 Examples of U-Net prediction.

Pavement	Raw Image	Predicted Mask
PCC		
Bridge Joint		
AC with "Inverted-T" Patching		

Figure A.27 False positive prediction using U-Net.

After exploring these different training methods, some challenges in detecting "Inverted-T" patching from pavement 3D images using DL are summarized as follows:

(1) The number of training images are limited because (a) the "Inverted-T" patching may expand across two consecutive images (Figure A.28): so this "Inverted-T" patching may be missed when preparing the training datasets by checking each 3D image; (b) some images with potential "Inverted-T" patching contains one transverse crack rather than two transverse cracks, and (c) sometimes, it is challenging for a human to determine if a 3D image includes "Inverted-T" patching: the research team needs to double check the corresponding 2D and ROW images to make decisions.
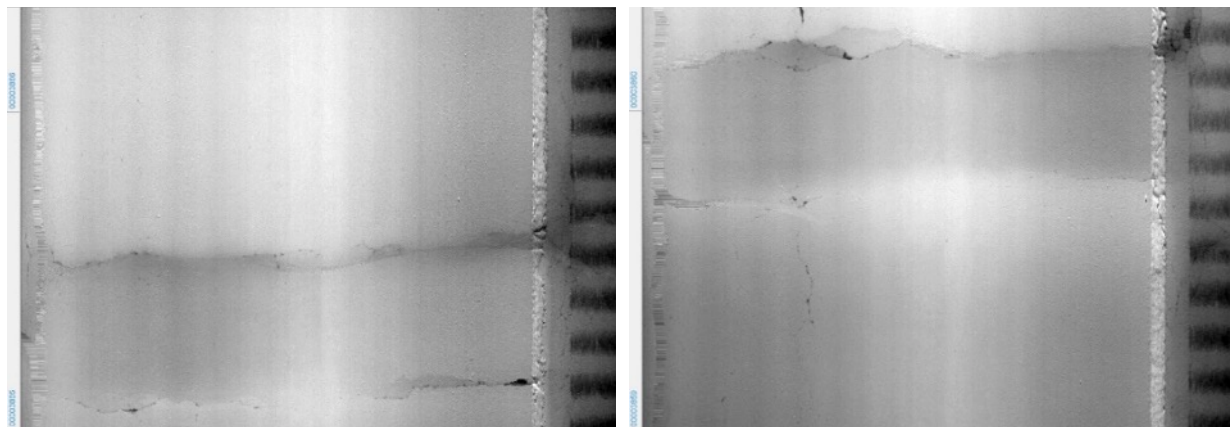
(a) "Inverted-T" Patching in Image 3865   (b) "Inverted-T" Patching in Image 3859-3860

Figure A.28 Example "Inverted-T" patching in one and two images.

(2) The "Inverted-T" patching is so similar to the background that the DL model cannot distinguish them. For example, in Figure A.29(a), the 3D image contains two parallel transverse cracks and is labeled as an "Inverted-T" patching candidate for the network to learn. However, for the pixels between the transverse cracks and within the "Inverted-T" patching, it is similar to other pixels belonging to the background or other normal pavement sections. This is different from a typical image segmentation task. For example, people want to detect vehicles from images for autonomous driving using DL (Figure A.29(b)). The pixels within the vehicle object is most likely different from other objects, such as road or sky. Therefore, the similarity between "Inverted-T" patching and background in the obtained 3D images could bring challenges for DL networks to get accurate predictions.

| (a) Detect "Inverted-T" Patching | (b) Detect Vehicles |
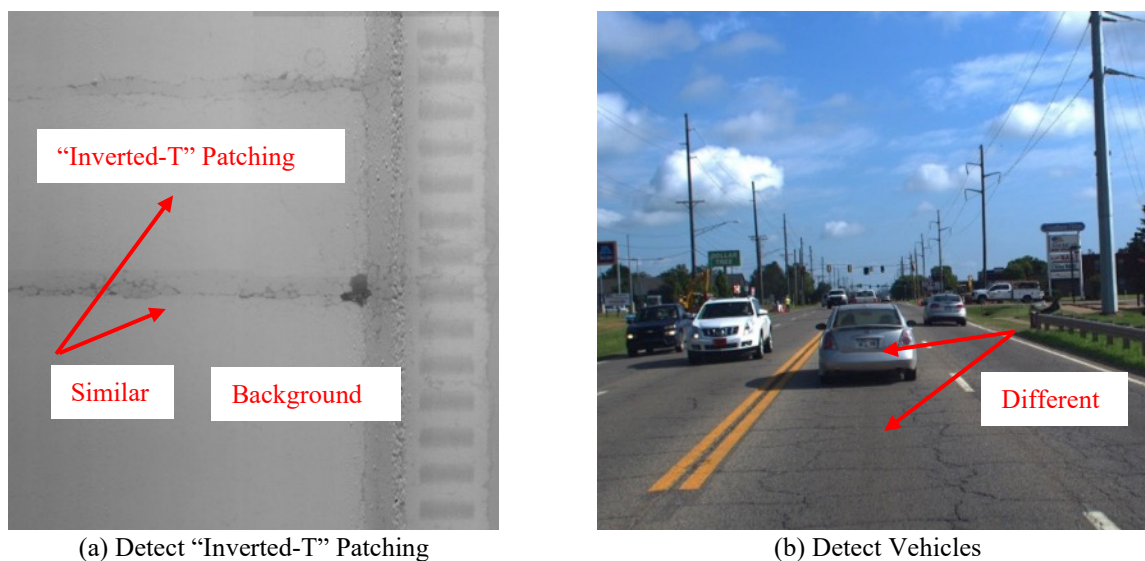
Figure A.29 Similarity of "Inverted-T" patching and background.

## A.5   IRI Based "Inverted-T" Patching Detection

The "Inverted-T" patches are not connected with the existing concrete pavement with dowel bars, so they could be unstable sections having more settlement than existing concrete pavement under traffic loading. This uneven settlement leads to failures including dip and reflective transverse cracking in the asphalt overlay around the "Inverted-T" patches. Due to challenges the OSU research team faced in developing effective DL based "Inverted-T" patching detections, the team subsequently explored "Inverted-T" patching detection based on International Roughness Index (IRI), a widely used indicator for pavement roughness or ride quality.

A.5.1   IRI and Pavement Distresses

The pavement roughness profile was obtained for data collections in Table A.1 via the WayLink 3D laser imaging system. As the laser imaging system moves on an "Inverted-T" patching with uneven settlement that causes dip or reflective transverse cracks, the vehicle is anticipated to experience more vibrations than pavement sections without this distress. Therefore, an "Inverted-T" patching causing dip or reflective transverse cracks could cause a larger IRI value: a higher IRI value indicates a rougher road surface or lower ride quality.

Therefore, the IRI results and corresponding 2D/3D pavement images were checked together to investigate the relationship between pavement condition and IRI numbers. The IRI was calculated with 12 feet as the interval for data collections on I-65 and I-74 via 4K and 8K laser imaging systems. Some conclusions are found as follows:
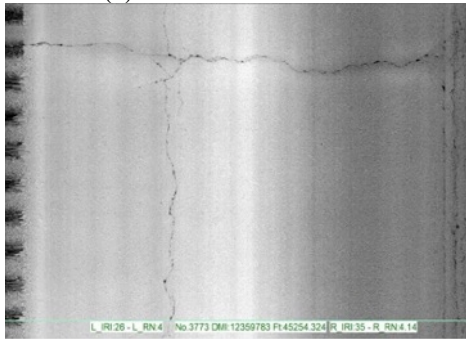
(1) Pavement location with no cracking or minor cracking has IRI less than 150 in/mi (Figure A.30); (2) Pavement location with small dip or medium distress has IRI between 150 in/mi and 300 in/mi (Figure A.31); (3) Pavement location with wide cracking, big dip, or other severe distress has IRI larger than 300 in/mi (Figure A.32).
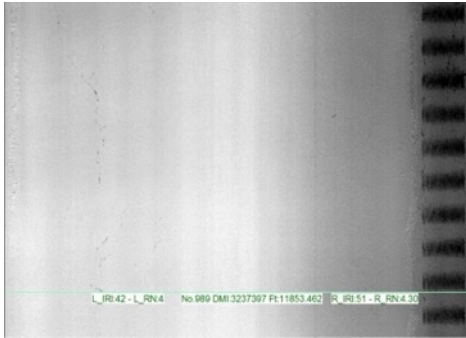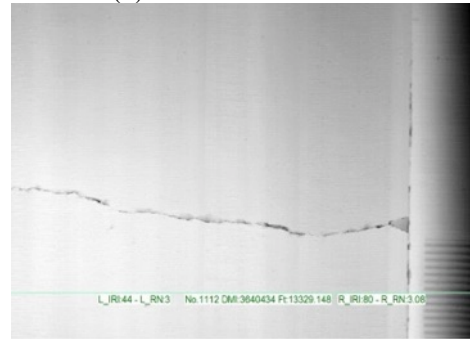
(a) AC with small cracks
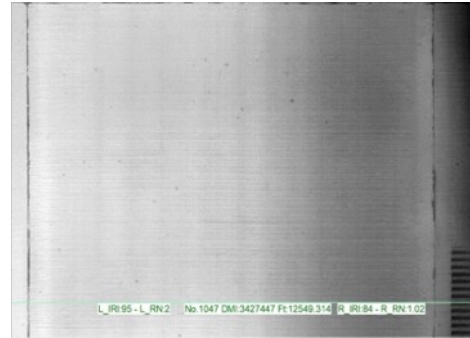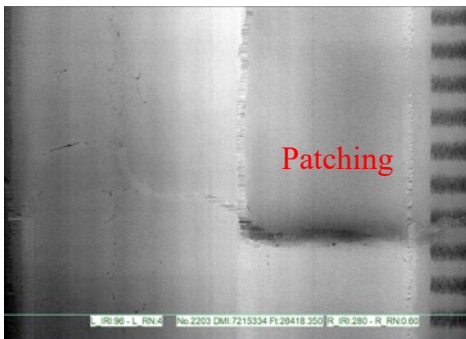

(b) PCC without distress
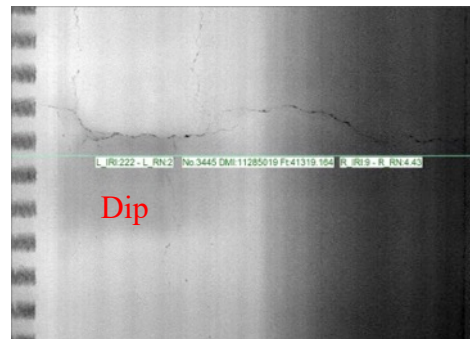

(c) AC with transverse crack but no dips

(d) PCC with transverse crack

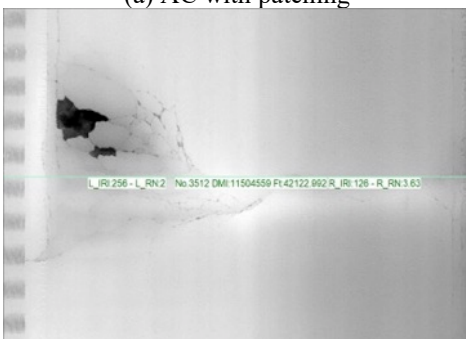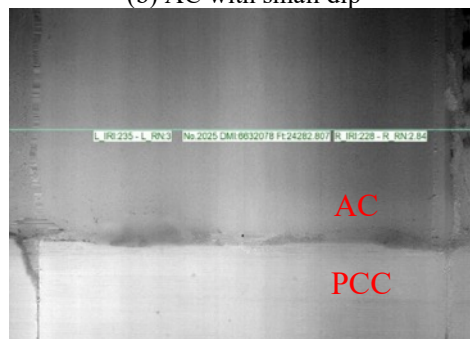*Figure A.30 Pavement condition and corresponding IRI (<150 in/mi).*

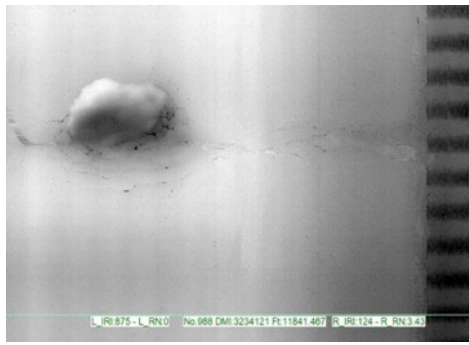
(a) AC with patching

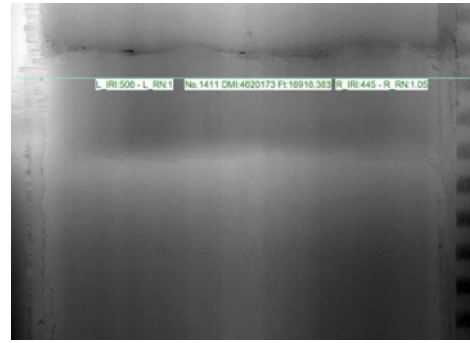(b) AC with small dip

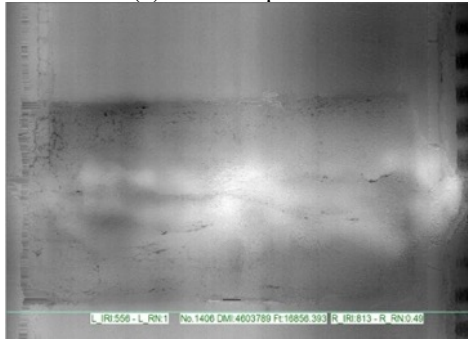(c) AC with alligator cracking

(d) Joint of AC and PCC

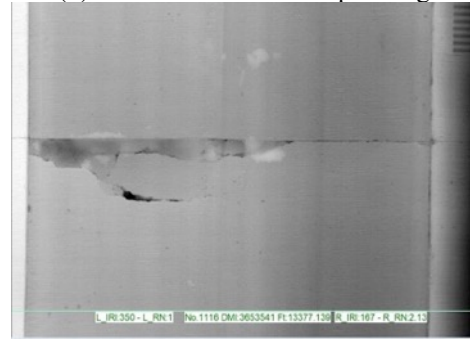*Figure A.31 Pavement condition and corresponding IRI (150–300 in/mi).*
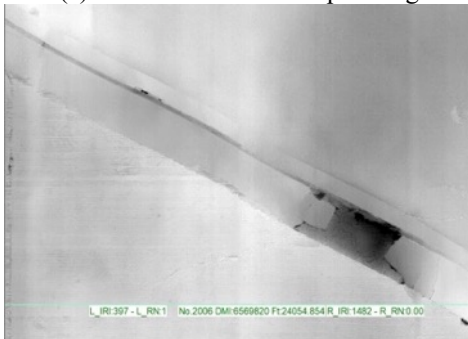
(a) AC with pothole

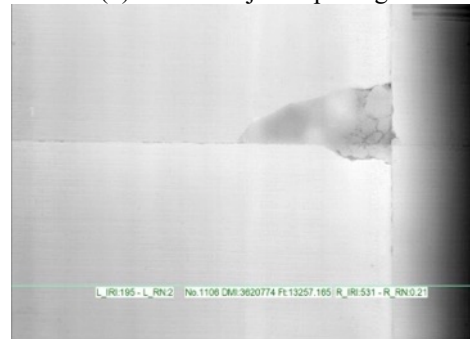(b) AC with "Inverted-T" patching

(c) AC with deteriorated patching

(d) PCC with joint spalling

(e) Bridge joint

(f) PCC with corner break

*Figure A.32 Pavement condition and corresponding IRI (>300 in/mi).*

Figure A.30, Figure A.31, and Figure A.32 list examples of pavement 3D images with different distresses and corresponding IRI results. The green numbers in each image list the left and right roughness indicators including IRI and roughness number (RN). For example, in "AC with transverse crack but no dips" in Figure A.30(c), the left IRI is 26 in/mi and the right IRI is 35 in/mi. It means pavement sections with some cracks, but no dips still have small IRI numbers less than 100 in/mi. For "AC with small dip" in Figure A.31(b), there are some cracks and a small dip on the left side for this location, therefore, the IRI is 222 in/mi for the left side whereas 9 in/mi for the right side. For "AC with pothole" in Figure A.32(a), there is a pothole on the left side of the 3D image, for that reason, the IRI is 875 in/mi for the left side and 124 in/mi for the right side. For "AC with "Inverted-T" patching" in Figure A.32(b), the cracks of this location are not big whereas the IRI is 506 in/mi for the left side and 445 in/mi for the right side due to the existence of dip on the "Inverted-T" patching. Therefore, the IRI results for the 12 feet pavement

section is highly related to localized pavement distress and can be used to identify pavement sections with localized distress, such as locations with "Inverted-T" patching that causes dip or reflective transverse cracks.
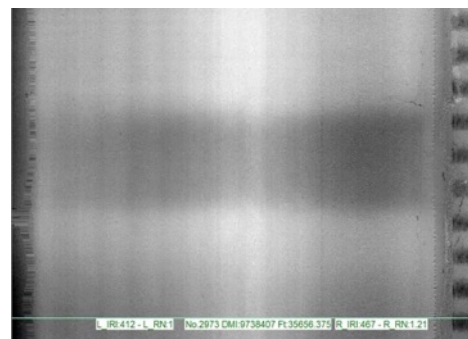
A.5.2 IRI and "Inverted-T" Patching

With the understanding that pavement IRI of 12 feet pavement section and localized distress are related to Inverse-T locations, the relationship between IRI and pavement sections with potential "Inverted-T" patches is carefully reviewed. Figure A.33 lists example 3D images and corresponding IRI results of locations with potential "Inverted-T" patching. The "Inverted-T" patches with two transverse cracks are obvious candidates for patch repair (Figure A.33(a)). However, there are potential locations with "Inverted-T" patches causing dip but no transverse cracks or only one transverse crack (Figure A.33(b) to (d)).

For example, Figure A.33(a) has two transverse cracks and the IRI around this location is 813 in/mi and 809 in/mi. In Figure A.33(b), it has no transverse cracks but a dip with almost 0.5 in. height difference, so the IRI around this location is 412 in/mi for the left and 467 in/mi for the right. If there is no dip around this place, the IRI number would be less than 100 in/mi. In Figure A.33(d), only one transverse crack is observed. Normally, the IRI should be less than 150 in/mi if there is no other distress on this location. However, there is a dip with more than 0.5-in. height difference which causes large IRI results (720 in/mi and 810 in/mi) for the left and right sides of this location. These examples indicate potential locations with "Inverted-T" patches may not always have two transverse cracks but always have a high IRI number.
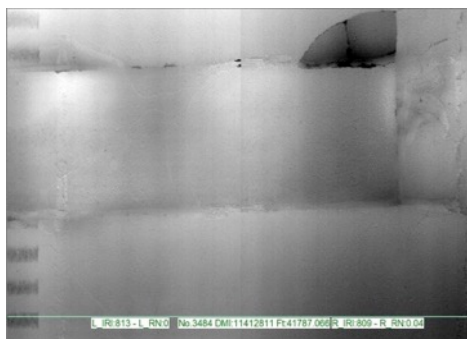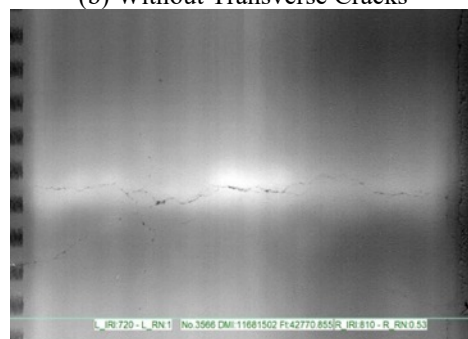

(a) With Two Transverse Cracks   (b) Without Transverse Cracks
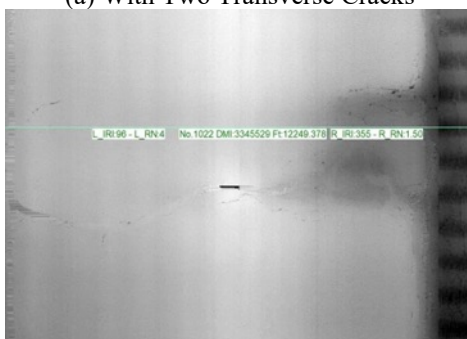
(c) With One Transverse Crack   (d) With One Transverse Crack

Figure A.33 Example of potential "Inverted-T" patching.

Therefore, for a pavement section, a large IRI number can be a better indicator for "Inverted-T" patching rather than determine if it has two transverse cracks. In other words, it is not accurate to determine the location of "Inverted-T" patching by just looking for locations with two transverse cracks. Sometimes, the "Inverted-T" patching may cause dip first with no transverse crack or just one transverse crack. For example, there were 30 images labeled as "Inverted-T" patching candidate from the 13th data collection "LL62 I-74 EBDL-20190531.111914" when judging if a prepared pavement 3D image has two transverse cracks. For the same data collection, 92 locations were labeled as "Inverted-T" patching candidate by checking if a location has large IRI number. Similarly, for the 14th data collection "LL62 I-74 WBDL 3-20190531.104216", there were only 4 candidates identified when judging if a location has two transverse cracks but 97 candidates by if a location has large IRI number.

Consequently, it is more reliable to determine the location of "Inverted-T" patching from IRI results. However, a large IRI number is not always caused by "Inverted-T" patching. As shown in Figure A.32, locations such as bridge joint (Figure A.32(e)), concrete sections with distress (Figure A.32(d) and (f)), or AC with potholes (Figure A.32(a)), patching (Figure A.32(c)), or other distresses also have IRI numbers larger than 300 in/mi. These locations should be removed from the final "Inverted-T" patching list. Therefore, IRI based "Inverted-T" patching detection is possible while it is desired to develop a tool to (1) list locations with IRI numbers larger than user defined threshold, and (2) remove locations with large IRI numbers due to other distresses.

A.5.3   IRI based "Inverted-T" Patching Detection in ADA

With this conclusion, the IRI based "Inverted-T" patching detection tool is developed in ADA software (Figure A.8). The ADA is able to perform automatic pavement cracking detection via DL based algorithm, IRI and rutting calculation, texture evaluation, and other pavement distress detection using data collected from the WayLink 3D laser imaging system. With this tool, the user can specify a threshold for IRI results to screen locations with IRI numbers: if "Scan" is initiated by the user, the ADA software will list locations with IRI results larger than the specified threshold. For example, the threshold of IRI is 120 in/mi in Figure A.34, and the three locations with IRI larger than 120 in/mi are listed as candidates for "Inverted-T" patching. The GPS coordinate, image ID, and distance for each candidate are also listed.
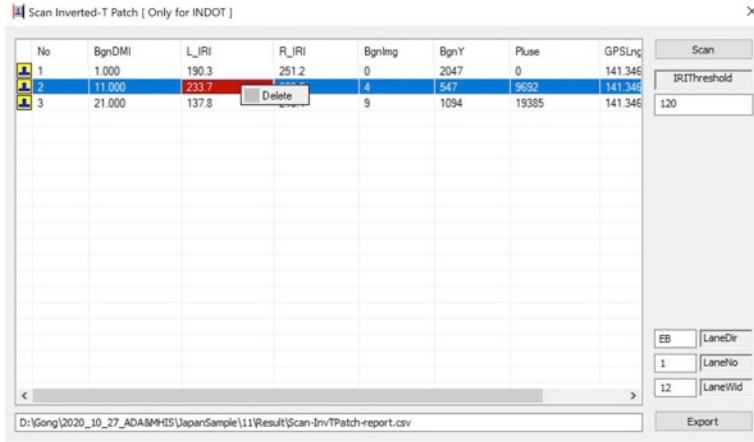
Figure A.34 IRI based "Inverted-T" patching detection.

If the user double-clicks any of the candidates, the ADA software will display the corresponding 2D/3D and ROW images for quality check. If the user found that large IRI is caused by bridge joint, concrete sections with distress, or asphalt sections with potholes, patching, or other distresses, the user can delete that candidate by right clicking the mouse and selecting "Delete" (Figure A.34). After finishing quality check for all the candidates, the final list of "Inverted-T" patching can be exported to a .csv file to create a patching table database for INDOT engineers to perform evaluation for eventual patch repairs. Furthermore, the speed of IRI based "Inverted-T" patching detection is good: with this newly developed tool in ADA, engineers should have a patch repair table populated in less than 2 hours for a data collection around 10 miles long.

A.5.3   IRI Threshold Value

Different conditions of "Inverted-T" patching correspond to different levels of IRI numbers. Figure A.35 shows four different locations from data collection "LL62 I-74 EBDL-20190531.111914" and the corresponding IRI numbers. For Figure A.35(a), the "Inverted-T" patching has minor cracks and small settlement difference as surrounding pavement, the IRI is 127 in/mi for the left side and 113 in/mi for the right side. For the locations in Figure A.35(c) and (d), the cracking and settlement difference are worse than the location in Figure A.35(a), therefore, a higher IRI number is observed for these two locations. In Figure A.35(d), the "Inverted-T" patching has wider cracks and larger settlement difference as surrounding pavement. So, the IRI is 437 in/mi for the left side and 353 in/mi for the right side.

As a result, a reasonable threshold value of IRI should be determined for the "Inverted-T" patching detection tool in Figure A.34. If a small IRI threshold value is specified in the tool, it will list many candidates that may include all the potential locations of "Inverted-T" patching but also require longer time to complete quality check. On the other side, if a large IRI threshold value is specified in the tool, it lists less candidates that requires less time to complete quality check but may miss some "Inverted-T" patching locations with small dip or less IRI values. A reasonable threshold value of IRI should capture most of the potential "Inverted-T" patching locations while requiring reasonable time for quality check.

At this point, the IRI numbers of potential "Inverted-T" patching in four data collections have been summarized to determine the desired threshold of IRI for the "Inverted-T" patching detection tool in Figure A.34. Each candidate with IRI larger than 100 in/mi is carefully reviewed by the research team to determine if it is "Inverted-T" patching. The IRI distribution of the final "Inverted-T" patching candidates for each data collection is listed in Table A.6. For example, for data collection "LL62 I-74 EBDL-20190531.111914", there are 82.61%, 60.87%, 48.91%, and 41.30% of potential "Inverted-T" patching locations when using 150 in/mi, 200 in/mi, 250 in/mi, and 300 in/mi as IRI thresholds.

*Table A.1 IRI Distribution of Potential "Inverted-T" Patching*

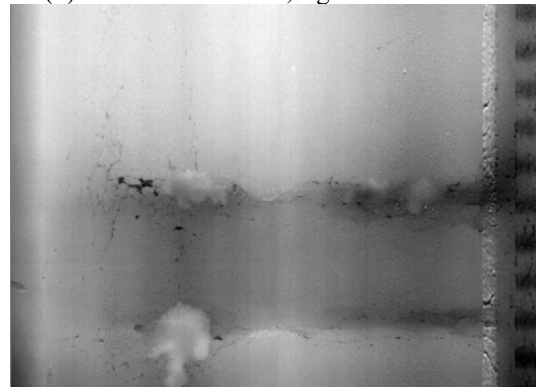| Data Collections	IRI Threshold (in/mi)			
	150	200	250	300
LL62 I-74 EBDL-20190531.111914	82.61	61.96	50.00	42.39
LL62 I-74 WBDL 3-20190531.104216	86.60	76.29	60.82	47.42
LL 62 I-74 WBPL-20190531.123431	83.33	78.33	56.67	36.67
LL 62 I-74 EBPL-20190531.131121	85.11	74.47	65.96	53.19
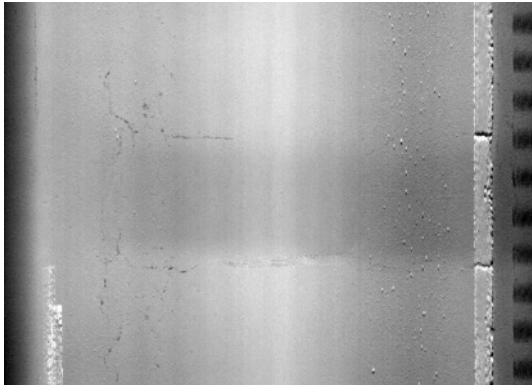
(a) Left IRI: 127 in/mi; right IRI: 113 in/mi
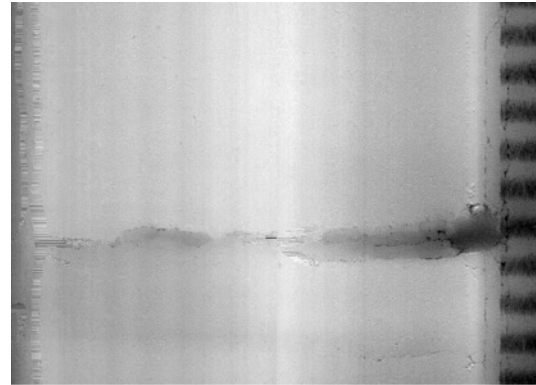
(b) Left IRI: 173 in/mi; right IRI: 162 in/mi
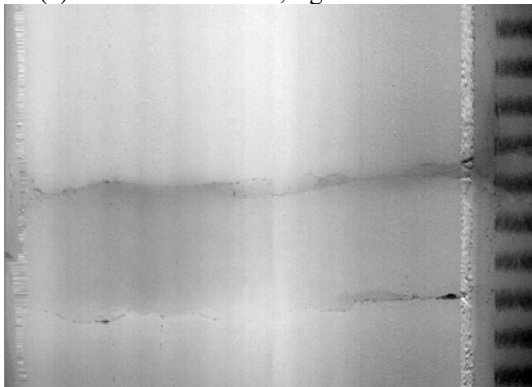
(c) Left IRI: 237 in/mi; right IRI: 151 in/mi

(d) Left IRI: 437 in/mi; right IRI: 353 in/mi

Figure A.35 IRI of different "Inverted-T" patching.

Nevertheless, potential "Inverted-T" patching locations with IRI less than 150 in/mi are not easy to distinguish in 3D images, as shown in Figure A.35(a), this potential "Inverted-T" patching has IRI 127 in/mi on the left and 113 in/mi on the right. Therefore, 150 in/mi is

recommended as the starting point of IRI threshold for screening "Inverted-T" patching. This might be conservative and will take longer time to check all the possible candidates for quality check.

As listed in Table A.6, 61.96%, 76.29%, 78.33%, and 74.47% of potential "Inverted-T" patching locations in the four data collections have IRI larger than 200 in/mi, while 42.39%, 47.42%, 36.67%, and 53.19% of potential "Inverted-T" patching locations in the four data collections have IRI larger than 300 in/mi. It indicates many potential "Inverted-T" patching locations with IRI less than 300 in/mi (Figure A.35(b) and (c)) will be missed, if 300 in/mi is used as the threshold value. Consequently, 200 in/mi is recommended as IRI threshold for routine screening of "Inverted-T" patching. In this case, the user can detect more than 60% of the locations with potential "Inverted-T" patching and IRI larger than 200 in/mi.

Lastly, it is worth mentioning that the IRI based "Inverted-T" patching detection method is more practical and useful than the DL method in the following aspects:

(1) Unlike DL based "Inverted-T" patching detection method that only identifying locations with two transverse cracks, the IRI based method will identify potential "Inverted-T" patching locations having large IRI numbers with two, one, or no transverse cracks. So, the IRI based "Inverted-T" patching detection tool will result in more complete results.

(2) The results from IRI based method is more accurate than DL based method that only works well on the prepared training dataset but has many false predictions on images from a normal data collection.

(3) The speed of IRI based method is acceptable to narrow down the patch search area for INDOT. Depending on the number of the potential "Inverted-T" patching in a data collection, the data processing speed of IRI based "Inverted-T" patching detection should be more than 5 mph to generate a final "Inverted-T" patching table.

A.6   Conclusions

In this study, detection of "Inverted-T" patching using images and roughness data from the WayLink 3D laser imaging system was performed to narrow down the patch search area and create a patching table database for INDOT. From 2019 and 2020, a total length of 447 miles of pavement was scanned with the 4K and 8K laser imaging system. The 3D images with potential "Inverted-T" patching was manually identified and labeled to prepare the training data for different DL models.

Three popular and advanced DL models were explored to automatically detect "Inverted-T" patching using pavement 3D images: two object detection models (SSD300 and Mask R-CNN) and one image segmentation model (U-Net). The DL based methods show good performance on the prepared dataset but have many false predictions on images from a normal data collection. There are two major challenges to improve the performance of these DL models for automatic "Inverted-T" patching detection: (1) The number of training images are limited in this study; and (2) the "Inverted-T" patching is so similar to the background that the DL model may not be able distinguish them through the networks' cognition capabilities.

Subsequently, the IRI based "Inverted-T" patching detection was explored because the weak connection between "Inverted-T" patching and existing pavement can cause dips or transverse cracks that introduce abnormal pavement roughness condition and ride quality. It is demonstrated that the IRI results for 12 feet pavement section is related to localized pavement

distress, such as "Inverted-T" patching. A software tool is developed in the ADA software to display locations with IRI numbers larger than the threshold and generate final patching table for INDOT. Also, 150 in/mi is recommended as the IRI threshold in a conservative manner, while 200 in/mi is recommended as the IRI threshold for routine screening of "Inverted-T" patching.

A data fusion work will be conducted as part of the project to match the patching table from IRI based "Inverted-T" patching detection tool to the patching table from the Purdue team that is generated from the GPR data. It is the anticipation that the two patch tables and methods would be integrated to further improve the detection accuracy of Inverse-T patches in the INDOT pavement network. For future work consideration, DL based methods remain good candidates to detect patch locations on pavement surface as long as adequate training samples can be obtained and labeled.

APPENDIX B. METAL PLATE EXPERIMENT AT RESEARCH DIVISION

B.1 Introduction

An experiment was recently run at the INDOT Research Division in West Lafayette involving a ground penetrating radar (GPR) made by Geophysical Survey Systems, Inc. The experimental apparatus includes the Model 3101A and 3101D Tx/Rx antenna packages including digital-to-analog conversion, transmit amplifier, bowtie transmit antenna, bowtie receive antenna, receiver filters and amplifiers, and analog-to-digital conversion. The radar is controlled by a Model SIR 30 radar controller.

The system is setup to run at 900 MHz center frequency and is an ultra-wideband pulse radar with pulse width of approximately 1.1 nsec. Nominally, the pulse is supposed to be a Ricker wavelet (Daniels, 2004). See Figure B.1 where the controller is on the hand cart and the antenna package is positioned over a metal plate lying on the shop floor. The purpose of the experiment was to gather data to estimate the shape and duration of the radar pulse in a relatively simple situation. In actual use the returned radar signal is a complicated superposition of many reflected radar returns—the experimental situation explored here should only involve one strong reflection.
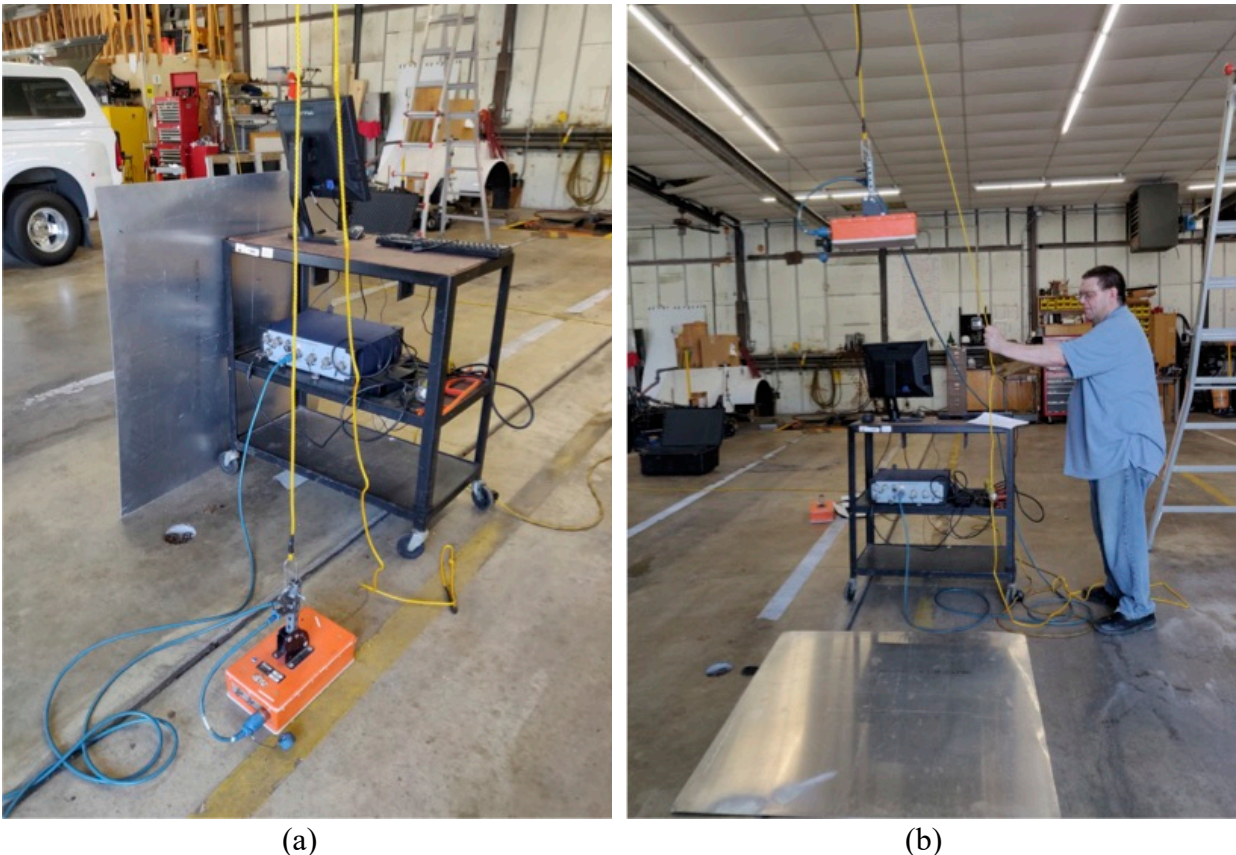
(a)   (b)

Figure B.1 Single pulse experiment in the INDOT research division shop: (a) Test equipment. (b) Test data collection.

The experiment was run by holding the antenna package over the metal plate at a particular height and collecting a large number of returns, which would nominally be identical. Then the height was changed and the experiment was repeated. Matlab .mat files were saved containing the raw data captured from the two antenna packages at different heights. When one of these files is loaded into Matlab a matrix variable is created of size $M \times N$. The row index corresponds to the time samples of the received radar return in response to the transmission of a single pulse. The column index corresponds to replications of the basic transmit pulse and receive radar return scenario. All of the files have $M = 508$ time samples in each return. The number N changes from .mat-file to .mat-file because the duration of each experimental run varies.

B.2   Preliminary Look at the Data

An image was created for the returns recorded with the radar antenna positioned about 6 feet above the metal plate in the INDOT shop. The result is shown in Figure B.2. The image shows a white band starting about 3.3 nsec followed immediately by a dark band. Further down in the image one sees a disturbance around 16 nsec. As it turns out the first band has nothing to do with the plate. It is a so-called direct wave traveling from transmit to receive antenna with no apparent reflection. Assuming that the time required for the radar wave to travel directly from transmit antenna to receive antenna is negligible, we can set 3.3 nsec as the starting time of the pulse. Given this, the round trip time to the metal plate on the shop floor should be about 16 - 3.3 = 12.7 nsec, a reasonable number if the spacing between radar antennas and metal plate is about 6 feet.

Figure B.3 shows an individual radar return taken at each spacing. This clearly indicates how the first major wave is independent of spacing and how the second wave is the pulse returning to the radar after reflection on the metal plate. At spacings of 2 feet and larger there is little interaction between direct wave and the reflected pulse while at 1 foot spacing interference is starting. Based on this observation it is reasonable to estimate the basic radar pulse width at 2 nsec. Note that the radar antenna manual claims a 1.1 nsec pulse width.

Note that the reflected pulse in the 2 foot trace of Figure B.3 shows the classical Ricker wavelet shape. However, there are two questions that come up when comparing the reflected pulse to the direct wave pulse. First, the direct wave appears to be distorted and does not have the expected Ricker shape. Second, it is not clear that there is a negative inversion between the direct wave pulse and the reflection, which is expected from the physics. We will return to this question later.
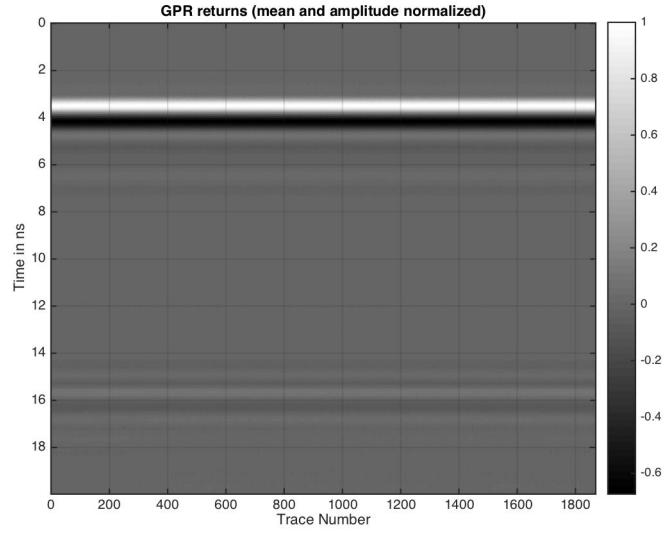
Figure B.2 Grey scale image created from about 1,870 individual traces captured from the GSSI 3101A while it was positioned about 6 feet above the metal plate.
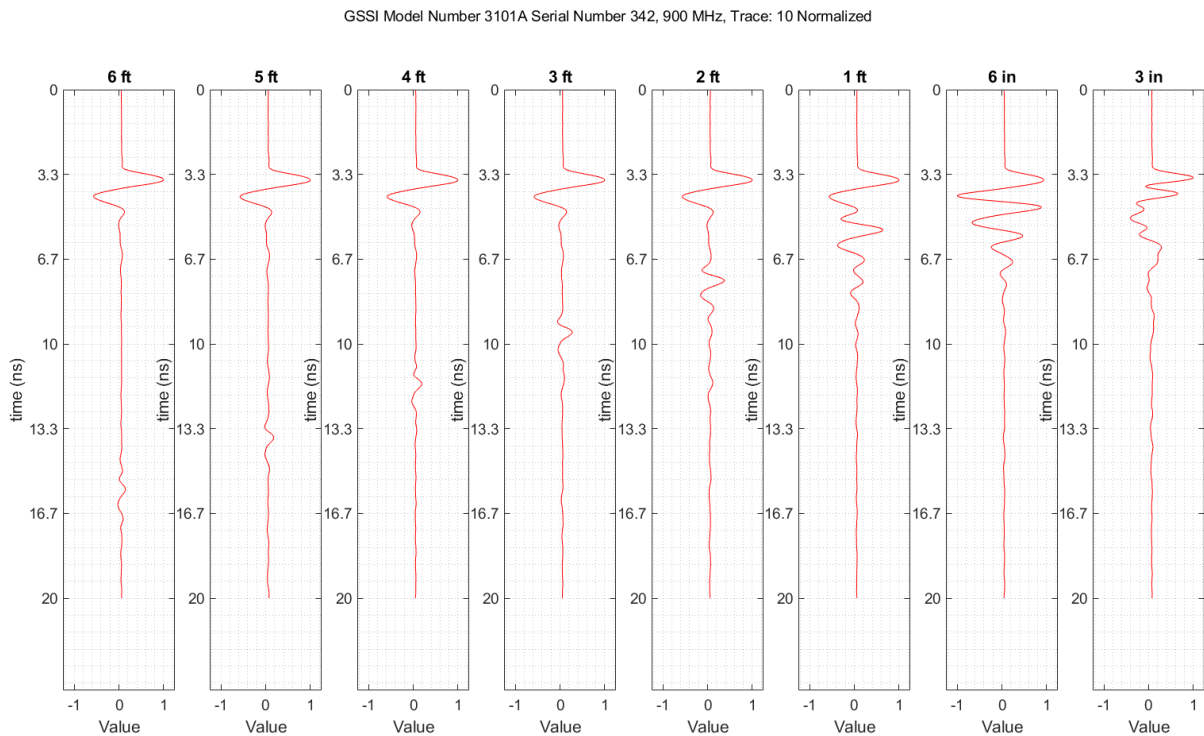

Figure B.3 Representative traces of the GSSI 3101A return captured at differing heights above the metal plate.

B.3   The Ricker Wavelet

A Ricker Wavelet is the second derivative of a Gaussian pulse. For a generic Gaussian pulse with "mean" zero and "variance" τ^2 the Ricker pulse $r(t)$ and its corresponding Fourier transform $R(f)$ are

$$r(t) = \left(\frac{-1}{\sqrt{2\pi\tau^3}}\right)\left[1 - \frac{t^2}{\tau^2}\right]e^{-t^2/2\tau^2}$$

$$R(f) = (j2\pi f)^2 e^{-2\pi^2\tau^2 f^2}$$

In the frequency domain the Ricker Pulse will have a zero at $f = 0$ and a peak at some center frequency, which we can find by taking the derivative of $R(f)$ and setting that equal to zero. Doing so we find solutions $f = 0$ and $f = \pm 1/\sqrt{2}\pi\tau$. To set the center frequency at 900 MHz as is apparently the case in GSSI Model 3101A we would find

$$\tau = \frac{1}{\sqrt{2}\pi(900\ MHz)} \approx 0.25\ nsec.$$

These pulses and their Fourier transforms are shown in Figure B.4(a) and (b).

(a)   (b)
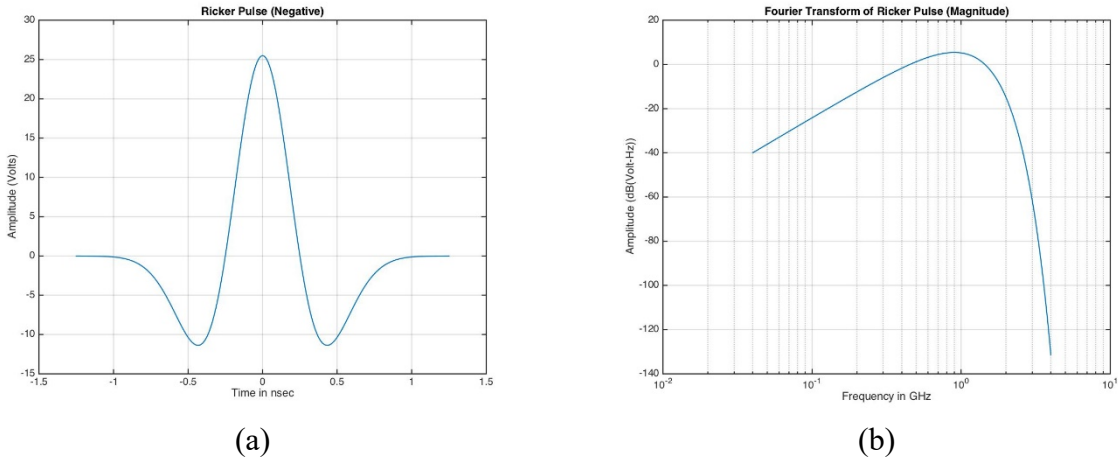
Figure B.4 Ricker pulse (a) and its Fourier transform (b) for pulse width parameter $\tau = 0.25\ nsec$.

B.4   Model for the Data

A mathematical model for a single return is of the form: $y(t) = p(t) + cp(t - T) + n(t)$. Here $p(t)$ is the transmitted pulse, T is the roundtrip delay time for the pulse to travel from the radar transmit antenna to the metal plate and back to the radar receive antenna, and c is an attenuation factor. Each return contained in a data matrix can be considered to be an independent observation following the basic model above. Let Y be one of the $M \times N$ data matrices and let y_k

denote its columns. The unknowns in this problem are real numbers T, c and the transmitted pulse p considered as a $K \times 1$ vector (note $K < M$). Then a model for the repeated observations is

$$y_k = H(c, T)p + n_k$$

for $k = 1, 2, \ldots, N$. Here the $\{n_k\}$ are unobserved noise vectors and H is an $M \times K$ matrix which is a function of c and T. The minimization problem is then:

$$\min_{c,T,p} \sum_{k=1}^{N} \|y_k - H(c, T)p\|^2.$$

In the collected data sets time has already been sampled and so we may as well assume that the delay variable T is an integer number of samples.

Let's assume the sampling interval for radar returns is T_s. For the data taken here the value is approximately $T_s = 0.04 \, nsec$. The pulse p is $K \times 1$ and considerably shorter than the observation window M where we are expressing time in terms of integer numbers of samples. In the collected data $M = 508$ corresponding to a total roundtrip delay time of 20 nsec. If the transmitted Ricker pulse were of duration equal to 1.1 nsec as suggested by the GSSI manual, then the pulse width in samples should be $K = 28$. If instead we use our observation that the pulse width is about 2 nsec, then $K = 50$.

The $M \times M$ *delay-by-one-sample* matrix Z_1 has ones on the diagonal just below the main diagonal and zeros elsewhere. We can create the delay-by-Δ-samples matrix as a power of Z_1:

$$Z_\Delta = Z_1^\Delta = \begin{bmatrix} 0 & 0 & 0 & & 0 & 0 \\ 1 & 0 & 0 & \cdots & 0 & 0 \\ 0 & 1 & 0 & & 0 \vdots & 0 \\ & \vdots & & \ddots & 0 & \vdots \\ 0 & 0 & 0 & \cdots & 1 & 0 \end{bmatrix}^\Delta$$

Equivalently, we may also define Z_Δ as the matrix with ones on its Δ-th diagonal below the main diagonal and zeros elsewhere. Also, note that Z_1^T is the $M \times M$ *advance-by-one-sample* matrix.

If the pulse support p were assumed to be the same length as the radar return, then the model matrix $H(c, \Delta)$ would be simply $I + cZ_\Delta$. Let $\tilde{I}$ denote the $M \times K$ matrix formed by deleting the the last $M - K$ columns of the $M \times M$ identity matrix. Note that the product of multiplying an $M \times M$ matrix A on the right by $\tilde{I}$ is itself the $M \times K$ matrix $\tilde{A} = A\tilde{I}$ obtained from $\tilde{A}$ by deleting the last $M - K$ columns.

Therefore, with a pulse p constrained to be $< K$ samples long the model matrix becomes

$$\tilde{H}(c, \Delta) = (I + cZ_\Delta)\tilde{I} = \tilde{I} + c\tilde{Z}_\Delta.$$

To shorten the notation, we will drop the explicit reference to c and Δ and write $\tilde{H} = \tilde{I} + c\tilde{Z}$.

The objective function is $OF(c, \Delta, p) = \sum_{k=1}^{N} \|y_k - \tilde{H}p\|^2$ which is easily simplified to

$$\widetilde{OF}(c, \Delta, p) \quad = \quad -2\left(\frac{1}{N}\sum_{k=1}^{N} y_k^T\right)\tilde{H}p + p^T\tilde{H}^T\tilde{H}p \quad = \quad -2\bar{y}^T\tilde{H}p + p^T\tilde{H}^T\tilde{H}$$

For a fixed value of the delay parameter Δ the first order partial derivatives of the objective function with respect to c and the components of the vector p exist and are easily seen to be given by

$$\nabla_p \widetilde{OF}(c, \Delta, p) \quad = \quad -2\tilde{H}^T\bar{y} + 2\tilde{H}^T\tilde{H}p$$

$$\frac{\partial}{\partial c}\widetilde{OF}(c, \Delta, p) \quad = \quad -2\bar{y}^T\frac{\partial \tilde{H}}{\partial c}p + p^T\frac{\partial\{\tilde{H}^T\tilde{H}\}}{\partial c}p$$

Ideally, we would set these equal to zero and solve for p, c, which would represent a stationary point and hopefully, a minimum. We would use

$$\frac{\partial \tilde{H}}{\partial c} = \tilde{Z}$$

and

$$\frac{\partial \{\tilde{H}^T \tilde{H}\}}{\partial c} = \tilde{I}^T \tilde{Z} + \tilde{Z}^T \tilde{I} + 2c\tilde{Z}^T \tilde{Z}.$$

Note that $\tilde{I}^T A$ deletes the last $M - K\$$ rows of the matrix A. Therefore, $\tilde{I}^T \tilde{Z} = \tilde{I}^T Z \tilde{I}$ is actually, the $K \times K$ *delay-by*-Δ matrix. If we make the substitutions into the previous equations and set them equal to zero then we have an expression for the set of simultaneous equations that should be solved for values c and p that give a stationary point of the objective function. These are for a fixed hypothetical delay Δ, whose notation has been suppressed

$$-2(\tilde{I}^T + c\tilde{Z}^T)\bar{y} + 2(\tilde{I}^T \tilde{I} + c\tilde{I}^T \tilde{Z} + c\tilde{Z}^T I + c^2 \tilde{Z}^T \tilde{Z})p \quad = \quad 0$$

$$-2\bar{y}^T \tilde{Z}p + p^T(\tilde{I}^T \tilde{Z} + \tilde{Z}^T \tilde{I} + 2c\tilde{Z}^T \tilde{Z})p \quad = \quad 0$$

The above are coupled quadratic equations in the $K + 1$ variables c and p and it is not easy to see a closed form solution.

An expedient approach to solving is to iterate between solutions of the two parts. That is, assume a value for c and use the top equation to solve for p. Then substitute that value into the bottom equation to solve for c. Iterate for a few steps to see what happens. The resulting algorithm is summarized in the table below.

Algorithm 1: Method for solution of the minimization of problem.

Result: Compute p_{best}, c_{best}, Δ_{best}:

$\bar{y} = \frac{1}{N} \sum_{k=1}^{N} y_k$;

initialize $-$;

$r_{best} = 100$;

$p_{best} = [1, 1, \ldots, 1]^T$;

$c_{best} = 0$;

$\Delta_{best} = 1$;

for $\Delta = 1$ *to* N **do**

    initialize $-$;

    $c = 0.9$;

    $p = [1, 1, \ldots, 1]^T$;

    $\epsilon = 1$;

    while $\epsilon > 0.01$ **do**

        compute $\tilde{H}$ from Δ and c;

        solve $\tilde{H}^T \tilde{H} p_{new} = \tilde{H}^T \bar{y}$ for p_{new};

        solve $-2\bar{y}^T \tilde{Z} p_{new} + p_{new}^T (\tilde{I}^T \tilde{Z} + \tilde{Z}^T \tilde{I} + 2c_{new}\tilde{Z}^T \tilde{Z}) p_{new} = 0$ for c_{new};

        $q = [c, p^T]^T$;

        $q_{new} = [c_{new}, p_{new}^T]^T$;

        $\epsilon = \|q_{new} - q\| / \|q_{new}\|$;

        set $c = c_{new}$ and $p = p_{new}$;

    end

    $\hat{\bar{y}} = \tilde{H}p$;

    $r = \|\bar{y} - \hat{\bar{y}}\|$;

    if $r < r_{best}$ **then**

        $r_{best} = r$;

        $p_{best} = p$;

        $c_{best} = c$;

        $\Delta_{best} = \Delta$;

    end

end

B.5   Experimental Results

We have data sets from two nominally identical 900 MHz antennas, which makes sense to compare. Looking at the traces we see that there is an interval of dead time before the direct wave arrives. The algorithm developed estimates the beginning of the direct wave pulse and removes the "zero" signal at the beginning. The algorithm finds the least-squares estimate of the delay Δ, the pulse p, and the reflected pulse amplitude c. The table below shows the parameter values where the minimum was found. The least-squares residual is r.

Table B.1 Summary of Parameter Estimates

Distance	Model 3101A			Model 3101D		
	Δ_{best}	r_{best}	c_{best}	Δ_{best}	r_{best}	c_{best}
1 foot	33	0.80	-0.78	51	1.14	0.70
2 feet	100	0.82	0.26	102	0.83	0.34
3 feet	153	0.51	0.17	155	0.62	0.24
4 feet	204	0.36	0.11	205	0.53	0.17
5 feet	258	0.43	0.11	258	0.55	0.17
6 feet	309	0.35	0.09	311	0.57	0.12

Plots are included showing the return traces as an image and as a collection of overlaid wiggles in Figure B.5 for both 900 MHz antennas and for heights of 1, 3, and 5 feet. Figure B.6 compares the average trace with its least-squares estimate as reconstructed from the estimated model parameters. Finally, Figure B.7 compares the estimated pulses.

B.6   Conclusions

1. Looking at in Figure B.5 we see that interference between the direct and reflected waves is apparent at the 1 foot spacing. It is also evident at smaller spacings as well. We also start to see negative values for c_{best} and some irregularity in the value for best delay variable, i.e., Δ_{best} does not scale proportionally with height for heights less than 1 foot.
2. Running the code at 2 feet, 3 feet, 4 feet with either antenna shows the characteristic Ricker shape in the reflected waves even though it is not evident in the direct wave, nor is the expected negative reflection found in the value found for c_{best}. Note, however, that the values for Δ_{best} scale proportionally with height.
3. We had to pick the expected pulse length in samples larger than would correspond to either the 1.1 nsec or 2 nsec lengths in order to get a nice result.
4. The estimated pulses are clearly dominated by the very strong direct path signal and do not really show the Ricker shape even though it is present in the reflected wave. The direct wave likely has some non-linear distortion. See Figure B.8 which shows a hypothesized distortion of the recorded direct wave which might explain both the non-Ricker shape and the inversion the physics requires on the reflected wave.
5. Could rewrite the problem to enforce the Ricker pulse shape. Could also consider weighting the least squares error to de-emphasize the errors in the direct wave.
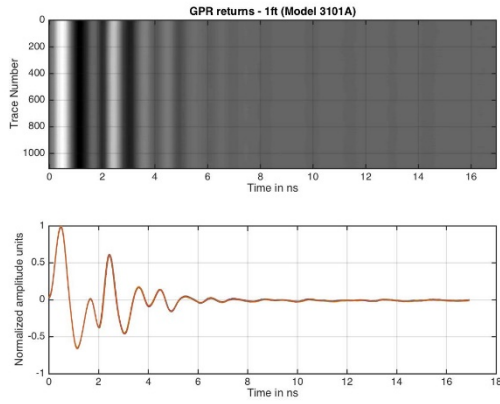
(a) Model 3101A - 1 foot   (b) Model 3101D - 1 foot
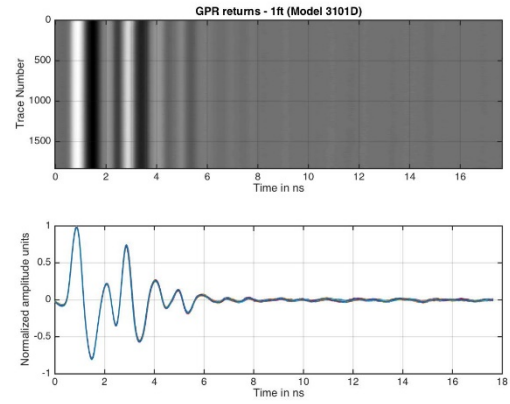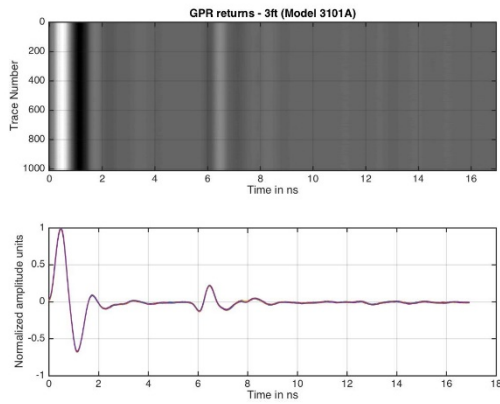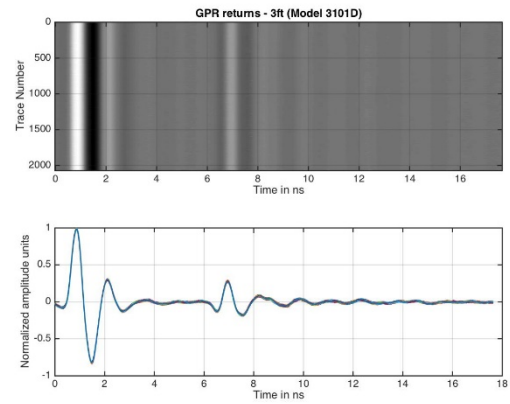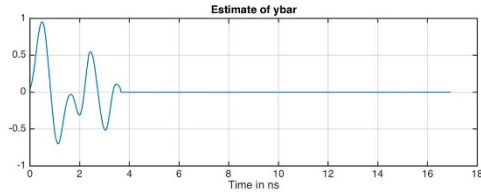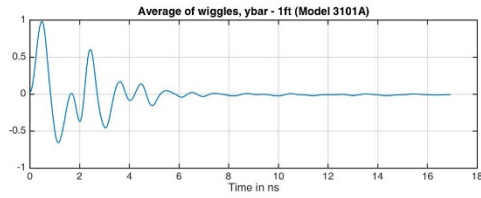
(c) Model 3101A - 3 feet   (d) Model 3101D - 3 feet
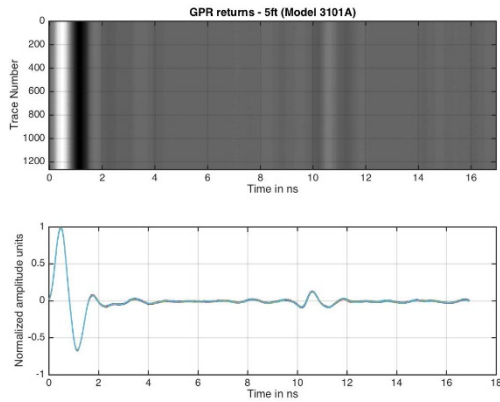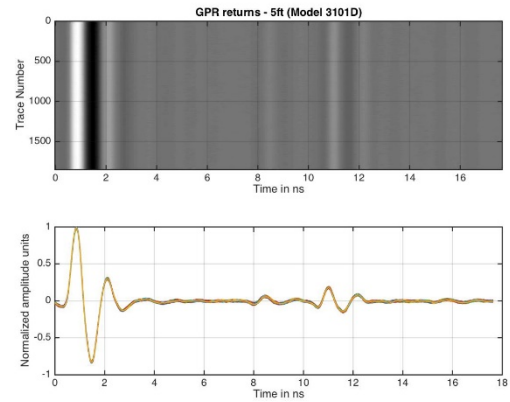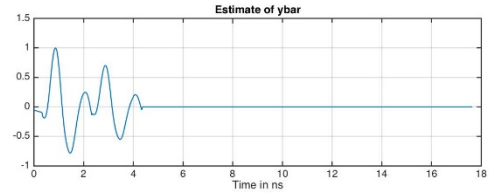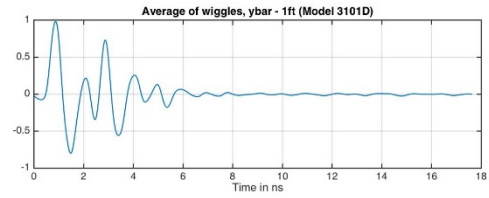
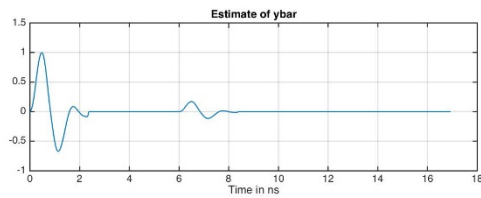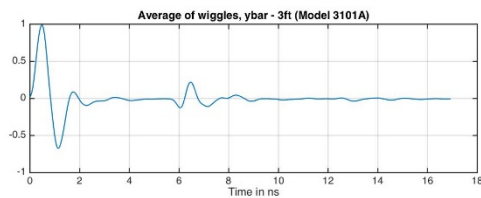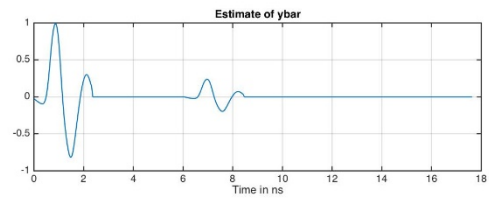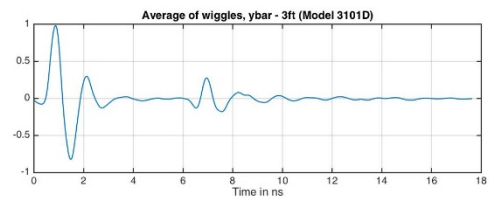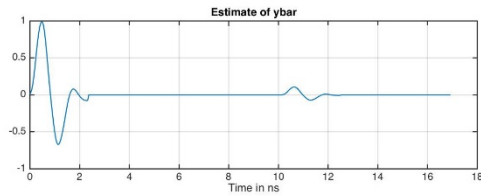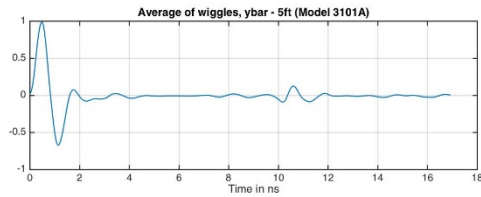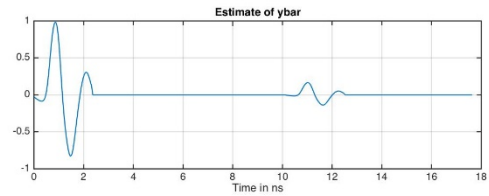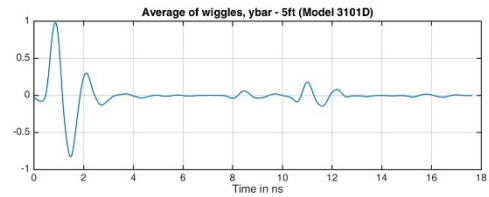(e) Model 3101A - 5 feet   (f) Model 3101D - 5 feet

Figure B.5 Return traces as image and overlaid wiggles.

(a) Model 3101A - 1 foot

(b) Model 3101D - 1 foot
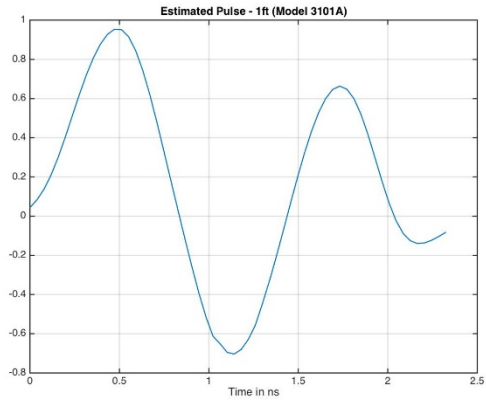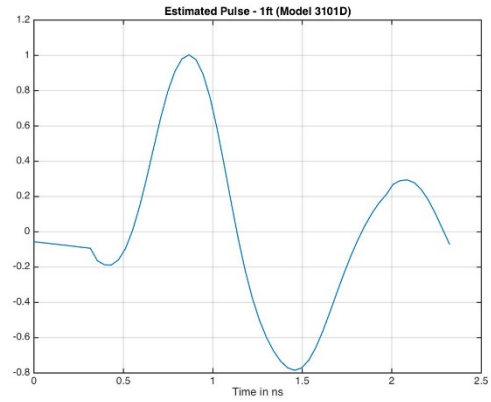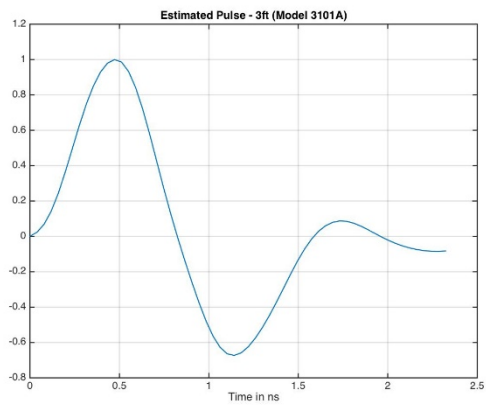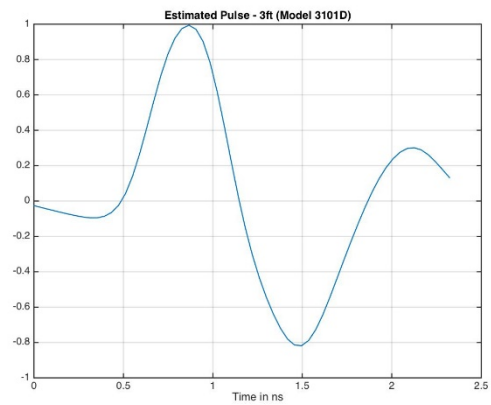
(c) Model 3101A - 3 feet

(d) Model 3101D - 3 feet

(e) Model 3101A - 5 feet

(f) Model 3101D - 5 feet

Figure B.6 Average traces compared with estimated trace in various scenarios.
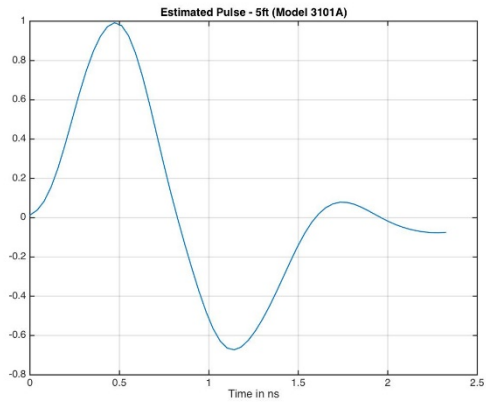
(a) Model 3101A - 1 foot
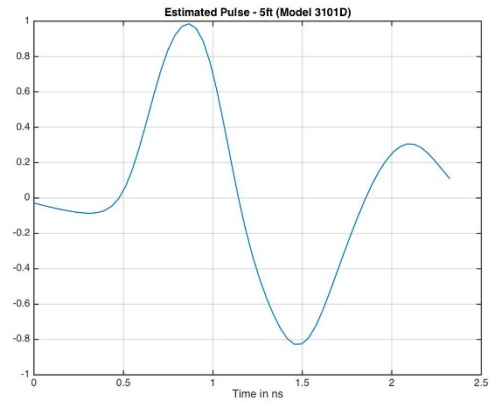
(b) Model 3101D - 1 foot

(c) Model 3101A - 3 feet

(d) Model 3101D - 3 feet

(e) Model 3101A - 5 feet

(f) Model 3101D - 5 feet
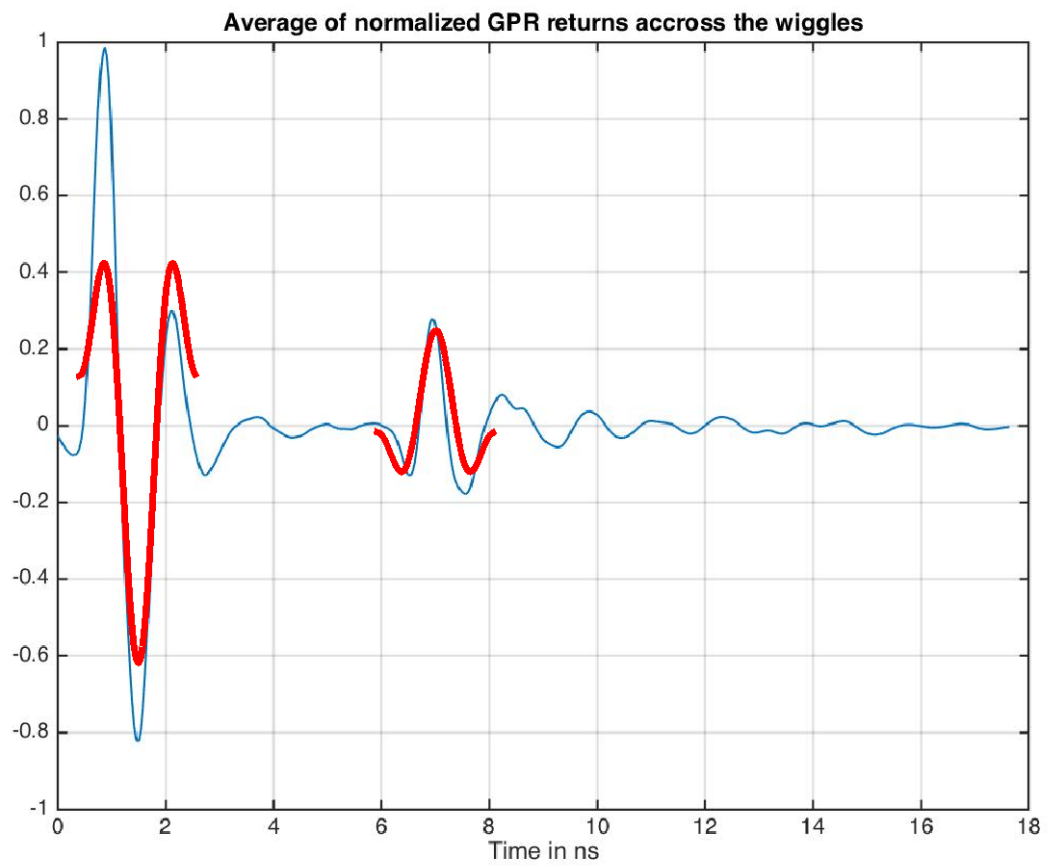
Figure B.7 Estimated pulse for various scenarios.

Figure B.8 Possible ricker distortion.

About the Joint Transportation Research Program (JTRP)

On March 11, 1937, the Indiana Legislature passed an act which authorized the Indiana State Highway Commission to cooperate with and assist Purdue University in developing the best methods of improving and maintaining the highways of the state and the respective counties thereof. That collaborative effort was called the Joint Highway Research Project (JHRP). In 1997 the collaborative venture was renamed as the Joint Transportation Research Program (JTRP) to reflect the state and national efforts to integrate the management and operation of various transportation modes.

The first studies of JHRP were concerned with Test Road No. 1—evaluation of the weathering characteristics of stabilized materials. After World War II, the JHRP program grew substantially and was regularly producing technical reports. Over 1,600 technical reports are now available, published as part of the JHRP and subsequently JTRP collaborative venture between Purdue University and what is now the Indiana Department of Transportation.

Free online access to all reports is provided through a unique collaboration between JTRP and Purdue Libraries. These are available at http://docs.lib.purdue.edu/jtrp.

Further information about JTRP and its current research program is available at http://www.purdue.edu/jtrp.

About This Report

An open access version of this publication is available online. See the URL in the citation below.

Cheng, P., Krogmeier, J. V., Bell, M. R., Wang, K., Li, J., & Yang, G. (2021). *Detection and classification of concrete patches by integrating GPR and surface imaging* (Joint Transportation Research Program Publication No. FHWA/IN/JTRP-2021/18). West Lafayette, IN: Purdue University. https://doi.org/10.5703/1288284317320